

NUMERICAL INVESTIGATION OF CIRCULATING FLUIDIZED BED RISER
HYDRODYNAMICS FOR CONCENTRATING SOLAR THERMAL RECEIVER
APPLICATIONS

A THESIS SUBMITTED TO
THE GRADUATE SCHOOL OF NATURAL AND APPLIED SCIENCES
OF
MIDDLE EAST TECHNICAL UNIVERSITY

BY

SERHAT BİLYAZ

IN PARTIAL FULFILLMENT OF THE REQUIREMENTS
FOR
THE DEGREE OF MASTER OF SCIENCE
IN
MECHANICAL ENGINEERING

SEPTEMBER 2015

Approval of the thesis:

**NUMERICAL INVESTIGATION OF CIRCULATING FLUIDIZED BED
RISER HYDRODYNAMICS FOR CONCENTRATING SOLAR THERMAL
RECEIVER APPLICATIONS**

submitted by **SERHAT BİLYAZ** in partial fulfillment of the requirements for the degree of **Master of Science in Mechanical Engineering Department, Middle East Technical University** by,

Prof. Dr. Gülbin Dural Ünver

Dean, Graduate School of **Natural and Applied Sciences**

Prof. Dr. Tuna Balkan

Head of Department, **Mechanical Engineering**

Assoc. Prof. Dr. İlker Tari

Supervisor, **Mechanical Engineering Dept., METU**

Examining Committee Members:

Assoc. Prof. Dr. Almıla Güvenç Yazıcıoğlu

Mechanical Engineering Dept., METU

Assoc. Prof. Dr. İlker Tari

Mechanical Engineering Dept., METU

Assoc. Prof. Dr. Derek K. Baker

Mechanical Engineering Dept., METU

Assist. Prof. Dr. Özgür Bayer

Mechanical Engineering Dept., METU

Prof. Dr. Şenol Başkaya

Mechanical Engineering Dept., Gazi University

Date: 08 – 09 – 2015

I hereby declare that all information in this document has been obtained and presented in accordance with academic rules and ethical conduct. I also declare that, as required by these rules and conduct, I have fully cited and referenced all material and results that are not original to this work.

Name, Last name : Serhat Bilyaz

Signature :

ABSTRACT

NUMERICAL INVESTIGATION OF CIRCULATING FLUIDIZED BED RISER HYDRODYNAMICS FOR CONCENTRATING SOLAR THERMAL RECEIVER APPLICATIONS

Bilyaz, Serhat

M.Sc., Department of Mechanical Engineering

Supervisor : Assoc. Prof. Dr. İlker Tari

September 2015, 113 pages

Various heat transfer fluids and thermal storage materials are considered for concentrating solar power systems to improve the storage capability of the system which compensates the fluctuating behavior of the solar resources. Solid particles can be a good alternative since they have high sensible heat capacity. In addition, they are cheap, environmentally benign and chemically and mechanically stable at high temperatures. In this thesis, hydrodynamics of circulating fluidized bed solar receiver was numerically investigated. 2D axisymmetric Eulerian-Eulerian (Two-Fluid Method) Computational Fluid Dynamics (CFD) model was constructed in open source software MFIX. Sand particles having diameter of $550\mu m$ was used in receiver. Model options and parameters were examined by modeling an experimental bubbling fluidized bed study. Grid independence, various drag models, effect of frictional and collisional behavior between wall and particles and effect of turbulence were examined in that model. Afterwards, experimental validation of final model

was performed by modeling an experimental circulating fluidized bed riser study. Wall boundary condition parameters, which are specular coefficient and particle-wall restitution coefficient were adjusted to fit the mass flux results with experimental data and final validated model was applied to final riser receiver design. Hydrodynamic parameters like solid mass flux distributions, void fractions, solid and gas velocities and pressure drop along riser were presented and discussed. Results were similar to the results in experimental validation study and reasonable in the light of information available in the literature.

Keywords: Concentrating Solar Power, Circulating Fluidized Bed Riser, Solid Particle Solar Receiver, Thermal Storage, Computational Fluid Dynamics

ÖZ

YOĞUNLAŞTIRILMIŞ GÜNEŞ ENERJİSİ ALICISI UYGULAMALARI İÇİN SİRKÜLASYONLU AKIŞKAN YATAĞIN HİDRODİNAMİĞİNİN SAYISAL İNCELENMESİ

Bilyaz, Serhat

Yüksek Lisans, Makina Mühendisliği Bölümü

Tez Yöneticisi : Doç. Dr. İlker Tarı

Eylül 2015, 113 sayfa

Yoğunlaştırılmış Güneş Enerjisi sistemlerinin ısı depolama kapasitelerinin artırılması, Güneş kaynaklarının değişkenliğini karşılama açısından önem arz etmektedir. Isıl depolama amacıyla farklı ısı transferi akışkanları veya ısı depolama malzemeleri incelenmektedir. Katı tanecikler, yüksek ısı kapasitesine sahip olmaları, ucuz, çevreye zararsız ve yüksek sıcaklarda mekanik ve kimyasal olarak dayanıklı olmaları nedeniyle hem ısı transferi akışkanı hem de ısı depolama malzemesi olarak düşünülmektedir. Bu tezde, sirkülasyonlu akışkan yataklı bir güneş alıcısının hidrodinamiği Hesaplamalı Akışkanlar Dinamiği (HAD) metodu ile incelenmiştir. Katı fazının da akışkan fazı gibi düşünüldüğü iki akışkan metodunu kullanan iki boyutlu aksisimetrik bir model açık kaynak kodlu MFX yazılımında oluşturulmuştur. Güneş alıcısı $550\mu\text{m}$ çapındaki kum tanecikleri için çalıştırılmıştır. Model parametreleri, deneysel bir kabarcıklı akışkan yatak çalışmasının modellenmesi ile incelenmiştir. Sayısal ağ bağımsızlığı, sürüklenme modelleri, taneciklerin duvar ile

olan arpıřma ve srtnme karakteristikleri ve trblans etkileri bu model ile incelenmiřtir. Daha sonra, gneř alıcısında kullanılacak model deneysel bir sirklasyonlu akıřkan yatak alıřmasının modellemesi ile belirlenmiřtir. Tanecik-duvar etkileřim modelinin yansıtıcılık ve tanecik-duvar geri sırama katsayılarının ayarlanması ile deneysel doęrulama saęlanmıřtır. Deneysel doęrulama sonucunda elde edilen model gneř alıcısı tasarımı iin kullanılmıřtır. Katı fazı akısının radyal daęılımı, bořluk yzdeleri, katı ve gaz hızları ve basın kaybı gibi hidrodinamik parametreler sunulmuř ve tartıřılmıřtır. Gneř alıcısı iin elde edilen sonular deneysel doęrulama modelinin sonuları ile paralel, literatr ile uyum halindedir.

Anahtar kelimeler: Yoęunlařtırılmıř Gneř Enerjisi Sistemleri, Sirklasyonlu Akıřkan Yataklar, Katı Tanecikli Gneř Alıcıları, Isıl depolama, Hesaplamalı Akıřkan Dinamięi

To My Parents

ACKNOWLEDGEMENTS

First, I would like to express my gratitude to Assoc. Prof. Dr. İlker Tarı for his valuable guidance and supervision throughout my thesis. His kind and supportive attitude was very helpful in my master study. I am also thankful to Assoc. Prof. Dr. Derek Baker for sharing his vision of solar energy and for his contributions on my academic background in his research group, CERES. I am grateful to Assoc. Prof. Dr. Murat Köksal and Ali Karakuş for their insightful discussions during my thesis studies.

I would like to thank my family for being a strong support in every sphere of my life. It is surely beyond doubt that they share a big part in my success. Additionally, I am thankful to my brother, Soner for his comments and contributions for my thesis.

It is impossible to mention my pleasure to my colleagues: Onur Özkan for having a great housemate for three years and his insightful discussions, Mine Kaya for being a great friend for eight years, Eylül Şimşek for her sincere friendship. I would like to highlight my gladness of working in a very warm lab atmosphere thanks to the great friendship of Göker Türkakar, Erdem Dursunkaya, Haydar Dirik, Mesru Altınöz, Berke Harmancı, Serdar Hiçdurmaz, Gizem Şencan, Ozan Erartsın and tea breaks with nice talks of Mustafa Yalçın.

This work is partially funded by METU Research Fund Project BAP-03-02-2015-007. The numerical calculations reported in this thesis were performed at TUBITAK ULAKBIM, High Performance and Grid Computing Center (TRUBA Resources).

TABLE OF CONTENTS

ABSTRACT.....	v
ÖZ	vii
ACKNOWLEDGEMENTS	x
TABLE OF CONTENTS	xi
LIST OF TABLES	xiv
LIST OF FIGURES	xv
NOMENCLATURE.....	xix
CHAPTERS	1
1. INTRODUCTION	1
1.1. Motivation	1
1.2. Solar Thermal Electricity	4
1.2.1. Concentrating Solar Power Collectors	4
1.2.2. Heat Transfer Fluids Used in CSP Systems	7
1.2.3. Thermal Storage in CSP Systems	9
1.3. Literature Review	10
1.3.1. Particles as a Storage Medium for Solar Thermal Energy	10
1.3.1.1. Free Falling Solid Particle Receiver.....	11
1.3.1.2. Circulating Fluidized Bed Solid Particle Receiver.....	14
1.3.2. Computational Modeling of Circulating Fluidized Beds	19
1.4. Thesis Overview	26
1.4.1. Objective	26

1.4.2.	Organization	26
2.	FUNDAMENTALS OF HYDRODYNAMICS IN FLUIDIZED BEDS	29
2.1.	Introduction	29
2.2.	Hydrodynamics.....	30
2.2.1.	Fluidization Parameters.....	30
2.2.2.	Classification of Particles.....	35
2.2.3.	Mapping of Fluidization Regimes.....	36
3.	COMPUTATIONAL FLUID DYNAMICS METHOD FOR NUMERICAL INVESTIGATION OF FLUIDIZED BEDS.....	41
3.1.	Introduction	41
3.2.	Fundamental Equations of Two-Fluid Method	43
3.3.	Gas-Solids Momentum Transfer	45
3.4.	Fluid Phase Stress Tensor.....	47
3.5.	Solid Phase Stress Tensor.....	48
3.5.1.	Plastic Regime (Dense Regime).....	49
3.5.2.	Viscous Regime (Dilute Regime)	50
3.6.	Turbulence Model.....	52
3.7.	Conclusion.....	54
4.	MODEL DEVELOPMENT	55
4.1.	Computational model	55
4.2.	Examination of Model Parameters	55
4.2.1.	Bubbling Bed Model Used for Investigation of Model Parameters.....	55
4.2.2.	Grid Independence	57
4.2.3.	Drag Models.....	59

4.2.4.	Wall Boundary Conditions.....	61
4.2.5.	Turbulence models.....	65
4.3.	Circulating Fluidized Bed Riser Model.....	69
4.3.1.	Modeling of an Experimental CFB Study.....	70
4.3.2.	Optimization of Wall Boundary Condition Parameters.....	73
4.3.3.	Final Model Applied to CFB Riser Solar Receiver.....	77
5.	RESULTS.....	81
5.1.	Mass Flow Rate.....	81
5.2.	Void Fraction.....	88
5.3.	Solid and Gas Velocities.....	93
5.4.	Pressure Drop.....	95
6.	CONCLUSION.....	97
6.1.	Summary.....	97
6.2.	Concluding Remarks.....	99
6.3.	Future Work.....	102
	REFERENCES.....	105
	APPENDIX: INSTANTANEOUS VOID FRACTION CONTOUR PLOTS OF DIFERENT REGIONS FOR 118-119 SECONDS TIME RANGE.....	111

LIST OF TABLES

TABLES

Table 1 Some solid particle properties for thermal storage medium for solar receiver	16
Table 2 Summary of CFD studies of circulating fluidized beds loaded with Geldart B type particles.....	25
Table 3 Properties of glass beads	56
Table 4 Simulation parameters used for modeling Mastellone's case.....	72
Table 5 Physical properties of sand.....	79
Table 6 Riser simulation parameters	80
Table 7 Pressure drop per unit length for different regions of the receiver.	96

LIST OF FIGURES

FIGURES

Figure 1 Available CSP technologies (a) Central receiver (Solar Tower) (b) Parabolic Trough Receiver (c) Linear Fresnel Receiver (d) Parabolic Dish Receiver (Adapted from [9]).....	7
Figure 2 Free falling particle solar receiver of Hruby (Adapted from [14]).....	12
Figure 3 A concentrating solar power system with solid particle thermal storage (Adapted from [6]).....	14
Figure 4 Dense suspension solar receiver of Flamant. 1) Riser solar receiver; 2) Fluidized bed particle distributor; 3) Receiving fluidized bed; 4) Suspension return (Adapted from [6]).....	17
Figure 5 Circulating fluidized bed solar receiver of Brems 1) Riser solar receiver; 2) Cyclone; 3) Heat exchanger (Adapted from [24]).....	18
Figure 6 Schematic of a typical circulating fluidized bed (Adapted from [39]).....	30
Figure 7 Voidage of randomly packed uniformly sized particles having various sphericities (Adapted from [40]).....	32
Figure 8 Pressure drop with respect to superficial gas velocity (Adapted from [40])	33
Figure 9 Schematic representation of equilibrium of primary forces on a single particle when the particle has terminal velocity (Adapted from [41]).....	34
Figure 10 Geldart powder classification diagram for fluidization by air at ambient conditions (Adapted from [40]).....	36
Figure 11 Generalized map of fluidization regimes (Adapted from [40]).....	38
Figure 12 Progressive change in fluidization regime with change in gas velocity (Adapted from [40]).....	39

Figure 13 Schematic representation of different fluidization regimes (Adapted from [42]).....	40
Figure 14 Various approaches for computational modeling of gas-solid flows	42
Figure 15 Schematic of plastic and viscous regimes of granular phase as a function of void fraction (Adapted from [44]).....	49
Figure 16 Schematic of simple fluidized bed used for model optimization and experimental validation (Adapted from [59])	56
Figure 17 Radial distribution of time-averaged void fraction at 8cm height for grid resolution study	58
Figure 18 Percentage void fraction deviations along radial location at 8cm height for different meshes with respect to finest mesh	59
Figure 19 Radial distribution of time-averaged void fraction at 8cm height for different drag models	61
Figure 20 Illustration of relationship between slip condition and surface characteristics for solid particles (Adapted from [45])	62
Figure 21 Radial distribution of time-averaged void fraction at 8cm height using Johnson&Jackson partial slip wall boundary condition with different specularly coefficients	64
Figure 22 Radial distribution of time-averaged void fraction at 8cm height using Johnson&Jackson partial slip wall boundary conditions with different particle-wall restitution coefficients	65
Figure 23 Radial distribution of time-averaged void fraction at 8cm height for investigation of k-e turbulence model and Ahmadi model and Jenkins wall boundary condition.....	67
Figure 24 Radial distribution of time-averaged void fraction at 8cm height for investigation of wall-restitution coefficients for the best model selected. Experimental data are given with the associated error bars.	68

Figure 25 Time averaged void fraction along bed height for data spatially averaged across the radial location of the bed for comparison of the best model with the experimental data. Experimental data are given with the associated error bars.	69
Figure 26 Core annulus flow regime in circulating fluidized bed risers a) For low superficial gas velocities, b) For high superficial gas velocities.....	70
Figure 27 Schematic of CFB system used in Mastellone's study. (1) riser; (2) and (3) recirculation standpipes; (4) solids control butterfly valve; (5) feed hopper; (6) three ways valve; (7) and (8) cyclones (Adapted from [68])	71
Figure 28 Radial distribution of solid mass flux at 4.23m height of Mastellone's case for various specularly coefficients	73
Figure 29 Time averaged and radially averaged void fraction along the riser for various specularly coefficients.....	74
Figure 30 Radial distribution of solid mass flux at 4.23m height of Mastellone's case for various particle-wall restitution coefficients when $\phi = 0.001$	75
Figure 31 Radial distribution of solid mass flux at 4.23m height of Mastellone's case for various particle-wall restitution coefficients when $\phi = 0.005$	75
Figure 32 Time averaged and radially averaged void fraction along the riser for the best case.	76
Figure 33 Schematic of circulating fluidized riser solar receiver	77
Figure 34 Initial condition of 2D axisymmetric riser model	78
Figure 35 Time variation of radially averaged solid mass flow rates at different heights of the riser.....	82
Figure 36 Averaged solid mass flow rates in 0-1 seconds time range.....	83
Figure 37 Averaged solid mass flow rate for $y=0.2\text{m}$ and $y=0.5\text{m}$ cases in 1-5 seconds	84
Figure 38 Averaged solid mass flow rate for $y=1\text{m}$ and $y=1.1$ cases in 1-5 seconds	84

Figure 39 Averaged solid mass flow rate for $y=0.2\text{m}$ and $y=0.5\text{m}$ sections in 115-120 seconds	85
Figure 40 Averaged solid mass flow rate for $y=1\text{m}$ and $y=1.1\text{m}$ sections in 115-120 seconds	86
Figure 41 Radial distribution of mass fluxes at heights of $y=0.5\text{m}$ and $y=1\text{m}$ of the riser.....	87
Figure 42 Radial distribution of mass fluxes in different time ranges for beginning and ending lines of heat transfer region	88
Figure 43 Radial distribution of void fraction at heights $y=0.2\text{m}$, 0.5m , 1m and 1.1m of the riser.....	89
Figure 44 Radial distribution of void fractions in different time ranges for beginning and ending lines of heat transfer region	90
Figure 45 Instantaneous and time averaged void fraction contour plots for riser region upwards of 0.4m . a) $t=30\text{s}$; b) $t=60\text{s}$; c) $t=90\text{s}$; d) $t=120\text{s}$; e) Time averaged in the range of $0-120\text{s}$	91
Figure 46 Radially averaged and near wall void fractions along the riser	92
Figure 47 Radial distribution of solid vertical velocities at various heights of the riser	93
Figure 48 Radial distribution of gas vertical velocities at various heights of the riser	94
Figure 49 Pressure drop along the riser.....	95

NOMENCLATURE

Symbols	Unit	
Ar	-	Archimedes number
A_{riser}	m^2	Cross sectional area of the riser
c_1 and d_1	-	Parameters to adjust Syamlal drag model
C_D	-	Drag coefficient
d	m	Diameter
d^*	-	Dimensionless particle diameter
D	W/m^2	Dissipation of granular energy due to inelastic collisions
\bar{D}	s^{-1}	Strain rate tensor
e_w	-	Particle-wall restitution coefficient
f_g	N/m^3	Body force excluding force due to gravity
g	m/s^2	Gravity
g_0	-	Radial distribution function
G_s	$\frac{kg}{m^2s}$	Solid circulation rate
\bar{I}	-	Identity tensor
I_{gm}	N/m^3	Momentum transfer between gas and solid phases
I_{km}	N/m^3	Momentum transfer between different solid phases
J	W/kg	Collisional dissipation
k_1	J/kg	Turbulent kinetic energy for gas phase
k_2	J/kg	Turbulent kinetic energy for solid phase
\bar{m}_s	kg/s	Radially averaged solid mass flow rate
n	-	Unit normal from the boundary
N_f	Pa	Normal friction component of stress
P	Pa	Pressure
q_{PT}	W/m^2	Flux of granular energy

Re	-	Reynolds number
S_c^b	Pa	Force per unit area on the wall due to particle-wall collisions
\overline{S}_g	Pa	Stress tensor
U	m/s	Superficial velocity
u_{sl}	m/s	Slip velocity at wall
u^*	-	Dimensionless velocity
u_t	m/s	Terminal velocity of particles
V	m/s	Vertical velocity
V_{rm}	m/s	Terminal velocity of particles for Syamlal drag model
v'	m/s	Fluctuating velocity

Greek letters

β_{gs}	$\frac{kg}{m^3s}$	Drag coefficient for solid phase due to gas/solid relative velocity
δ	deg	Angle of friction between wall and particles
ϵ	-	Void fraction
ϵ^*	-	Critical void fraction
ϵ_1	W/kg	Dissipation of turbulent kinetic energy for gas phase
ϵ_2	W/kg	Dissipation of turbulent kinetic energy for solid phase
η	-	Particle-particle restitution function
κ_m	$\frac{W}{mK}$	Solids conductivity
μ	$Pa.s$	Viscosity
μ_b	$Pa.s$	Solids bulk viscosity
$\mu_{f,max}$	$Pa.s$	Maximum granular viscosity
μ_1^t	$Pa.s$	Gas turbulent viscosity/eddy viscosity
Θ	m^2/s^2	Granular temperature

ϕ	-	Specularity coefficient
ϕ_f	deg	Angle of internal friction
ϕ_w	deg	Angle of internal friction for particle-wall collisions
Φ_s	-	Sphericity
Π_ϵ, Π_k	W/m^3	Turbulence interaction terms
ρ	kg/m^3	Density
σ	Pa	Viscous stress
$\bar{\sigma}$	Pa	Viscous stress tensor
σ_c	Pa	Stress tensor due to collision
σ_f	Pa	Stress tensor due to friction
τ_{12}^x	s	Particle relaxation time
τ_1	s	Time scale of turbulent eddies

Subscripts

crit	Critical
g	Gas phase
inlet	Inlet
m	m th solid phase
mf	Minimum fluidization
p	Particle
pb	Packed bed
s	Solid phase

Abbreviations

CFB	Circulating Fluidized Bed
CFD	Computational Fluid Dynamics
CSP	Concentrating Solar Power
DAR	Direct Absorption Receiver
DEM	Discrete Element Method

DNS	Direct Numerical Simulation
DSMC	Direct Simulation Monte Carlo
EMMS	Energy Minimization Multi Scale
FCC	Fluid Catalytic Cracking
HTF	Heat Transfer Fluid
LBM	Lattice Boltzman Method
LDA	Laser Doppler Anemometry
MPPIC	Multiphase Particle-in-cell Method
PCM	Phase Change Material
PDA	Phase Doppler Anemometry
PTC	Parabolic Through Collector
RMS	Root Mean Square

CHAPTER 1

INTRODUCTION

1.1. Motivation

Renewable energy has become popular in recent years to compensate the increasing power demand of the World. Solar energy has been considered for electricity generation purposes for many years because it is available and has very low impact on carbon footprint compared to conventional fossil fuel thermal power plants. Mainly two different approaches exist for electricity generation from solar energy utilization which are photovoltaic systems and solar thermal systems. In photovoltaic systems, solar radiation is converted to electricity electrochemically. While, in Concentrating Solar Power (CSP) systems, solar radiation is used as heat source of a heat engine cycle. In CSP, solar radiation is usually concentrated through special collectors which enable reaching very high temperatures in the heat engine cycle by providing high heat fluxes. Renewable energy sources like solar and wind are not available every time, so that it becomes hard to maintain stable operation in an STS. Storage or back-up mechanisms should be added to such systems to compensate for the fluctuating behavior of the source in order to provide continuous and stable electricity generation. Considering the solar energy, solar thermal systems has advantages over photovoltaic systems due to their scalability and their ability to store thermal energy. Thermal energy storage systems can make the CSP systems more cost effective by compensating the cloudy hours of the day or maintaining the electricity generation some time after sunset.

Several alternatives are considered for thermal storage in CSP systems. While external heat storage units are considered in the system, special designs exist

providing the storage by selecting an appropriate Heat Transfer Fluid (HTF). Selection of storage material is an essential step and the selected medium should satisfy some requirements for better performance. Naturally, high energy density and high heat transfer rate between heat transfer fluid and storage material are key considerations. In addition to these fundamental criteria, the medium should be mechanically and chemically stable in operating conditions and compatible with the heat transfer fluid and the other equipments. Reversibility of the HTF in each charge-discharge cycle is very important to maintain the system cheaply. It is also required to have low cost, low thermal losses and low environmental impact [1].

Selection of heat transfer fluid determines the operating temperature range and storage capability of the system [2]. Water, oil based fluids, air or molten salt are generally used as HTFs. Advanced HTFs like nano-particle suspensions are under investigation. Water is free and environmentally harmless fluid, but direct steam generation in receivers has several disadvantages. Main problem of using water is the control of the flow which is difficult due to two-phase flow phenomenon. Transition regimes of the flow are hard to predict due to fluctuation of solar resources. Moreover, temperature and pressure gradients in the receiver may cause defects in the system [3]. Oil based organic fluids have low operating temperatures which prevents the use of efficient high temperature power cycles. These kind of fluids are expensive and not environment-friendly. Moreover, some of them can be flammable at high temperatures [2]. Molten-salts are recently used and commercially applied HTFs for thermal storage. However, they have high freezing temperature which may put the system in trouble during the night conditions. Moreover, operating temperature of molten-salts are limited to 500-600°C, beyond that range the fluid becomes instable [4]-[5]. So that, different HTFs are taken into consideration in order to reach high temperatures with no physical or chemical stability problems. Mixtures of air and solid particles is another viable HTF alternative. Using solid particles as a sensible heat storage medium is very promising and under-development due to several advantages. Sand-like particles or silicon carbide-like powders have advantages of high sensible heat capacity, low cost, and mechanical and chemical

stability at very high temperatures. Using solid particle solar receiver concept with over-sized solar tower concentrators, very high operating temperatures up to ~800-900°C can be possible which will allow usage of very efficient thermodynamic cycles such as supercritical steam or CO₂ cycles [6].

Mainly, two different concepts of solid particle receivers are taken into consideration which are free falling receivers where particles are directly irradiated by the solar source and fluidized bed receivers where radiation is absorbed by a fluidized bed or circulating fluidized bed riser tubes. Tubes can be glass or opaque metals. Flamant used AISI310S stainless steel which is placed into a cavity insulated by Insulfrax [6]. While particles are directly irradiated and thermal losses can be lowered in free falling receiver concept, solid flow control is hard since the velocity of the particles are determined by the terminal velocity. Fluidized bed or circulating fluidized riser receiver concept provides advanced control of solid mass flow rates which may be required under different solar resource conditions. Moreover, circulating fluidized bed is a well-developed technology for coal-burning power plants which facilitates process integration and field application of the system. Flamant [6] proposed a novel design similar to fluidized riser receiver. In his design, a dense gas-particle suspension is slowly rising in the receiver which prevents high velocity and mechanical energy consumption of solid circulation and provides higher wall-particle heat transfer coefficient compared to conventional operating conditions of circulating fluidized beds.

Considering the necessity of improvements on the storage capability and scalability of CSP systems mentioned in the motivation part, developing a numerical model for fluidized bed solar receiver is a significant research path which allows deep examinations of hydrodynamics and heat transfer mechanisms in the system. In light of the literature review, it is observed that the first important part of the numerical work is modeling hydrodynamics of the system because it will be a strong base for further heat transfer studies. Computational model will allow parametric studies for optimization of such systems which are harder and more expensive to perform via

experimental work. Therefore, this study aims to develop a reliable and stable first stage model to give an idea about feasibility of the system and draw a pathway for further investigations about different operating conditions of the system.

1.2. Solar Thermal Electricity

Electricity production from solar thermal energy is usually done by power plants which collect solar radiation and use the utilized heat to operate a power cycle. Usually the solar irradiation is concentrated by reflecting collectors to line or point type receivers. So that, the solar radiation irradiating a large area can be focused to a smaller receiver area which enables reaching high temperatures and high heat fluxes to operate heat engines. Concentrating collectors track the sun during the day and utilize only direct (beam) part of the solar radiation. Since beam radiation is scattered by atmosphere in cloudy days, CSP systems become useless in those days. Concentrating collectors can be classified based on their focusing principle. Fresnel collectors and parabolic trough collectors (PTC) are focusing the solar radiation on linear pipe receivers and solar towers and parabolic dish technologies are using point receivers [3] [7] [8]. Operating temperatures are relatively higher in point focusing technologies than line focusing ones.

1.2.1. Concentrating Solar Power Collectors

PTCs are the most common and developed collector type among others. Parabolic trough-shaped mirrors track the sun and collect the beam radiation to the receiver pipe passing through the focus line of the mirrors. This assembly is constructed in series and parallel arrays to heat up the HTF up to 400°C in the absorber tubes [4]. The axis of the collector can be aligned for east-west, north-south or two axis tracking. Usually north-south axis tracking is used to be able to track the sun better during the day. Heat transfer fluid used in PTCs are mostly oil based thermal fluids due to low-mid operating temperatures. Steam and molten salt fluids are also in consideration. PTC is the most commercially developed and proven CSP technology

due to long term research and development efforts in the United States and Europe. Plenty of engineering experience has been gained especially in California and in Spain [3]-[4].

Linear Fresnel Reflectors reflect the sunlight to a downward facing linear receiver by long rows of mirrors. Simple design and low investment costs of fresnel systems make them favorable, but they are less efficient than PTC or other collectors. It is difficult to have storage for these systems due to low operating temperatures, but they can be considered for low temperature systems, heating purposes or direct steam generation [4][9].

Parabolic dish collectors concentrate the solar beams to a focal point at the center of a dish which consist of multiple parabolic mirrors. The system usually has a Stirling engine at the focal point to obtain electricity. This kind of systems has higher efficiency among others but have low compatibility. Storage and hybridization of these systems are difficult [9]. Cooling water requirement is eliminated by the system because the Stirling engine is cooled by dry radiators. Since these systems are more modular than other CSP systems, they can be used for distributed power generation [4].

Solar towers concentrate solar radiation by thousands of 2 axis sun tracking flat mirrors called "heliostats". A receiver is placed at the top of the tower where the sunrays are collected. Concentration ratios are very high so that, temperatures up to 1000°C can be achieved at the receiver. This conceptually allows usage of advanced high efficiency power cycles like combined cycles and supercritical steam/gas turbines [4]. Due to high flux of radiation arriving the receiver, thermal storage becomes possible and useful for these systems. Different receiver designs are considered for solar towers such as volumetric air receivers, tubular gas/liquid receivers or solid particle receivers [5]. According to different receiver types, different HTFs like air, molten-salt, water and solid particles are considered for the tower systems.

Currently commercial experience on solar tower receivers are limited, but a decrease in cost of electricity is estimated [4]. Due to high concentration ratio and thermal storage capability, solar tower technology shows great potential for energy market in the future. However, significant amount of R&D effort is still needed to improve efficiencies, increase durability, reliability and reduce investment and operation and maintenance costs. Optimization of heliostat technology, development of advanced high temperature receivers, investigation of different HTFs for high operating temperatures with thermal storage capability and integration of advanced power generation cycles are compulsory [4]. Because of that, the objective of this thesis is to work on a receiver technology which is reliable at high temperatures and having remarkable thermal storage potential.

Schematics for four different solar thermal receiver technologies are provided in Figure 1 [9].

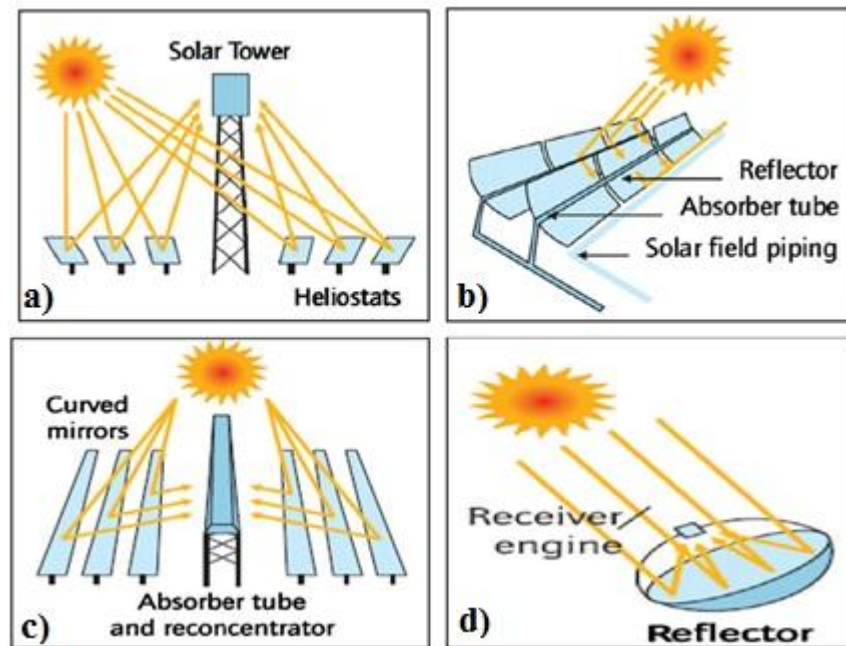


Figure 1 Available CSP technologies (a) Central receiver (Solar Tower) (b) Parabolic Trough Receiver (c) Linear Fresnel Receiver (d) Parabolic Dish Receiver (Adapted from [9])

1.2.2. Heat Transfer Fluids Used in CSP Systems

HTFs in CSP systems have significant roles on efficiency and operating principles of the system. There are many problems related to the selection of HTF. In addition, effective heat transfer; mechanical, physical and chemical stability at desired operating temperatures, storage capability, ease of flow control and cost are other important parameters to be considered. Air, water/steam, thermal oils, molten salts, liquid metals and solid particles are discussed in this section regarding the parameters mentioned above.

Using air as a HTF in CSP systems is not common. Air has no limit of operating conditions, but it has low thermal conductivity which makes heat transfer difficult [10].

Water is considered as HTF for direct steam generation purposes. Steam can be used directly in conventional Rankine cycle as the working fluid which prevents the usage of a secondary HTF. However, there are challenges in direct steam generation. Complex two phase flow phenomena makes the flow control difficult. Flow rates should be high to avoid stratified flow in the tube [3]. Two phase flow in the collector pipe causes temperature gradients in the pipe causing thermal stresses and mechanical defects. Corrosion of metallic pipes are also another issue to be considered for usage of high temperature steam [10].

Synthetic thermal oils are considered due to ease of flow control and good thermal conductivity. However, maximum operating temperature is limited to about 400°C with these oils. This prevents their use in high temperature CSP systems like solar towers. Thermal oils are expensive and not suitable for use as a storage medium, thus a heat exchanger is needed to transfer heat to another working fluid which cause some additional irreversibilities [10].

Molten salts are seriously considered as HTF due to their relatively low cost, good thermal conductivity and thermal storage capability. Most of the considered salts are nitrate based. Because the nitrate salt production is restricted, there is a need for alternative salts [10]. Stability issues occur at high temperatures above 600°C, thus operating temperatures up to 1000°C are not feasible. Corrosion in pipes should be considered for molten salts. Salts are usually preferred due to their thermal storage capability, however additional heating might be necessary when the medium temperature drops under the freezing temperature, especially in absence of solar resource for a long time.

Liquid metals are considered due to their good thermal conductivity, low viscosity and wide operating temperature range. For example, operating temperature range for liquid sodium is 98-883°C. However, they are less preferable for thermal storage compared to molten salts due to their low heat capacities [10].

The use of solid particles as HTF or thermal storage medium has been examined due to several advantages. Sand like ceramic particles can keep their mechanical and chemical stability at high temperatures up to 1000°C . Due to high heat capacity of particles, they are considered as good alternatives for thermal storage. HTF itself can be a storage medium, or heated particles can be collected in storage tanks. Particles are usually cheap materials and they are environmentally friendly. Heat absorption is done either by free falling solid particles in a receiver where particles are directly exposed to the direct sunlight or fluidization in bed or riser systems [5][11].

1.2.3. Thermal Storage in CSP Systems

Renewable energy is not usually considered as primary energy source to satisfy the entire electricity demand due to the fluctuating behavior of the source. Solar resources are more predictable and the solar energy is suitable for thermal storage which is efficient and relatively cheap compared to other storage technologies like electrochemical storage [4]. Solar energy can be stored during the day and thermal inertia can be used at night to maintain the operation of a heat engine. Storage media can be separated from the receiver or considered as the same HTF medium. Different storage materials and technologies are considered for thermal storage of CSP systems.

There are several criteria to optimize the thermal storage [1][12], namely

- High energy density in the storage medium
- Good heat transfer between the storage medium and the heat transfer fluid
- Mechanical and chemical stability at desired operating temperatures
- Chemical compatibility between interacting fluids and surfaces
- Reversibility for large number of charge/discharge cycles
- Low thermal losses
- Low cost
- Low environmental impact

Materials used for storage are classified according to storage mechanisms: sensible heat storage, latent heat storage and chemical heat storage. Sensible heat storage materials are most commonly used and most developed ones since there are plenty of available cheap materials. Latent heat storage materials or Phase Change Materials (PCM) have much higher storage capacity than sensible heat storage, but they have poor heat transfer characteristics. Chemical heat storage has also high storage capacity, but it requires complex reactors to maintain stability and long-term durability [1][13].

Sensible heat storage materials can be solid phase such as sand-rock like minerals, concrete, fire bricks or liquid phase such as oils, liquid metals and molten salts. Usually liquid metals and molten salts have better thermal conductivity than sand-rock like solid materials. However, liquid metals are chemically unstable which requires extra expenditure for safety issues. Molten salts are the most common materials for storage media due to good chemical stability at high temperatures up to 500°C. However, they have melting temperatures near 80-100°C. This means that when the temperature of salt drops below that point, additional heating would be necessary to avoid solidification [13]. In addition to that, stability issues occur in molten salts for temperatures above 500°C. Therefore, it seems that sand-rock or ceramic like particles can be more suitable for very high operating temperatures up to 1000°C.

1.3. Literature Review

1.3.1. Particles as a Storage Medium for Solar Thermal Energy

Two main approaches exist for usage of solid particles as heat transfer and thermal storage material for a CSP system. First one is using free falling solid particle receivers in which solid particles are freely falling in a receiver and has direct contact with concentrated solar radiation. In the second approach, solid particles are circulating in a fluidized bed where the concentrated solar beams are irradiating a

CFB riser and heating up the particles. For both cases, the purpose is heating up the particles to high temperatures, and transferring the heat from particles to another working fluid which can be used in gas/steam turbines. These kinds of studies started in early 80's, but have not been developed much ever since, thus further improvements are required. In the rest of this section, the literature of this field is summarized.

1.3.1.1. Free Falling Solid Particle Receiver

In this approach, particles are freely falling in a receiver and exposed to direct solar radiation. Particles are falling as a thin curtain and are heated up to high temperatures. Usually, heated particles are stored in an insulated tank and the heat extracted to other HTFs (such as air or water) via heat exchangers to be used in thermodynamic cycles. Cold particles are moved to another tank and finally carried to the top of the receiver by pneumatic or mechanical carriers. Since particles are mostly directly exposed to solar radiation in this systems, heat transfer investigations should include a proper radiative transfer model. Force convection would also be of interest depending on wind conditions and the design of the receiver.

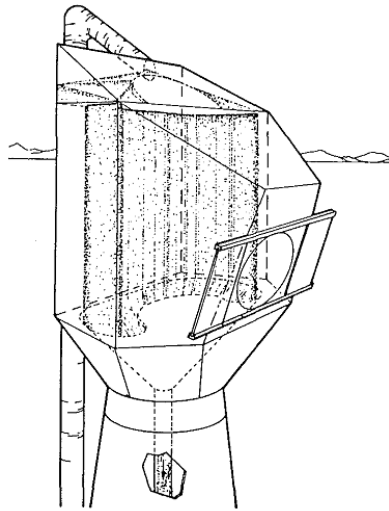


Figure 2 Free falling particle solar receiver of Hruby (Adapted from [14])

This approach was started in early 80's in Sandia National Laboratory. Hruby et al. [14] examined flow characteristics and convective heat transfer numerically and experimentally. Absorptivities of spherical Aluminum Oxide particles are determined when they are exposed to direct solar radiation. Speed and temperature of the heated and unheated particles was recorded in that study. Free falling particle receiver of Hruby is shown in Figure 2 [14].

Rightley et al. [15] characterized heat transfer in a free-falling particle receiver. Experimental measurements were performed for directly irradiated particle curtain in high-flux solar furnace. Radiative heat flux, particle temperatures and extinction coefficient of Directly Absorbing Receiver (DAR) were investigated. Radiative transfer was also solved by a theoretical model based on discrete ordinates approximation. Theoretical model showed good agreement with experimental measurements in terms of total incident and transmitted heat fluxes and average exit temperature of particles.

Chen et al. [16] performed computational fluid dynamics analysis of free falling particles in a solar receiver and compared their results with experimental data of Hruby [14]. Their 3D model was established in Fluent. Realizable $k-\epsilon$ model is used to determine turbulence characteristics and discrete ordinate method is used to couple

radiative transfer to the heat transfer model. Particle interactions were neglected. Results were compared for two extreme cases of the receiver geometry which are maximum bottom opening and no bottom opening to show the negative effect of bottom opening. Cavity efficiencies and particle outlet temperatures were compared and better results were shown for the closed bottom case. In addition, particle size effect was examined in a range of 200-600 micrometer. It was concluded that smaller particles can reach higher temperatures.

Kim et al. [17] developed a CFD model for free-falling solid particle receiver to examine wind effect. Ceramic particles of approximately 687 μm diameter were used. CFD model was based on two fluid model and developed in MFIIX. Study was called "cold study" in which heat transfer was not considered and stated as future work. Wind effect was considered for different angles of attack to the receiver and various speeds. Particle losses were reported and the smaller receiver model was considered as a base for a scale-up model.

Nowadays, this research has been started again in Sandia National Laboratory. Siegel et al. [18] established a new solid particle solar receiver prototype and performed on-sun tests. In addition to the set-up a Fluent CFD model was also established and verified with experimental results. Solar heat input to the receiver was 1.58-2.51 MW_{th} . After examining particle speeds, particle outlet temperatures, and the receiver efficiency, maximum error rate of 10% was obtained between experimental and numerical results.

“High Temperature Falling Particle Receiver” project was started in 2012 by Sandia National Laboratories in cooperation with other several partners and awarded 4.4 million USD funding by U.S. Energy Department, Sun Shot. The project is planned to be finalized in 2015. [19]

1.3.1.2. Circulating Fluidized Bed Solid Particle Receiver

In this approach, solid particles are fluidized and circulated in a bed. Concentrated solar beams irradiate the Circulating Fluidized Bed (CFB) riser and heat up the particles. Circulating air is heated up by the particles in the riser and at the exit of the riser air is extracted by a cyclone and used in a gas turbine to obtain electricity. Alternatively, solid particles can be extracted and stored in a hot storage tank. Solid particles have a high heat capacity so that thermal energy can be stored in particles. In the present thesis, the fluidized bed is considered to be well isolated and in cases of insufficient solar radiation, all openings of the bed exposed to the atmosphere will be covered with insulation and fluidized bed will be considered as a storage bed which is expected to extend the operation of electricity generation system. A conceptual example of a concentrated solar power system with solid particle storage is shown in Figure 3 [6].

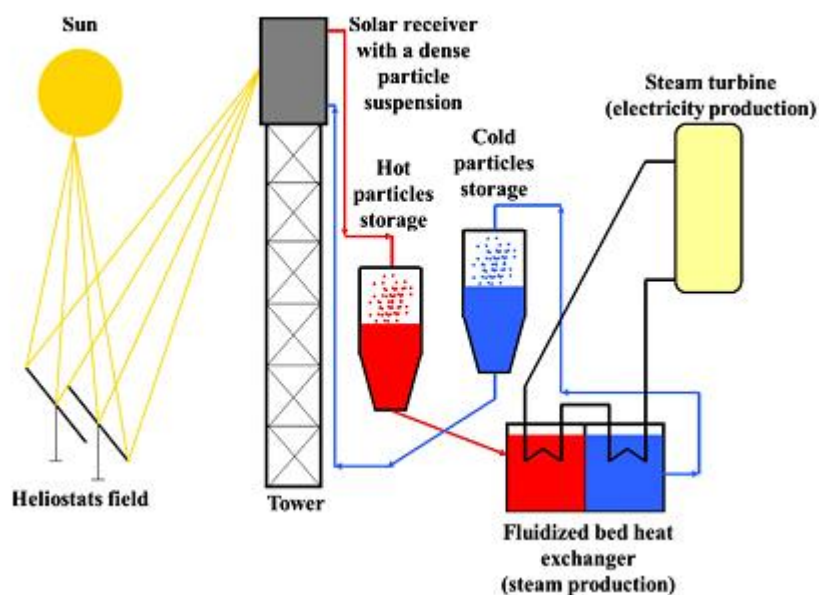


Figure 3 A concentrating solar power system with solid particle thermal storage
(Adapted from [6])

First studies in that topic was started in early 80's. Flamant [20] designed a fluidized bed solar receiver for gas heating and chemical energy storage and investigated heat

transfer in the bed theoretically and experimentally. His design included a transparent bed which transmits the solar radiation to solid particles. Flamant studied non-transparent version of his design as well. Experiments were performed to examine radiative transfer to the particles and extinction coefficient and mean penetration distance. Detailed results were obtained for particle and gas temperature profiles, particle flux density profiles and radiative heat fluxes. Theoretical results coincided with experimental results in minimum fluidization conditions.

Ma et al. [21] examined different particle mediums for the solid particle solar receiver concept. First law and second law efficiencies and storage effectiveness parameters were considered to comment on the feasibility of these systems. Their receiver design was similar to a circulating fluidized bed receiver where the storage was supplied by hot and cold storage tanks. Compared to other storage medias like liquid metal, molten salt or oil, solid particles like ash, sand, refractory brick and concrete were stable and cheap. It was reported that particle thermal energy storage cost in the range of \$ 5-7/ kWh_{th} which showed more than %75 reduction in cost of thermal storage compared to current systems. The achieved cost was even less than cost target of SunShot, \$ 15/ kWh_{th} . Ma et al. [22] also compared different particles to show advantages and disadvantages of them, which are tabulated in Table 1 [22].

Table 1 Some solid particle properties for thermal storage medium for solar receiver

Material	Density (kg/m³)	Heat capacity (J/kgK)	Advantage	Disadvantage
Silica Sand	2610	710	Stable, abundant, low cost	Low conductivity
Quartz Sand	2650	755	Stable	Medium
Alumina	3960	880	Stable	High cost
Ash	2100	720	Stable, abundant, low cost	Identification of suitable ash
Silicon Carbide	3210	670	High conductivity	High erosion, high cost
Graphite Pebble	2250	710	High conductivity	Oxidation, attrition

Flamant [6] designed novel dense suspension circulating fluidized bed solar receiver and examined heat transfer experimentally in a solar furnace. His design is shown in Figure 4. Dense silicon carbide suspension with 64 micrometer particles were used. Particles were exposed to solar flux of 200-250 kW/m² and temperature rise of 50-150 °C was observed. Wall to suspension heat transfer coefficients of 140-500 W/m²K were obtained for different conditions. Higher the operation temperatures, higher the heat transfer coefficients were expected. Suspension had heat capacity characteristics similar to liquid heat transfer fluids. Since silicon carbide material is stable at high temperatures, high temperature operating conditions allow the usage of efficient thermodynamic cycles such as supercritical steam and supercritical carbon dioxide cycles.

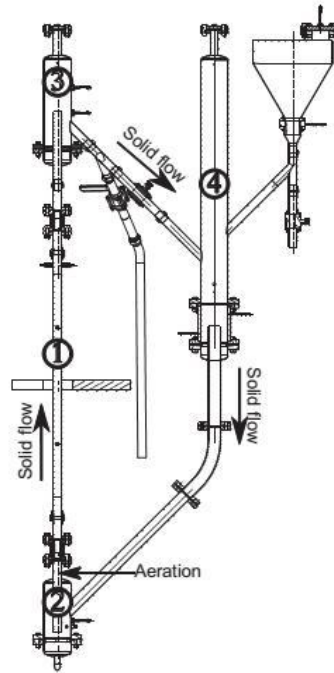


Figure 4 Dense suspension solar receiver of Flamant. 1) Riser solar receiver; 2) Fluidized bed particle distributor; 3) Receiving fluidized bed; 4) Suspension return (Adapted from [6])

Pitie et al. [23] investigated heat transfer characteristics and storage capability of CFB solar receiver. In the study, feasibility of PCM was investigated and wall to bed heat transfer coefficient was obtained experimentally. Results were compared with empirical predictions of Molodtsov-Muzyka and Golriz-Grace and good agreement was obtained. Optimum particle size was determined as $<400 \mu\text{m}$. Heat transfer coefficients were found around $60 \text{ W/m}^2\text{K}$ in low solid mass flux cases and $350 \text{ W/m}^2\text{K}$ in high solid mass flux cases. For both cases radiative heat transfer were not considered. It is mentioned that PCM particles has advantages over SiC or sand particles. Using non-PCM particles, temperature difference between the wall and the riser was progressively increasing during heating, but for the PCM it was constant and fixed to its maximum. Moreover, required circulation rate was higher for non-PCM than PCM which may cause high operating costs due to high energy

consumption. Current limitation of PCM was reported as hardness of manufacturing smaller particles ($<400\ \mu\text{m}$) and solidification on non-heating parts of riser wall.

Brems et al. [24] investigated wall-to bed heat transfer experimentally. The study was performed to be used in various systems, including solar energy capture. This concept is shown in Figure 5. Different flow regimes were noticed and Molotsof-Muzyka model was used. Since the results were highly sensitive to solid mass flux, Golriz-Grace model was modified according to solid mass fluxes and results were obtained accordingly. Future work was announced as modifying the heat transfer results according to particle contact time determined by Positron Emission Particle Tracking.

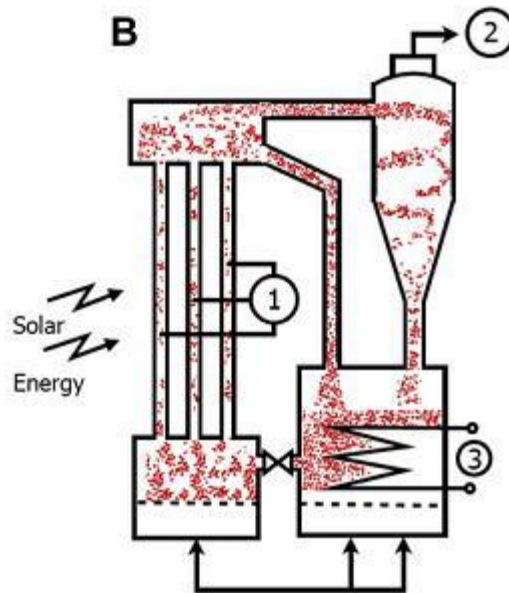


Figure 5 Circulating fluidized bed solar receiver of Brems 1) Riser solar receiver; 2) Cyclone; 3) Heat exchanger (Adapted from [24])

"Concentrated Solar Power in Particles" project has been started by strong partners as Centre National de la Recherche Scientifique (CNRS) and Zurich ETH with funding of European Commission in 2011 [25]. The project is still on progress and aiming to improve the technology and design an innovative solar power system with solar tower receiver. A $100\text{-}150\text{kW}_{\text{th}}$ prototype will be constructed in CNRS which

will operate in 500-750°C operating temperature range and the project is aiming to reach 70% thermal efficiency. Theoretical analysis will be performed for economic feasibility of industrial scale models (~10-50 MW_e).

1.3.2. Computational Modeling of Circulating Fluidized Beds

There are different approaches to computational modeling of fluidized beds. Computational Fluid Dynamics (CFD) methods are popular among these models. Gas phase is considered in classical approaches and solid phase is either tracked by Lagrangian framework or approximated to fluid phase by use of proper closure relations. The second approach is also called Eulerian-Eulerian method or two fluid method. Details of these models are explained in Chapter 3. Since Circulating Fluidized Bed (CFB) systems are large systems and contain high amount of particle load, it is hard to track individual particles due to computational limitations. Therefore, two fluid method is a common approach for modeling CFB systems. In this section studies using this approach are reviewed, because two fluid method is used in this thesis.

CFB systems are widely used for fluid catalytic cracking (FCC) systems or CFB combustion systems. Therefore, most of the studies in the literature are done for FCC particles or sand. Since FCC particles are in Geldart A classification and sand is in Geldart B [26], it is not very realistic to model both of them in the same manner. Since sand particles are used in this thesis, only the studies performed with Geldart B type particles are covered in this section.

Enwald [27] summarized Eulerian two phase flow theory in fluidization applications. It is an important paper due to derivations of the equations and review of applications in bubbling beds or CFBs. For CFB applications, it was reported that most of the studies were using kinetic theory of granular flows. It was also mentioned that most of the studies does not include turbulence models.

Tsuo and Gidaspow [28] developed a computational model to investigate different flow regimes in CFBs. Sand and FCC particles are used to observe two different patterns. Dilute cluster formation pattern was obtained for sand and dense core-annulus flow regime was obtained for FCC particles. Time averaged volume fraction and solid/gas velocities at some sections of the riser were compared with some experimental studies available in the literature. Average volume fraction of 1% was obtained for sand case which reduces while moving upwards in the riser. Cluster formation was observable in that case since solid volume fraction was increased and solid velocity decreased. According to parametric studies, it was concluded that the results show fair dependence on superficial gas velocity, solid circulation rate, particle size and riser diameter.

Mathiesen et al. [29] investigated hydrodynamics of CFB experimentally and numerically. Sand particles having Sauter mean diameter of $120\mu\text{m}$ and $185\mu\text{m}$ were mixed in fluidized bed. Experimental measurements were conducted with Laser Doppler Anemometry (LDA) and Phase Doppler Anemometry (PDA) systems. 2D Cartesian two fluid model was developed for the whole circulating fluidized bed system; including the riser, the cyclone, and the recirculation pipe. Radial distribution of average particle diameter, solid volume fraction, solid velocity, particle turbulent velocity (RMS velocity or average of velocity fluctuation) profiles were obtained for different heights of the riser. Reasonable matches were observed between experimental and computational results. Core-annulus flow pattern was obtained in the riser. Relative velocity between small and big particles were decreased near the walls where overall particle agglomeration existed. It was also reported that smaller particles had greater turbulent velocities.

Zhang and Van der Heyden [30] performed high resolution 3D computational analysis of a square cross section CFB riser. Particles having average diameter of $120\mu\text{m}$ and density of 2400kg/m^3 were used. Simulation results were compared with an experimental study available in the literature. Effect of grid resolution was presented. Radial distribution of particle volume fraction, velocity and standard

deviation of velocities were printed for different riser sections. Basic features of the flow and the qualitative behavior of the flow could be captured well. However, even if a high resolution grid was used, mesoscale structures and cluster formation could not be observed well. Reason for this was explained by simplicity of the model which did not include constitutive models considering particle interactions. Investigation of mesoscale structures were done in the following study of Zhang and Van der Heyden [31] by deriving macroscopic averaged closure equations for added-mass and drag forces. Reduction coefficient for relative particle velocity which relates the drag force and the reduction coefficient for mesoscale added-mass coefficient was suggested.

Hartge et al. [32] simulated hydrodynamics of circulating fluidized bed with the two fluid model in a commercial software, Fluent. 3D analysis was performed for square cross section riser and compared with the experimental data available in literature. Different drag models were examined which are Syamlal, Gidaspow and EMMS drag models. Turbulence models of RNG $k - \epsilon$ and realizable $k - \epsilon$ were tested. Sand particles having mean particle size of $190 \mu m$ were used. Among different drag models, EMMS model could estimate averaged void fraction along riser closely due to consideration of subgrid heterogeneities in the flow. Generally, the simulation results were in reasonable agreement with the experimental results, but requirement of more detailed experimental data was reported.

Zhang et al. [33] investigated hydrodynamics of a 150MWe circulating fluidized bed boiler by using Eulerian-Eulerian CFD method. The whole boiler system including the riser, the feeding units and the cyclones were modeled in 3D. Sand particles having $200 \mu m$ diameter and 2000kg/m^3 density were used. For a specific operating condition, heterogeneity of flow was applied by recalculation of drag reduction parameters based on EMMS approach. Pressure drop along the riser was adjusted to compare with the experimental data available in literature. Excellent agreement was found in this comparison. Pressure drops in every component of the system were plotted and radial distribution of solid volume fractions were presented at different

sections of the riser. Increase in the particle concentration was reported in various sections of the riser. In addition, significant drop in the solid vertical velocity was obtained at regions closer to the boiler wall.

Nguyen et al. [34] examined cold and hot dual circulating fluidized bed both experimentally and numerically. Full loop of the system was considered including the riser, the cyclone, the downcomer pipe, the bubbling bed and the loop-seal. A 3D two fluid CFD model was constructed in Fluent. Various operating conditions depending on gas velocities were compared. 6 different cases for cold bed were compared in terms of solid circulation rates and solid holdup. Difficulty of obtaining steady operating conditions was mentioned by presenting solid holdup profiles especially at high solid circulation rates. Deviations in radial distribution of solid volume fraction and solid velocities for hot and cold cases were compared. Hydrodynamic similarity was shown between hot and cold cases. The discrepancies were attributed to limitations of the 2D model.

Baysal [35]-[36] studied on numerical investigation of circulating fluidized bed hydrodynamics. Particles having wide range of size and density were examined. Phoenix CFD code was used in the thesis. It is an important study since it gives lots of results from parametric studies. It is concluded that particle density, particle diameter and superficial gas velocity affects solid circulation rate a lot. Results were obtained for radial distribution of void fractions, radial distribution of solid and gas velocities at different heights and pressure and void fraction contour plots.

Li et al. [37] performed a grid independence study for Eulerian CFD modeling of CFBs. Only the riser section with inlet and outlet sections was modeled in 2D in an open-source software, MFIX. Two different systems were considered, one is a square riser loaded with sand particles having $213\mu\text{m}$ diameter and 2640kg/m^3 density and the other is a relatively longer circular riser loaded with dense polyethylene beads with diameter of $802\mu\text{m}$ and density of 863 kg/m^3 . For the first system, simulation results were compared with the experimental data in literature while for the second system an experimental set-up was available in their laboratory. Specularity

coefficient was selected as 0.005 and particle-wall restitution coefficient was selected as 0.8. Hundreds of simulations were performed and time-averaged data was taken. Typically, increase in solid concentration and decrease in solid velocity was observed near the wall. Grid dependence was examined for these parameters. It was concluded that for the first case with sand particles, 2D grid could converge better than for the second case. Good predictions were obtained for even coarser grid size of ten times the particle diameter, which is usually a suggested size as a rule of thumb. Better grid convergence was obtained from the 3D model than the 2D model.

As a follow up study for the previous one, Li et al. [38] studied the differences of 2D and 3D models for the CFB riser. Both sand and polyethylene particles were used again with the same riser geometries. Pressure drops, radial distribution of solid concentration and vertical solid velocities were compared. Generally, significant differences were observed between the 2D and 3D cases. The 2D simulations were not able to catch the effect of cross-section shape. It was reported that the 2D models can give good results if filtered subgrid models are used. Discrepancies were more abrupt for Geldart A particle case (polyethylene case). It was concluded that 2D models can be used for predicting qualitative behavior of such systems. Accurate quantitative predictions can be made using 3D models only.

The studies in the literature related to CFD simulations of Geldart B type particles in CFBs explained in this section is summarized in Table 2.

According to the literature review, following deductions can be made about CFD analysis of fluidized bed systems:

- Eulerian-Eulerian methods (two fluid methods) have been commonly used for large systems due to lower computational cost compared to Lagrangian methods.
- Eulerian methods contain complex models. Frictional and collisional behavior of particles should be modeled properly. Interphase drag force is

dominant, so that accurate prediction of drag force is necessary to estimate hydrodynamic behavior of these systems.

- It is hard to obtain clear grid independence for all parameters due to transient and fluctuating behavior of these systems and model complexity.
- Proper adjustments of model parameters are required for different Geldart classifications of particles. (e.g on drag models, particle-wall interaction models).
- Even well-built 2D models cannot make very accurate predictions about the hydrodynamics of the system quantitatively. Nonetheless, 2D models can give good qualitative predictions. On the other hand, 3D models require very large amount of computational power. Especially for large systems like CFBs, the code must allow parallelization up to 100 cores.
- Due to inaccuracies in drag prediction, solid mass fluxes cannot not be estimated accurately. Moreover, it is hard to reach pure steady state operating conditions in time ranges viable to simulate due to high computational cost.
- Turbulence models should be considered for large particle and high speed operating conditions. Because the gas velocity should be higher than at least terminal velocity of the particles, a gas turbulence model and a solid phase stress model based including turbulence should be considered for circulating fluidized bed riser models. This might not be necessary for fine and light Geldart-A powders, since they can fluidize in low velocities and dense forms.

Table 2 Summary of CFD studies of circulating fluidized beds loaded with Geldart B type particles

Reference	Riser Geometry	Particle properties	Model geometry	Code/Software
Tsuo and Gidaspow [28]	76.2 mm ID cross section 5.5m height	$d_p = 520\mu m$ $\rho_s = 2620kg/m^3$	2D	Extended k-FIX
Mathiesen et al. [29]	32 mm ID cross section 1m height	$d_p = 120 \& 185\mu m$ $\rho_s = 2400kg/m^3$	3D	Tel-Tek code
Zhang and VanderHeyden [30]-[31]	20x20cm ² cross section 2m height	$d_p = 120\mu m$ $\rho_s = 2400kg/m^3$	3D	CFDLIB
Hartge et al. [32]	1x0.3m ² cross section 8.5m height	$d_p = 190\mu m$ $\rho_s = 2600kg/m^3$	3D	Fluent
Zhang et al. [33]	15.32x7.22m ² cross section 36.5m height	$d_p = 200\mu m$ $\rho_s = 2000kg/m^3$	3D	Fluent
Nguyen et al. [34]	40x110mm ² cross section 4.5m height	$d_p = 250\mu m$ $\rho_s = 2466kg/m^3$	2D	Fluent
Li et al. [37]-[38]	146x146mm ² cross section 9.14m height	$d_p = 213\mu m$ $\rho_s = 2640kg/m^3$	Both 2D & 3D	MFIX

1.4. Thesis Overview

1.4.1. Objective

In this thesis, CFB riser solar receiver concept is examined using a riser model similar to the design of Flamant [6]. Modeling hydrodynamics of the system is the main goal which will be the basis for the subsequent heat transfer investigations. In order to achieve that goal, literature is reviewed and important parameters about modeling of these systems are examined. For bubbling bed and circulating fluidized bed riser systems, model optimizations have been made by experimental validation studies. Outcomes of the CFB solar riser analyses are discussed.

Objectives of this thesis are listed below:

- Examination of the details in numerical modeling of fluidized beds using computational fluid dynamics methods
- Development of a reliable fluidized bed model and validation of it with an experimental study
- Investigation of hydrodynamics of a CFB riser receiver by applying the validated model to the design
- Evaluation and discussion of operating parameters of the riser such as pressure drop, voidage profiles and gas/solid velocities.

1.4.2. Organization

Motivation of the thesis supported by a structured literature review giving a background of solar thermal power systems and covering current state of the art for hydrodynamical investigations of CFB risers is provided and the objectives of the thesis are explained with a list of tasks in Chapter 1.

Fundamentals of hydrodynamics in fluidized beds are given in Chapter 2 to provide a theoretical base to understand the fluidized bed systems.

Theory of two fluid computational fluid dynamics method for modeling fluidized bed systems is provided in Chapter 3.

Most of the work performed for accomplishment of the tasks of the thesis are provided in Chapter 4. Examination of two fluid model parameters are done by using a bubbling fluidized bed model for which experimental data is available. Using the insight gained from the preliminary bubbling fluidized bed study, the final riser model is developed and wall boundary conditions are adjusted according to an experimental study. After this experimental validation, CFB riser receiver design and model is provided and model parameters are given at the end of Chapter 4.

Results after evaluation of the riser model are provided and discussions about hydrodynamics parameters are done in Chapter 5.

Outcomes of the thesis and important results are summarized in Chapter 6 and some suggestions are provided to extend this work in future studies.

CHAPTER 2

FUNDAMENTALS OF HYDRODYNAMICS IN FLUIDIZED BEDS

2.1. Introduction

Fluidization is an operation of attracting solid particles by flow of another fluid to carry stationary solid particles to a fluid like state or in other words, to fluidize. This operation has several advantages especially in combustion processes. Fluidization technology is used in various areas like coal combustion, gasification, fluid catalytic cracking, chemical processing, coating, granulation and drying. For instance, combustion of coal or biomass in fluidized beds are widely investigated to obtain efficient burning and capture harmful product gases. Hydrodynamics and heat transfer of these systems are extensively studied experimentally. Theoretical and computational investigations of these systems are also interesting research areas in which various significant developments have been made up to now.

In the literature, different reactor designs exist such as fluidized beds, spouted beds and circulating fluidized beds. The design to be modeled in this thesis is similar to CFB in which particles are circulating in the reactor. CFBs consist of a bed, a riser, a cyclone and a return seal. Particles are fluidized in the bed and transported upwards through the riser section. Gas is usually separated from the particles in the cyclone section and the particles return back to the riser through the return seal and complete the circulation cycle. A typical schematic of a CFB is given in Figure 6. [39]

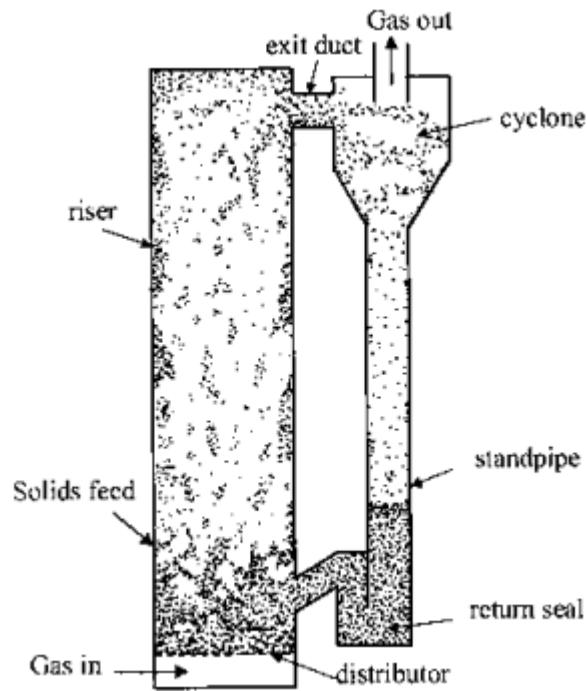


Figure 6 Schematic of a typical circulating fluidized bed (Adapted from [39])

Hydrodynamics and heat transfer of fluidized beds are studied extensively for various fluidized bed designs. Despite the differences among various designs, fundamentals of fluidization that will be discussed in this section are similar for all of the designs.

2.2. Hydrodynamics

Hydrodynamics of fluidization is classified mainly by flow regimes. Different flow regimes are determined by the particle type and the flow parameters affecting hydrodynamics of the fluidized bed. These parameters and mapping of fluidized bed regimes will be explained in the following sections

2.2.1. Fluidization Parameters

First of all, characterization of particles is very important for the investigation of fluidization. Particle size (particle diameter) can be determined for fully spherical

particles easily, but particle size determination can be confusing for non-spherical particles. Sphericity Φ_s is defined for measuring how close is the particle shape to a sphere, which is fraction of the surface area of a spherical particle of the same particle volume to the actual particle surface area. Φ_s is defined in the range of 0-1 and $\Phi_s = 1$ for perfect spheres. Sphericity of sand-like particles usually varies in the range of 0.5-0.9. Some correlations for the sphericity of different particles are available in the literature. Sphericity is conceptually given as [40]

$$\phi_s = \left(\frac{\text{surface of sphere}}{\text{surface of particle}} \right)_{\text{of same volume}} \quad (1)$$

Void fraction (ϵ_f) is the volume fraction of the gas phase in any cross section at a given time. Usually void fraction profiles are used to distinguish the bubble formation and determine the flow regimes. Packed bed or fixed bed is the condition of a bed when the particles are staying stationary. Void fraction in a packed bed depends on the particle sphericity. Packed bed voidage ϵ_m is given in a chart in the textbook of Levenspiel [40] which is presented in Figure 7.

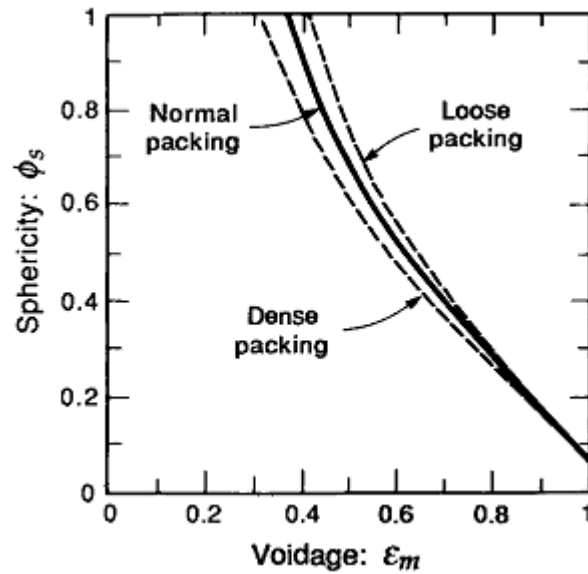


Figure 7 Voidage of randomly packed uniformly sized particles having various sphericities (Adapted from [40])

Superficial gas velocity (U_g) is velocity of air that is supplied to the bed to fluidize the solid particles which is one of the main parameters affecting the flow regimes. This value should reach to a certain level to obtain fluidization, which is called minimum fluidization velocity (U_{mf}). Minimum fluidization condition is achieved when drag force of upward flowing gas on particles can just compensate the weight of particles. Drag force is usually determined by empirical correlations which are developed from pressure drop measurements. In other words, when the gas velocity is started to be increased from a very small value, U_{mf} is the gas velocity when the fixed bed is started to fluidize. Pressure drop is increased up to reaching U_{mf} and it becomes constant when the bed is fluidized. After reaching terminal velocity, pressure drop starts decreasing. This situation can be shown in Figure 8.

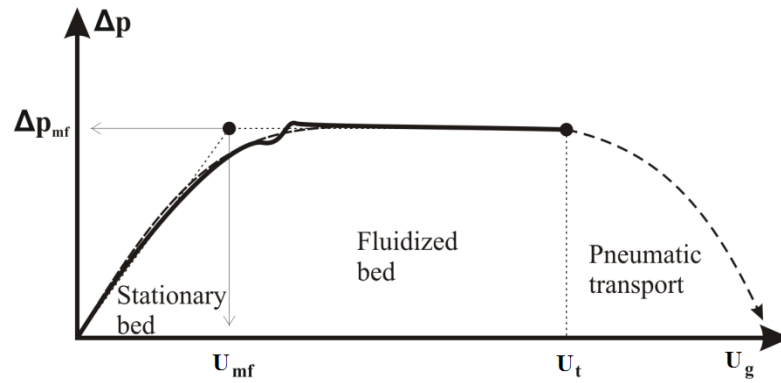


Figure 8 Pressure drop with respect to superficial gas velocity (Adapted from [40])

There are various correlations to calculate minimum fluidization velocity. Minimum fluidization velocity can be written in terms of minimum fluidization Reynolds number as [40]

$$U_{mf} = \frac{\mu Re_{mf}}{d_p \rho_g} \quad (2)$$

Here Re_{mf} is the minimum fluidization Reynolds number to be determined. Normally, it depends on Archimedes number, the sphericity and the minimum fluidization voidage. However, when experimental data is not available for the sphericity and the minimum fluidization voidage, it is still possible to estimate Re_{mf} with a correlation defined by Wen-Yu, which is given as.[40]

$$Re_{mf} = \sqrt{(33.7^2 + 0.0408Ar)} - 33.7 \quad (3)$$

where Ar is Archimedes number that is defined as [40]

$$Ar = \frac{d_p^3 \rho_g (\rho_s - \rho_g) g}{\mu^2} \quad (4)$$

Terminal velocity of the particles, u_t is an important parameter especially for circulating fluidized beds. Terminal velocity of particles is the limiting velocity of particles in free fall. Considering the primary forces on particles, which are gravity force and drag force, terminal velocity is the velocity of the particle when these two

forces are equal. A schematic representation of this phenomenon is shown in Figure 9.

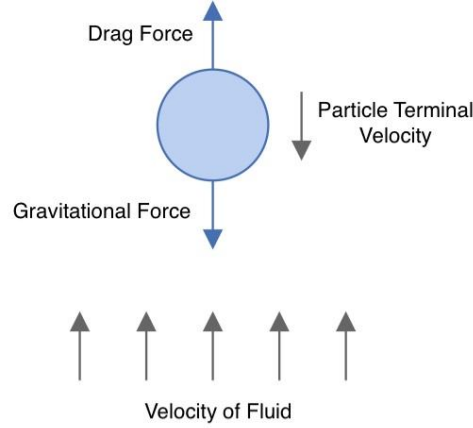


Figure 9 Schematic representation of equilibrium of primary forces on a single particle when the particle has terminal velocity (Adapted from [41])

Gas velocity must be greater than this parameter to carry and move particles upwards through the circulating fluidized riser. u_t is defined as

$$u_t = \left(\frac{4d_p(\rho_s - \rho_g)g}{3\rho_g C_D} \right)^{1/2} \quad (5)$$

C_D is the drag coefficient to be determined experimentally. Some empirical correlations are available in literature. Dimensionless diameter (d_p^*) and dimensionless velocity (u^*) are derived from graphical representation of these correlations in order to approximate u_t directly. Dimensionless parameters are defined as [40]

$$d_p^* = d_p \left(\frac{\rho_g(\rho_s - \rho_g)g}{\mu_g^2} \right)^{1/3} \quad (6)$$

$$u^* = u \left(\frac{\rho_g^2}{\mu_g(\rho_s - \rho_g)g} \right)^{1/3} \quad (7)$$

Based on these dimensionless definitions, dimensionless terminal velocity is defined as [40]

$$u_t^* = \left(\frac{18}{d_p^{*2}} + \frac{2.335 - 1.744\Phi_s}{d_p^{*0.5}} \right)^{-1}, \quad 0.5 < \Phi_s < 1 \quad (8)$$

After dimensionless terminal velocity is calculated, u_t is obtained from Equation (7).

Solids circulation rate (G_s) is an important parameter for circulating fluidized beds which is the amount of solid particles circulating at a given time inside the circulating fluidized bed loop.

2.2.2. Classification of Particles

Geldart [26] classified the particles according to their fluidization characteristics. Geldart classification of particles which is given below is useful and is commonly used for describing fluidized particles.

Particles in Geldart group A have small particle size and/or low particle density ($< \sim 1.4 \text{ g/cm}^3$). They are aeratable and easy to fluidize. FCC catalyst and silicon carbide are examples for this group. Agglomeration might exist during fluidization.

Most particles in Geldart group B are in size range of 40-500 μm and in a density range of 1.4-4 g/cm^3 . They fluidize well and large bubbles occur in the bubbling regime. Usually the minimum fluidization velocity and the minimum bubbling velocity are close to each other. Fluidization behaviors and computational analyses of this kind of particles are extensively studied. Sand-like particles, glass beads and some biomass particles can be exemplified in this group.

Geldart group C particles have very small sizes. They are as small as very fine powders. Cohesive behavior causes difficulty in fluidization. Face powder, flour, and starch are examples of group C.

Geldart group D particles have very large size and/or high density. They are spoutable. Fluidization is difficult if the bed is deep. Drying grains and peas, roasting coffee beans, gasifying coals are classified in Group D.

Geldart [26] prepared a powder classification diagram where the particles are classified in terms of mean particle diameter (\bar{d}_p) and relative density of solid with respect to air density ($\rho_s - \rho_g$). Levenspiel [40] prepared a simplified form of his diagram which is given in Figure 10

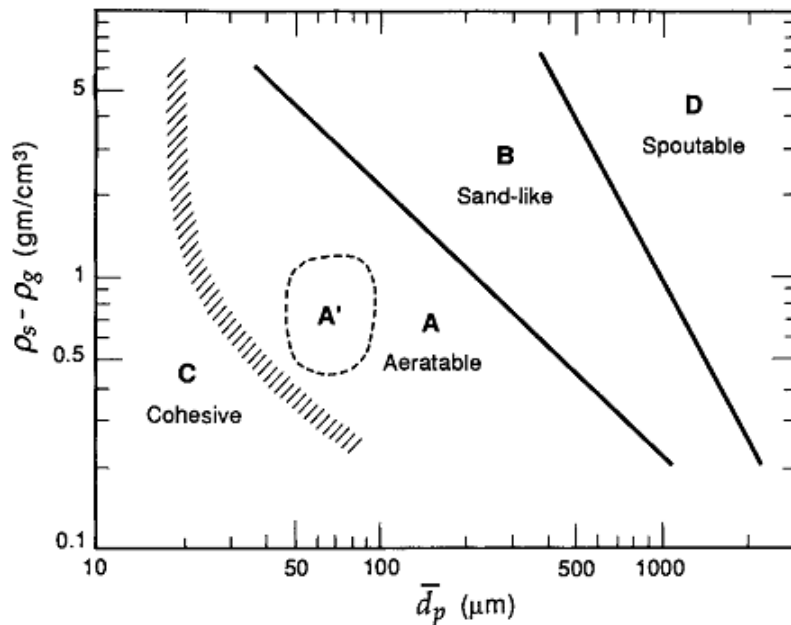


Figure 10 Geldart powder classification diagram for fluidization by air at ambient conditions (Adapted from [40])

2.2.3. Mapping of Fluidization Regimes

Different fluidization regimes are classified and briefly explained in this section, starting from dense flows continuing to dilute flows.

Fixed bed regime is the regime when particles are stationary. Superficial gas velocity is below the minimum fluidization velocity. Particles are quiescent and no visible fluidization occurs.

In particulate regime (smooth regime), superficial gas velocity is between the minimum fluidization and the minimum bubbling velocities. Bed expands smoothly and small-scale homogeneous particle motions are seen.

Bubbling regime presents bubble formation. Superficial gas velocity is above the minimum bubbling velocity. Gas bubbles make mixing of solids during their rise to the surface.

In the turbulent-churning regime, superficial gas velocity is higher than it is in the bubbling regime. Bubbles and slugs in narrow columns no longer appear. Bed voidage is large and particle clusters are formed.

Fast fluidization regime is where solid fractions are much lower than for bubbling or turbulent beds (30-60%), but much higher than that for pneumatic transport. Clusters and strands of particles that break apart and reform quickly. Back mixing of solids exists. Suspension is denser at the bottom and dilute at the top, there is no bed surface.

Pneumatic conveying regime can be considered as a limit of dilute fluidization. Superficial gas velocity is very high and the solid volume fractions are very low ($< \sim 0.01$). All particles are moving separately and everywhere the suspension is dilute. Concentration is varying along the riser, there is no bed surface. [40]

Knuii and Levenspiel [40] represented a general flow regime diagram for different Geldart particle types which is given for particle mean size and superficial gas velocity in Figure 11.

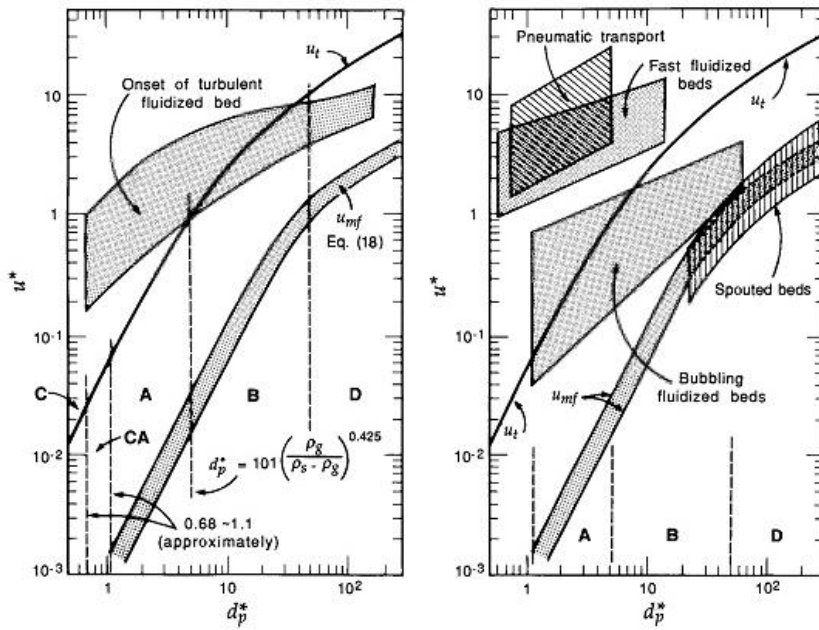


Figure 11 Generalized map of fluidization regimes (Adapted from [40])

Flow regimes are summarized briefly in a table represented by Knuii and Levenspiel [40] in Figure 12. C,A,B and D are representing the Geldart particle types. Particle size increases moving to the right and superficial gas velocity increases moving upwards.

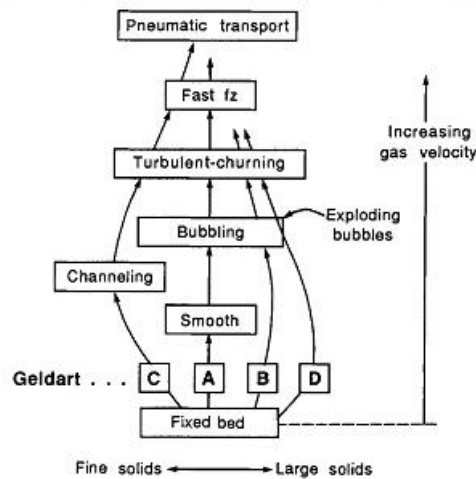


Figure 12 Progressive change in fluidization regime with change in gas velocity
(Adapted from [40])

Schematic representation of fluidization regimes are presented in Figure 13. Dark areas represent solid particles. As the gas velocity increases, bed becomes more dilute starting from particulate regime to pneumatic conveying regime. Usually flow regime in circulating fluidized bed riser is fast fluidization or dilute pneumatic conveying.

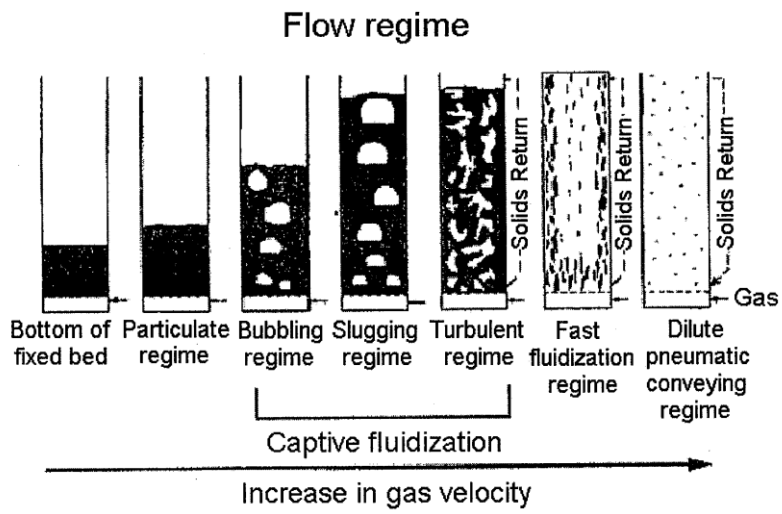


Figure 13 Schematic representation of different fluidization regimes (Adapted from [42])

CHAPTER 3

COMPUTATIONAL FLUID DYNAMICS METHOD FOR NUMERICAL INVESTIGATION OF FLUIDIZED BEDS

3.1. Introduction

Computational Fluid Dynamics methods are used for numerical investigation of gas-solid suspension flows and fluidized beds quite frequently. Gas phase is usually considered in Eulerian approach. For the solid phase either Eulerian or Lagrangian approaches are used. As it is well known, Lagrangian specification of the flow field is based on following an individual fluid parcel when it moves through space and time. In Eulerian specification, one focuses on specific locations in space where the fluid flows as time passes. Various methods used for computational modeling of gas-solid multiphase flows are shown in Figure 14

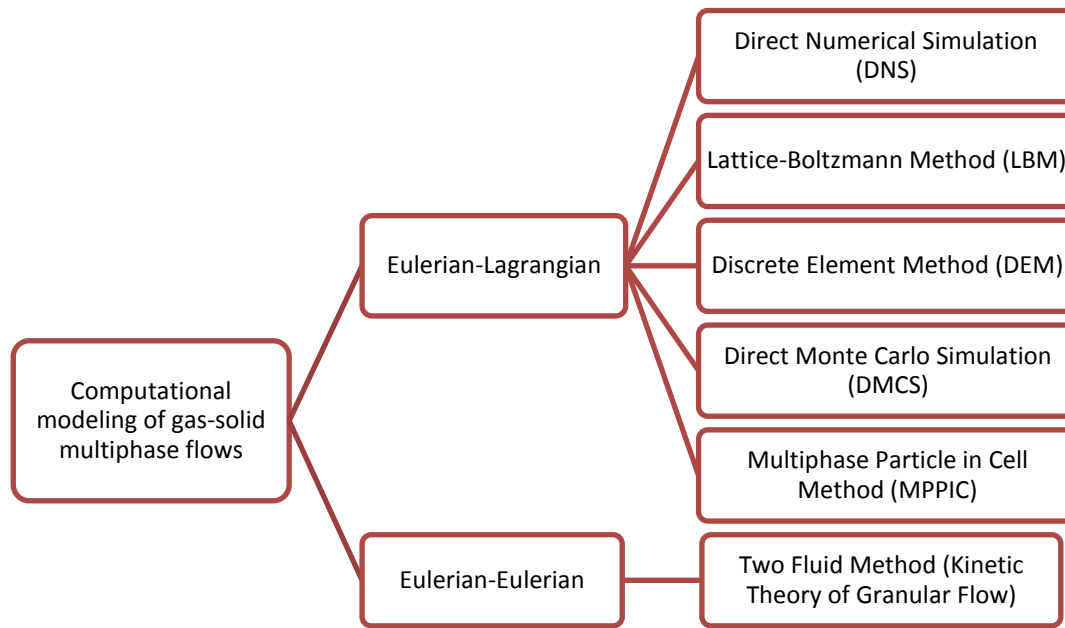


Figure 14 Various approaches for computational modeling of gas-solid flows

In Lagrangian models, which are also called discrete particle models, solid particles are tracked individually in the domain and the solution is coupled with the Eulerian solution of the gas phase. These models calculate the motion and the path of particles and particle interactions are defined by soft-particle dynamics or particle dynamics [43]. Physical resolution of the flow reduces the necessity for complex constitutive relations. By particle tracking, realistic models can be constructed, but it requires large computational power and memory which makes using these models unfeasible for industrial scale fluidized bed models. [43]–[45]

Direct Numerical Simulation (DNS) method is one of the Lagrangian approaches to the flow solution. DNS fully resolves Navier-Stokes equations of the flow around the particles and tracks the particle motion by solving Newton's equation of motion. Although the model does not contain complex constitutive relations, it is computationally the most expensive method among others [44]. Lattice-Boltzmann Method (LBM) differs itself from DNS by solving the flow around the particles with Lattice-Boltzmann equations. LBM is a computationally less expensive method

compared to DNS, but computational cost can be reduced by not resolving the flow field around the particles as in Discrete Element Method (DEM). Interphase forces like gas-solid drag should be modeled by constitutive relations which link solutions of the gas and the solid phases. Although it is possible to track a few millions of particles with current computer capabilities by this method, it is still hard to simulate big scale reactors which contain more than billion particles. [44] Most of the computational load of DEM comes from determination of particle contact and integration through the contacts. This load challenge is tried to be reduced by different methods. One of them is Direct Simulation Monte Carlo method, (DSMC) which detects particle contacts with a probabilistic approach. Other relatively new method is Multiphase Particle in cell method (MPPIC), which obtains collisional stresses from an Eulerian grid. Unexpectedly, third option is avoiding individual particle tracking and treating the solid phase as a fluid phase which is called Eulerian-Eulerian approach, continuum gas-solid model or Two-Fluid Model.

Eulerian models treat both solid and gas phases as a continuum and averaging solid motion out of the particle size which leads to an interpenetrating continuum model. In this model, solid phase co-locates the fluid phase so that both phases are sharing the same grid. This reduces computational expenses significantly, but model becomes more complicated since complex constitutive relations are required for adapting solid flow characteristics [40]-[41]. Since this thesis deals with an industrial scale circulating fluidized bed riser, most appropriate method is selected as Two-Fluid Model. Therefore, fundamental and constitutive equations of this method will be given in the upcoming sub-sections.

3.2. Fundamental Equations of Two-Fluid Method

First of all, basic transport equations of two-fluid method will be given. Conservation of mass, momentum and energy equations are derived for both gas and solid phases. Point variables are averaged over a region greater than the particle spacing. Determination of rate of averaging volume occupied by different phases are defined

by phasic volume fractions which are assumed to be continuous functions of space and time. Summation of volume fraction of all of the phases is equal to one. [46] The formulation is given with

$$\epsilon_g + \sum_{m=1}^{N_m} \epsilon_m = 1 \quad (9)$$

where ϵ_g and ϵ_m are volume fractions of gas and m^{th} solid phases. Please note that subscript g will be used for gas and s will be used for solid for parameters used in equations.

Continuity equation for the gas and solid phases are given in Equations (10) and (11).

$$\frac{\partial(\epsilon_g \rho_g)}{\partial t} + \frac{\partial}{\partial x_i} \cdot (\epsilon_g \rho_g U_{gi}) = \sum_{n=1}^{N_m} R_{gn} \quad (10)$$

$$\frac{\partial(\epsilon_m \rho_m)}{\partial t} + \frac{\partial}{\partial x_i} \cdot (\epsilon_m \rho_m U_{mi}) = \sum_{n=1}^{N_m} R_{mn} \quad (11)$$

where the right hand sides of the Equations (10) and (11) are mass transfer terms. Momentum equations for gas and solid phases are given in Equations (12) and (13) respectively.

$$\frac{\partial(\epsilon_g \rho_g U_g)}{\partial t} + \frac{\partial}{\partial x_j} \cdot (\epsilon_g \rho_g U_g U_{gj}) = -\epsilon_g \frac{\partial P_g}{\partial x_i} + \frac{\partial \tau_{gij}}{\partial x_j} - \sum_{m=1}^M I_{gmi} + f_{gi} + \epsilon_g \rho_g g_i \quad (12)$$

$$\frac{\partial(\epsilon_m \rho_m U_m)}{\partial t} + \frac{\partial}{\partial x_j} \cdot (\epsilon_m \rho_m U_m U_{mj}) = -\epsilon_m \frac{\partial P_g}{\partial x_i} + \frac{\partial \tau_{mij}}{\partial x_j} + I_{gmi} - \sum_{m=1}^M I_{kmi} + \epsilon_m \rho_m g_i \quad (13)$$

Both Equations (12) and (13) contain similar terms, the difference occur only in subscripts where g is for gas and m is for m^{th} solid phase. First term on the left hand side represents rate of momentum increase and the second term represents momentum transfer by convection. The first term on the right hand side represents

momentum change due to gas pressure gradient. The second term represents gas and solid phase stress tensors. I_{gm} is momentum transfer between gas and solid phases and I_{km} is for momentum transfer between different solid phases. f_g is general body force excluding the force due to gravity where it is defined in the last term. These fundamental equations are solved with constitutive equations defining the gas and solid phase stress tensors, interphase momentum exchanges and additional body forces [44].

3.3. Gas-Solids Momentum Transfer

There are several interaction forces between gas and solid phases like drag force, buoyancy, virtual mass effect, Saffman lift force, Magnus force, Basset force and Faxen force. Buoyancy force is caused by gas pressure gradient and represented in the first term on the right hand side of Equations (12) and (13). Since the most dominant and significant force is drag force which is caused by velocity differences between phases, I_{gm} term in Equations (12) and (13) will include drag force only [44]. Solid volume fraction will be linearly affecting drag formulation. Interphase momentum exchange term I_{gm} is defined as [47]

$$I_{gm} = \beta_{gm} |U_g - U_m| \quad (14)$$

Drag coefficient, β_{gm} is usually obtained from experimental pressure drop correlations. Ergun equation is commonly used for pressure drop calculations especially for dense beds or fixed beds. Wen and Yu [48] performed experiments for pressure drop calculations for wide range of solid volume fractions. Gidaspow [49] combined Wen&Yu correlation with Ergun equation [50] at high solid volume fractions and obtained Gidaspow drag model. [43] Drag coefficient of Gidaspow drag model is given with [43][47]

$$\beta_{gs} = \begin{cases} \frac{3}{4} C_D \frac{\rho_g \epsilon_g \epsilon_s |U_g - U_s|}{d_p} \epsilon_g^{-2.65}, & \epsilon_g \geq 0.8 \\ \frac{150 \epsilon_s (1 - \epsilon_g) \mu_g}{\epsilon_g d_{ps}^2} + \frac{1.75 \rho_g \epsilon_s |U_g - U_s|}{d_{ps}}, & \epsilon_g < 0.8 \end{cases} \quad (15)$$

C_D is defined by Rowe [51] and given with

$$C_D = \begin{cases} \frac{24}{Re_p} [1 + 0.15 Re_p^{0.687}], & Re_p < 1000 \\ 0.44, & Re_p \geq 1000 \end{cases} \quad (16)$$

where particle Reynolds number is defined as

$$Re_p = \frac{\rho_g \epsilon_g |U_g - U_s| d_p}{\mu_g} \quad (17)$$

Syamlal et al. proposed that drag coefficient can be obtained from terminal velocity of the particles. Syamlal drag model is given with [44][47]

$$\beta_{gs} = \frac{3}{4} C_D \frac{\epsilon_s \epsilon_g \rho_g}{V_{rm}^2 d_p} |U_g - U_s| \quad (18)$$

In Syamlal drag model, C_D is a function of terminal velocity, V_{rm} as well which is defined by Dalla Valle [52] with

$$C_D = \left(0.63 + 4.8 \sqrt{\frac{V_{rm}}{Re_p}} \right)^2 \quad (19)$$

Terminal velocity of particles are determined by empirical correlations of Garside and Al-Bibouni [53]. Terminal velocities are defined in Equations (20), (21) and (22) [40][43]. However Syamlal made some modifications on these empirical correlations to obtain a better match with the experimental results. Modification is done by the definition of parameters c_1 and d_1 in Equation (22) which are adjusted by using experimental minimum fluidization velocity [44].

$$V_{rm} = 0.5 \left(A - 0.06 Re_p + \sqrt{(0.06 Re_p)^2 + 0.12 Re_p (2B - A) + A^2} \right) \quad (20)$$

$$A = \epsilon_g^{4.14} \quad (21)$$

$$B = \begin{cases} c_1 \epsilon_g^{1.28}, & \epsilon_g \leq 0.85 \\ \epsilon_g^{d_1}, & \epsilon_g > 0.85 \end{cases} \quad (22)$$

There are many studies about proper determination of gas-solid drag coefficient for variety of cases and particle types. Since Syamlal and Gidaspow drag models are used in this thesis, details of these models have been given.

For all of the drag models discussed here, particles are assumed as fully spherical and they have a uniform particle size. Effect of particle shape on drag coefficient is widely examined in literature. These drag models can give proper results for Geldart B type particles, but modifications are needed for Geldart A type particles. Since Geldart A type particles are very fine and adhesive, agglomeration exists and classical drag models overestimate drag force and bed expansion. Another problem about drag estimation is lack of grid resolution to catch particle clusters. It is suggested to have a maximum grid size of ten particle diameters, but even that might not be possible for commercial-scale reactors. Therefore, subgrid models like filtered continuum models or energy minimization multiscale models (EMMS) are developed to be able to reach highly resolved solutions using coarse grids [44].

3.4. Fluid Phase Stress Tensor

Stress tensor for the gas or fluid phase is given with [44]

$$\overline{\overline{S}}_g = -P_g \overline{\overline{I}} + \overline{\overline{\tau}}_g \quad (23)$$

where P_g is gas pressure and $\overline{\overline{I}}$ is identity tensor. $\overline{\overline{\tau}}_g$ is viscous stress tensor and it is assumed to be of the Newtonian form as

$$\overline{\overline{\tau}}_g = 2\epsilon_g \mu_g \overline{\overline{D}}_g + \epsilon_g \lambda_g \text{tr}(\overline{\overline{D}}_g) \overline{\overline{I}} \quad (24)$$

where $\overline{\overline{D}}_g$ is the fluid phase strain rate tensor and tr is trace function. $\overline{\overline{D}}_g$ is defined with

$$\overline{\overline{D}}_g = \frac{1}{2} [\nabla \overline{\mathbf{v}}_g + (\nabla \overline{\mathbf{v}}_g)^T] \quad (25)$$

3.5. Solid Phase Stress Tensor

Developing closure equations for particle-particle interactions over dilute and dense regimes is a difficult task and wide research area due to different types of particle-particle force transmission. [44] This part is mainly responsible for fluid like modeling of granular phase. Similar to fluid phase, Newtonian description of solid phase stress tensor can be written as

$$\overline{\overline{S}}_s = -P_s \overline{\overline{I}} + \overline{\overline{\tau}}_s \quad (26)$$

Determination of solid phase stress $\overline{\overline{\tau}}_s$ and solid pressure P_s is a difficult task. Depending on different mechanisms, various models exist. Solid phase can be considered in two regimes depending on the volume fraction. In dense regime (plastic regime), frictional forces between particles are dominant and in dilute regime (viscous regime) collisional forces are significant. These two regimes are distinguished by a critical void fraction, called ϵ_g^* . Usually, critical void fraction is set to minimum fluidization void fraction for fluidized bed simulations. [46] Plastic and viscous regimes are presented in Figure 15 [44].

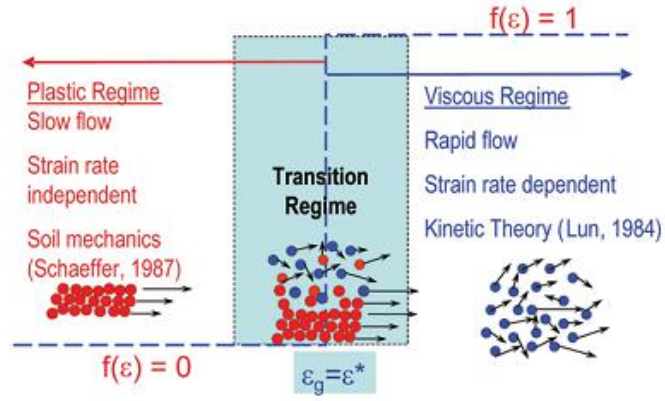


Figure 15 Schematic of plastic and viscous regimes of granular phase as a function of void fraction (Adapted from [44])

Plastic regime includes long-lasting particle contacts which cause slow flow of quasi-static particle assemblies which is modeled by soil mechanics. In viscous regime, particles are quickly moving and random particle collisions are frequent. Constitutive equations are derived from the kinetic theory. Transition regime is handled by blending functions which provide a balance between two approaches [44].

3.5.1. Plastic Regime (Dense Regime)

Schaeffer's frictional theory [54] is used in plastic regime. Please note that this model is used for void fractions under critical void fraction. Solid pressure is defined as [46]

$$P_s = 10^{25} (\epsilon_g^* - \epsilon_g)^{10}, \quad \epsilon_g < \epsilon_g^* \quad (27)$$

Solid phase stress is defined as

$$\bar{\tau}_s = 2\mu_s \bar{D}_s, \quad \epsilon_g < \epsilon_g^* \quad (28)$$

Expression for shear viscosity is given as

$$\mu_s = \min \left(\frac{P_s \sin(\phi_f)}{\sqrt{4I_{2D}}}, \mu_{f,max} \right), \quad \epsilon_g < \epsilon_g^* \quad (29)$$

where ϕ_f is angle of internal friction and $\mu_{f,\max}$ is maximum granular viscosity which is an arbitrary large value to avoid divergence. I_{2D} is defined with

$$I_{2D} = \frac{1}{6} [(D_{s11} - D_{s22})^2 + (D_{s22} - D_{s33})^2 + (D_{s33} - D_{s11})^2] + D_{s12}^2 + D_{s23}^2 + D_{s31}^2 \quad (30)$$

Rate of strain tensor is defined as

$$D_{sij} = \frac{1}{2} \left(\frac{\partial u_{si}}{\partial x_j} + \frac{\partial u_{sj}}{\partial x_i} \right) \quad (31)$$

3.5.2. Viscous Regime (Dilute Regime)

Solid phase stresses in dilute regime are usually derived from the kinetic theory of granular gases. Particle collisional interactions are dominant in this regime and effective solid phase stresses are defined from particle streaming and direct collisions. [43] A parameter called granular temperature, Θ is defined to describe velocity fluctuations. Granular temperature is not a particle temperature, it is a measure of kinetic energy of molecular vibrations of particles. Relationship of granular temperature with kinetic energy fluctuation can be given with [43]

$$\Theta = \frac{1}{3} \langle v_s'^2 \rangle \quad (32)$$

Kinetic energy fluctuations are also called granular energy, which is defined as $\left(\frac{3}{2}\Theta\right)$. Balance of granular energy is required to supply continuity and momentum equations for both phases. The granular energy balance is given with [44][47]

$$\frac{3}{2} \rho_m \left[\frac{\partial \epsilon_m \Theta_m}{\partial t} + \frac{\partial \epsilon_m U_{mj} \Theta_m}{\partial x_j} \right] = \frac{\partial}{\partial x_i} \left(\kappa_m \frac{\partial \Theta_m}{\partial x_i} \right) + \tau_{mij} \frac{\partial U_{mi}}{\partial x_j} + \prod_m -\epsilon_m \rho_m J_m \quad (33)$$

First term on the right-hand side represents granular temperature diffusion, second term is production, third term stands for viscous dissipation and gas-particle slip effect, and the last term is for collisional dissipation. Details of viscous and collisional dissipation terms can be found in literature.[40][43]

Definition of solid phase stress is given as [47]

$$\tau_{mij} = \left(-P_m + \eta\mu_b \frac{\partial U_{mi}}{\partial x_i} \right) \delta_{ij} + 2\mu_m S_{mij} \quad (34)$$

where S_{mij} is given as

$$S_{mij} = \frac{1}{2} \left(\frac{\partial U_{mi}}{\partial x_j} + \frac{\partial U_{mj}}{\partial x_i} \right) - \frac{1}{3} \frac{\partial U_{mi}}{\partial x_i} \quad (35)$$

and P_m is solid pressure derived from the kinetic theory which is given by

$$P_m = \epsilon_s \rho_s \Theta_s (1 + 4\eta \epsilon_s g_0) \quad (36)$$

The first term in Equation (36) represents kinetic contribution and the second term represents collisional contribution. η is a function of particle-particle restitution coefficient which is a parameter to measure for characterizing particle collision. g_0 is radial distribution function. Descriptions of these parameters based on the kinetic theory can be found in [43]-[44][46]-[47]. μ_m is solid viscosity and μ_b is bulk viscosity which are function of void fraction, granular temperature, restitution coefficient and radial distribution function. Definitions of them are given with [47].

$$\mu_m = \left(\frac{2 + \alpha}{3} \right) \left[\frac{\mu_m^*}{g_0 \eta (2 - \eta)} \left(1 + \frac{8}{5} \eta \epsilon_s g_0 \right) \left(1 + \frac{8}{5} \eta (3\eta - 2) (\epsilon_s g_0) \right) + \frac{3}{5} \eta \mu_b \right] \quad (37)$$

$$\mu_m^* = \frac{\rho_s \epsilon_s g_0 \Theta_s \mu}{\rho_s \epsilon_s g_0 \Theta_s + \frac{2\beta\mu}{\rho_s \epsilon_s}} \quad (38)$$

$$\mu = \frac{5}{96} \rho_s d_p \sqrt{\pi \Theta_s} \quad (39)$$

$$\mu_b = \frac{256}{5\pi} \mu \epsilon_s^2 g_0 \quad (40)$$

κ_m in Equation (33) is solid conductivity derived from kinetic theory and given with [44][47].

$$\kappa_m = \left(\frac{\kappa_m^*}{g_0}\right) \left[\left(1 + \frac{12}{5} \eta \epsilon_s g_0\right) \left(1 + \frac{12}{5} \eta^2 (4\eta - 3) (\epsilon_s g_0)\right) + \frac{64}{25\pi} (41 - 33\eta) \eta^2 (\epsilon_s g_0)^2 \right] \quad (41)$$

$$\kappa_m^* = \frac{\rho_s \epsilon_s g_0 \Theta_s \kappa}{\rho_s \epsilon_s g_0 \Theta_s + \frac{6\beta_{gs}\kappa}{5\rho_s \epsilon_s}} \quad (42)$$

$$\kappa = \frac{75\rho_s d_p \sqrt{\pi\Theta_s}}{48\eta(41 - 33\eta)} \quad (43)$$

3.6. Turbulence Model

Effect of gas phase turbulence has been investigated by many CFD studies. One of the most well known model is $k - \epsilon$ model where k represents turbulent kinetic energy and ϵ refers for dissipation of this turbulent kinetic energy. MFIX uses a modified turbulence model which is very similar to single phase $k - \epsilon$ model except the addition of solid phase influence on gas phase. [51]-[52]. Governing equations for gas phase is given in Equations (44) and (45). Please note that in these turbulence equations, subscripts of 1 and 2 are representing gas and solid phases respectively. This has been done to distinguish turbulence parameters from void fractions or conductivities.

$$\epsilon_g \rho_g \left[\frac{\partial k_1}{\partial t} + U_{1j} \frac{\partial k_1}{\partial x_j} \right] = \frac{\partial}{\partial x_i} \left(\epsilon_g \frac{\mu_1^t}{\sigma_k} \frac{\partial k_1}{\partial x_i} \right) + \epsilon_g \tau_{1ij} \frac{\partial U_i}{\partial x_j} + \Pi_{k1} - \epsilon_g \rho_g \epsilon_1 \quad (44)$$

$$\begin{aligned} \epsilon_g \rho_g \left[\frac{\partial \epsilon_1}{\partial t} + U_{1j} \frac{\partial \epsilon_1}{\partial x_j} \right] \\ = \frac{\partial}{\partial x_i} \left(\epsilon_g \frac{\mu_1^t}{\sigma_\epsilon} \frac{\partial \epsilon_1}{\partial x_i} \right) + \epsilon_g \frac{\epsilon_1}{k_1} \left(C_{1\epsilon} \tau_{1ij} \frac{\partial U_i}{\partial x_j} - \rho_g C_{2\epsilon} \epsilon_g \right) \\ + \Pi_{\epsilon 1} \end{aligned} \quad (45)$$

For solids phase, turbulent kinetic energy is defined by granular temperature and turbulence equation is derived accordingly as [56]

$$\begin{aligned} \epsilon_s \rho_s \left[\frac{\partial \Theta_s}{\partial t} + U_{2j} \frac{\partial \Theta_s}{\partial x_j} \right] \\ = \frac{\partial}{\partial x_i} \left(\epsilon_s \rho_s \kappa_s \frac{\partial \Theta_s}{\partial x_i} \right) + \epsilon_s \rho_s \tau_{2ij} \frac{\partial U_{2i}}{\partial x_j} + \Pi_{k2} - \epsilon_s \rho_s \epsilon_2 \end{aligned} \quad (46)$$

Closure equations are based on the study done by Cao and Ahmadi [57] since their model is used in this thesis. These constitutive equations are implemented in MFIX and called as Ahmadi model [56].

Π_{k1} , $\Pi_{\epsilon1}$ and Π_{k2} are turbulence interaction terms which show solid particle effects on turbulence. They are defined as

$$\Pi_{k1} = \beta_{gs} (3\Theta_s - 2k_1) \quad (47)$$

$$\Pi_{\epsilon1} = 0 \quad (48)$$

$$\Pi_{k2} = \beta_{gs} \left(\frac{2k_1}{1 + \tau_{12}^x / \tau_1} - 3\Theta_s \right) \quad (49)$$

where β_{gs} is drag coefficient. τ_{12}^x and τ_1 are particle relaxation time and time-scale of turbulent eddies respectively. Details of these parameters can be found in literature. [56].

Stress tensors are the same as the ones given in Equations (34) and (35), however solid pressure is redefined as

$$P_s = \epsilon_s \rho_s \Theta_s [(1 + 4\epsilon_s g_0) + 1/2(1 - e^2)] \quad (50)$$

Solid viscosity, μ_s and solid bulk viscosity, μ_b are defined as

$$\mu_s = \left[1 + \left(\frac{\tau_1^t}{\tau_{12}^x} \right) \left(1 - \frac{\epsilon_s}{\epsilon_{s,max}} \right)^3 \right]^{-1} \left[0.1045 \left(\frac{1}{g_0} + 3.2\epsilon_s + 12.1824g_0\epsilon_s^2 \right) d_p \rho_s \sqrt{\Theta_s} \right] \quad (51)$$

$$\mu_b = \frac{5}{3} \left[1 + \left(\frac{\tau_1^t}{\tau_{12}^x} \right) \left(1 - \frac{\epsilon_s}{\epsilon_{s,max}} \right)^3 \right]^{-1} \left[0.1045 (12.1824g_0\epsilon_s^2) d_p \rho_s \sqrt{\Theta_s} \right] \quad (52)$$

where μ_1^t is gas turbulent viscosity or eddy viscosity defined with

$$\mu_1^t = \rho_s C_\mu \left[1 + \left(\frac{\tau_1^t}{\tau_{12}^x} \right) \left(1 - \frac{\epsilon_s}{\epsilon_{s,max}} \right)^3 \right]^{-1} \frac{k_1^2}{\epsilon_1} \quad (53)$$

Solid granular conductivity, κ_s in Ahmadi model is different from the model given in previous section. κ_s is defined for Ahmadi model with

$$\kappa_s = 0.1306 \rho_s d_p (1 + e^2) \left(\frac{1}{g_0} + 4.8\epsilon_s + 12.1184g_0\epsilon_s^2 \right) \sqrt{\Theta_s} \quad (54)$$

C_μ , $C_{1\epsilon}$, $C_{2\epsilon}$ are constants, values of which can be found in [56].

3.7. Conclusion

In this thesis, an open source software called MFIX [58] is used. MFIX consists of fortran based codes which includes all the fundamental theory explained in this section. It allows modifications on drag functions or definition of new user defined functions. Although fundamental equations and stress tensors are defined already, drag model and turbulence models are to be selected. Different options about wall boundary conditions about frictional and collisional behavior of particles, which are discussed in Chapter 4, are defined in input file and then compiled and solved by the software. Therefore, this thesis does not focus on working on theoretical details of these equations instead, it considers different modeling options and parameters to model the hydrodynamics of CFB model. Modeling effort is presented in Chapter 4.

CHAPTER 4

MODEL DEVELOPMENT

4.1. Computational model

In this section, circulating fluidized bed riser solar receiver is described and details of model development is discussed. All of the CFD models are developed in open source software, Multiphase Flow with Interphase eXchanges (MFIx) code of National Energy Technology Laboratory (NETL) [58]. In this software, an Eulerian-Eulerian two-fluid model is used, details of which can be found in Chapter 3.

4.2. Examination of Model Parameters

Various model parameters affect the solution in two-fluid method. In order to understand these effects, a simple bubbling fluidized bed model was constructed for which experimental data are available. Grid independence study, different drag models, various wall boundary conditions and effect of turbulence model were investigated and compared with the experimental data in order to build an optimum hydrodynamics model. This model parameter examination study (Section 4.2) was presented in the 6th International Conference on Advances in Computational Heat Transfer [59]. The experimental study used for validation was performed by Deza [60].

4.2.1. Bubbling Bed Model Used for Investigation of Model Parameters

Deza [60] used 9.5cmx40cm bed filled with glass beads. Experimental data was taken from two perpendicular slices in 3D geometry which were called as x-slice and

y-slice. Both glass beads and the sand that we used in the actual riser are classified as B type according to Geldart type classification [26], hence both of them are expected to have similar fluidization behaviors.

Fluidized bed was initially filled with glass beads up to 10 cm height. Air was uniformly supplied from the bottom. Schematic for this simple fluidized bed is given in Figure 16.

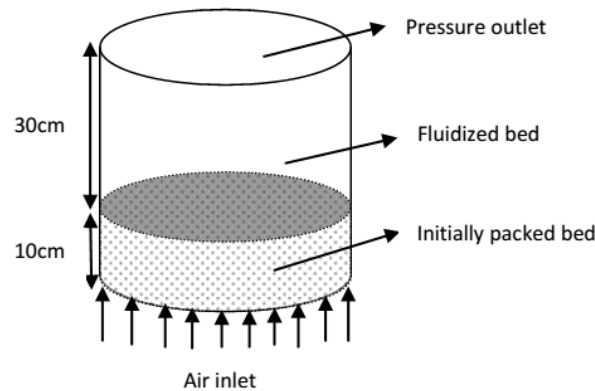


Figure 16 Schematic of simple fluidized bed used for model optimization and experimental validation (Adapted from [59])

Glass beads are spherical, while sand particles have variety of sphericities depending on the location where the sand is obtained. Properties of the glass beads used in modeling are presented in Table 3.

Table 3 Properties of glass beads

d_p (μm)	Φ_s	ρ_s (kg/m ³)	ϵ_{pb}	U_{mf} (m/s)
550	1	2600	0.373	0.199

In our transient 2D axisymmetric numerical model, the bed was initially loaded with glass beads up to 10 cm height and superficial air velocity of $1.3U_{mf} = 0.256\text{m/s}$

was supplied from the bottom of the bed. Air properties were obtained at 293K from textbook of Bergman et al. [61]. The time step size was initially selected as 10^{-5} . However, obtaining convergence in the shortest time was provided by time-step adjustment algorithm of MFIX [46]. The total maximum residual at convergence was taken as 10^{-3} . The transient simulations were performed for 40 seconds and all of the data presented in this study is obtained by time averaging in every 0.01s between 5-40 seconds.

4.2.2. Grid Independence

Grid independence is important when dealing with CFD analyses. In such transient and unsteady analyses, it is hard to obtain perfect resolution by mesh refinement. In addition, due to particle size, there is a minimum limit for the grid size. As a rule of thumb, grid size is suggested to be maximum ten times the particle diameter [46]. Despite these facts, a grid independence study was done to show this and select an appropriate grid size. The grid sizes of 2.5mmx5mm, 2.5mmx2.5mm and 1.25mmx2.5mm were investigated. Comparison of the simulation results from these grid sizes with experimental results together with the results of the 2.5mmx5mm grid planar model of Deza [60] is given in Figure 17

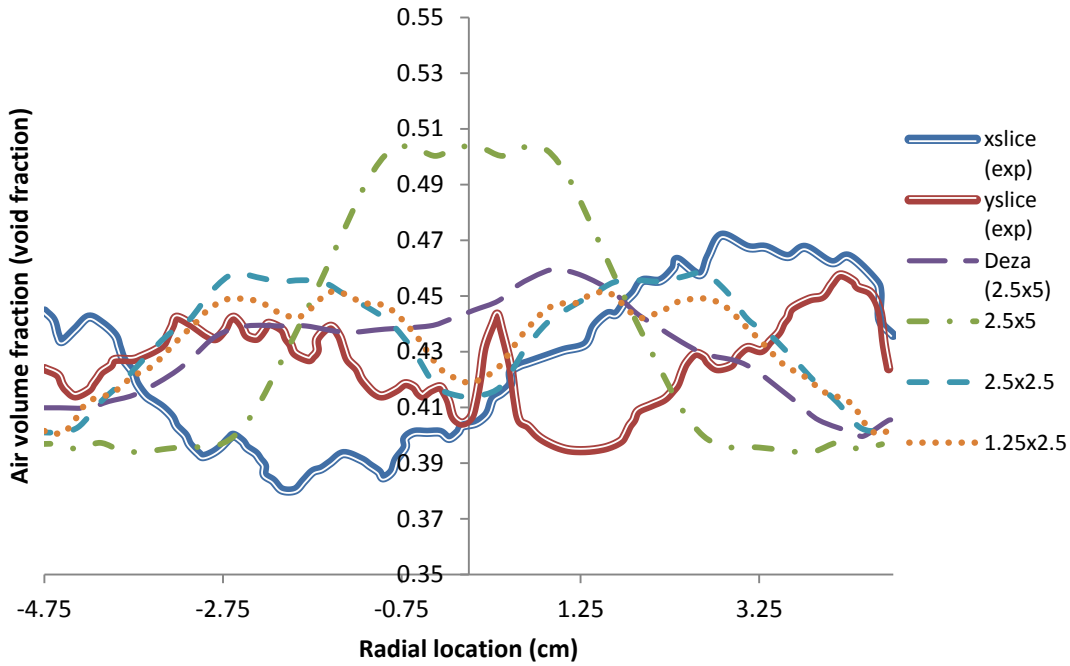


Figure 17 Radial distribution of time-averaged void fraction at 8cm height for grid resolution study

It can be seen that the grid sizes of 1.25mmx2.5mm and 2.5mmx2.5mm gave similar results while a big deviation is distinguishable between 2.5mmx5mm and 2.5mmx2.5mm grid sizes. Since accuracy of radial void fraction profile is important, grid resolution is adjusted accordingly. Percent differences of coarse grid void fraction results with respect to the finest grid (1.25mmx2.5mm) results are plotted in Figure 18. In order to have the same number of cells to compare with double sized grid, data for the finest grid is arithmetically averaged in every two cells. Percentage deviation is calculated as

$$\% = \frac{(Data\ of\ finest\ grid - Data\ of\ current\ grid) * 100}{Data\ of\ finest\ grid} \quad (55)$$

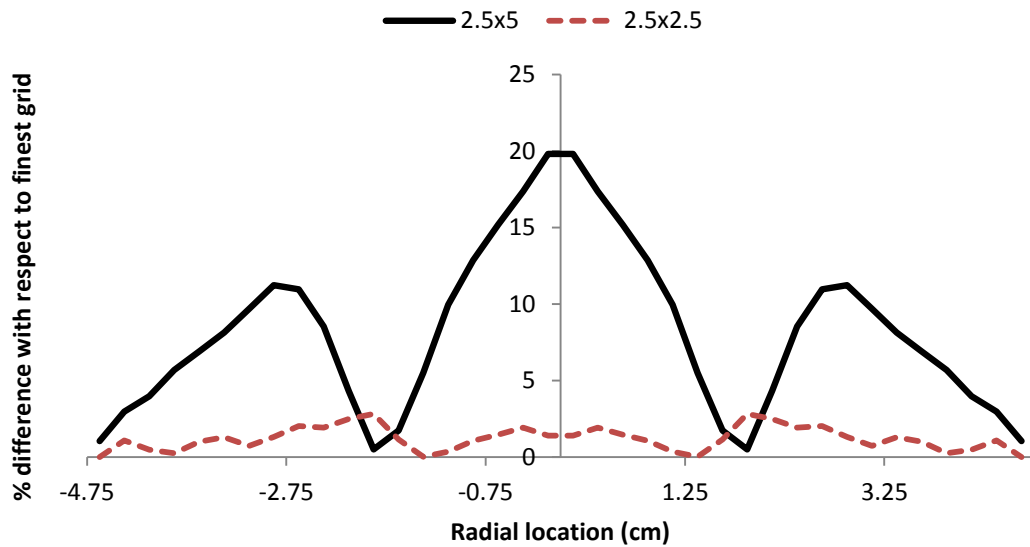


Figure 18 Percentage void fraction deviations along radial location at 8cm height for different meshes with respect to finest mesh

It can be seen in Figure 18 that 2.5mmx2.5mm grid size shows only a maximum deviation of 2.5%. Therefore, the grid size of 2.5mmx2.5mm was selected for the upcoming analyses.

4.2.3. Drag Models

Interphase momentum transfer is one of the most important phenomena affecting the fluidization characteristics in a fluidized bed. Drag force is the most dominant force in fluidization regarding the fluid-solid momentum transfer. Syamlal O'Brien [46] and Gidaspow [49] drag models were compared in this section. Details of these models were given in Chapter 3. Syamlal model was based on a terminal velocity correlation, which depends on coefficients c_1 and d_1 that should be adjusted according to experimental minimum fluidization velocity, particle diameter and density. Minimum fluidization velocity was calculated by formulation of Syamlal [44], which is given with

$$U_{mf} = \frac{\epsilon_g Re_{mf} \mu_g}{d_p \rho_g} \quad (56)$$

Re_{mf} in equation is depended on modified Archimedes number, c_1 and d_1 details of which can be found in literature. [44] c_1 is a constant and d_1 is function of c_1 , which is defined as

$$d_1 = 1.28 + \frac{\log(c_1)}{\log(0.85)} \quad (57)$$

After particle diameter, particle density and thermodynamic properties of air were supplied, c_1 was iteratively changed until U_{mf} in Equation (56) matches with experimental U_{mf} which is 0.199 m/s for glass beads [60]. For our case, the coefficients were adjusted as $c_1=0.55$ and $d_1=4.959$.

Drag models were compared according to the radial distribution of time-averaged void fraction at 8cm height in Figure 19.

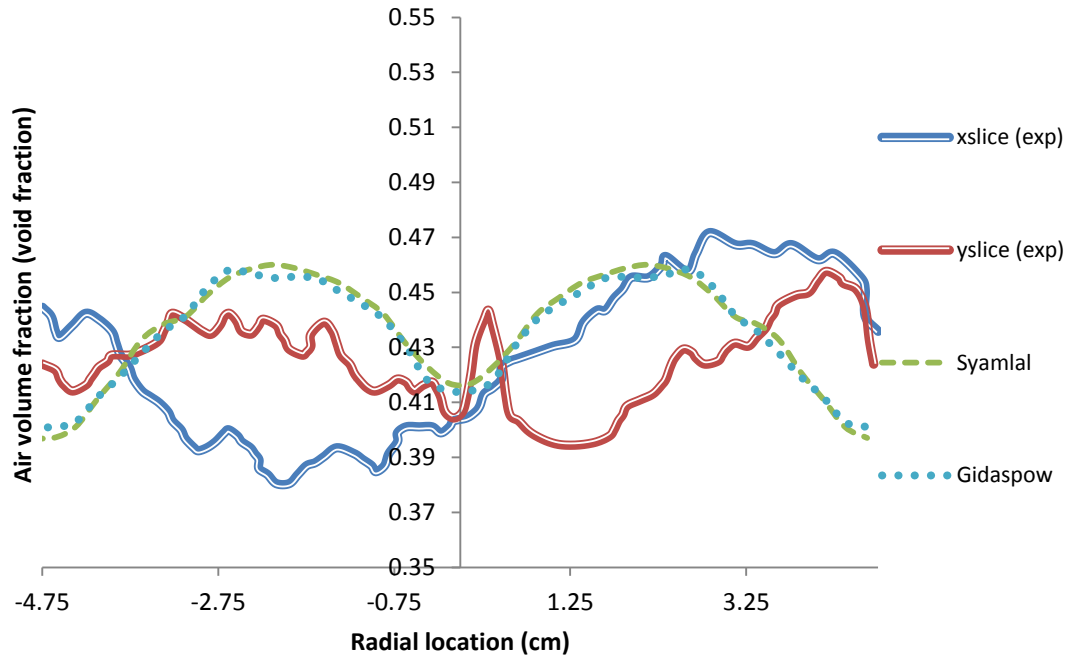


Figure 19 Radial distribution of time-averaged void fraction at 8cm height for different drag models

It is clear in Figure 19 that Syamlal O'Brien and Gidaspow drag models showed nearly no difference in accuracy. Since Gidaspow model does not require experimental minimum fluidization velocity, it is preferable in case of lack of experimental data. [60] Therefore, it was selected for use in the remaining studies and final model.

4.2.4. Wall Boundary Conditions

Wall boundary condition is significant in modeling of fluidized bed systems. Since the solar radiative flux will be imposed on the wall, accurate prediction of void fraction in wall region is important. Roughness of the wall, slip conditions, tangential momentum transfer and collisional/frictional behavior of particles are reasons of this importance. Frictional behavior is characterized by wall roughness and particle surface. Due to frictional and collisional characteristics gas or particles may slip at

the wall and lose energy. Relationship between slip condition and surface characteristics is illustrated in Figure 20.

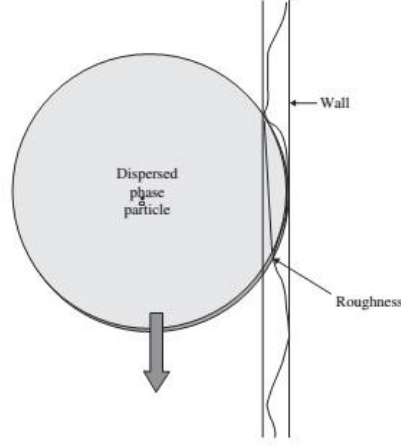


Figure 20 Illustration of relationship between slip condition and surface characteristics for solid particles (Adapted from [45])

In this study, no slip condition for both phases and partial slip condition suggested by Johnson&Jackson [62] are discussed.

Johnson&Jackson partial slip friction model [62] assumes that some particles are freely slipping at the wall and the others slide at the wall. Equating the tangential force at the wall to the sum of forces due to collisional and frictional stresses, Johnson&Jackson derived expression for slip velocity at the wall as [62]-[63].

$$\frac{u_{sl} \cdot (\sigma_c + \sigma_f) \cdot n}{|u_{sl}|} + \frac{\phi \sqrt{3\theta} \pi \rho_s \epsilon_s |u_{sl}|}{6 \epsilon_{s,max} \left(1 - \left(\frac{\epsilon_s}{\epsilon_{s,max}} \right)^{\frac{1}{3}} \right)} + N_f \tan(\delta) = 0 \quad (58)$$

u_{sl} is slip velocity at wall, σ_c and σ_f are stress tensors due to collision and friction respectively and n is vector normal to wall. N_f is normal friction component of stress and δ is friction angle between wall and particles. Here, specularity coefficient (ϕ) is defined to characterize the particle-wall collision. Zero value of specularity means collision is fully specular and particles are freely slipping at the wall while a value of unity is the same as no slip condition [62]-[63]. For bubbling regime, a moderate

value (e.g. ~0.5) is suggested where for dilute regimes low specularly values are preferred. [64] Li and Benyahia [63] developed a variable specularly model to determine this coefficient through the wall by adopting classic rigid body theory and kinetic theory to Johnson&Jackson partial slip model.

Another boundary condition for granular energy equation is derived by Johnson&Jackson as [62]-[63].

$$-n \cdot q_{PT} = D + u_{sl} \cdot S_c^b \quad (59)$$

q_{PT} is the flux of granular energy, S_c^b is the force per unit area on the wall due to particle-wall collisions and D is dissipation of granular energy due to inelastic collisions which is defined as [62]-[63].

$$D = \frac{1}{4} \pi \rho_s d_s^3 \Theta (1 - e_w^2) \frac{\sqrt{3\Theta}}{d_p \left[\left(\frac{\epsilon_{s,max}}{\epsilon_s} \right)^{\frac{1}{3}} - 1 \right]} \frac{1}{d_p^2 \left(\frac{\epsilon_{s,max}}{\epsilon_s} \right)^{2/3}} \quad (60)$$

The parameter e_w is particle-wall restitution coefficient which describes energy dissipation of particles due to wall interaction. e_w is defined between 0 and 1. As it can be seen in equation, a value of 1 for e_w refers zero energy dissipation due to collision since D will be zero. If e_w is 1, all the granular energy of particle disappears after collision.

First of all, a parametric study was done for specularly coefficient. Cases for Johnson&Jackson partial slip model [62] with specularly coefficients of 0.01, 0.1, 0.6, 0.8, 1 and variable specularly coefficient of Li&Benyahia [63] were examined. Time averaged void fraction profile results at 8cm height were plotted with no slip case results and experimental results in Figure 21.

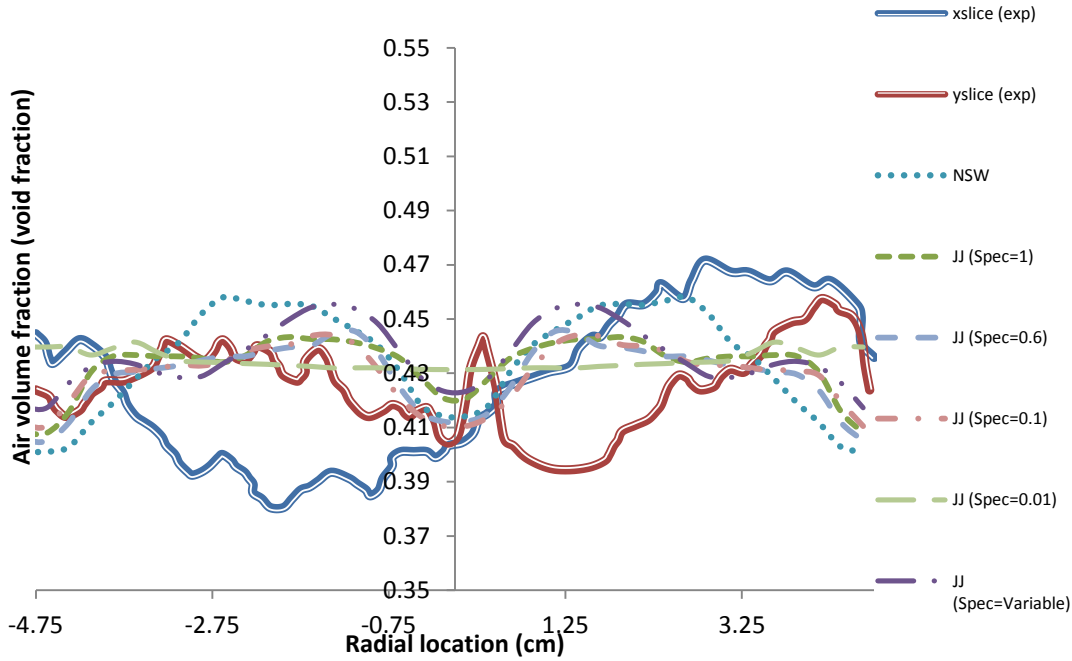


Figure 21 Radial distribution of time-averaged void fraction at 8cm height using Johnson&Jackson partial slip wall boundary condition with different specularly coefficients

As it can be seen in Figure 21, Johnson&Jackson (JJ) partial slip results differed from no slip results and specularly coefficient (ϕ) had strong effect on results. No significant difference was observable between $\phi = 0.1$ and $\phi = 0.6$ but bubble formation was undistinguishable for specularly coefficient less than 0.1. Therefore, for bubbling fluidized bed models, that parameter should not be less than 0.1. When results were compared with experimental data of Deza [60], best cases were Johnson&Jackson partial slip model for $\phi = 0.6$ and $\phi = \text{variable}$. However specularly has significant effect on radial distribution of solid particles, so that different values should be considered when the flow regime is changed. It was also reported in the literature that smaller specularly coefficient should be considered for riser case [37][65]-[66].

Secondly, effect of particle-wall restitution coefficient, e_w on radial distribution of void fractions is investigated. For this parameter, cases of 0.2,0.4, 0.8 and 1 were

examined. For all cases, specularity was fixed to 0.6. Similar to the representation for specularity cases, results were compared with experimental data in Figure 22.

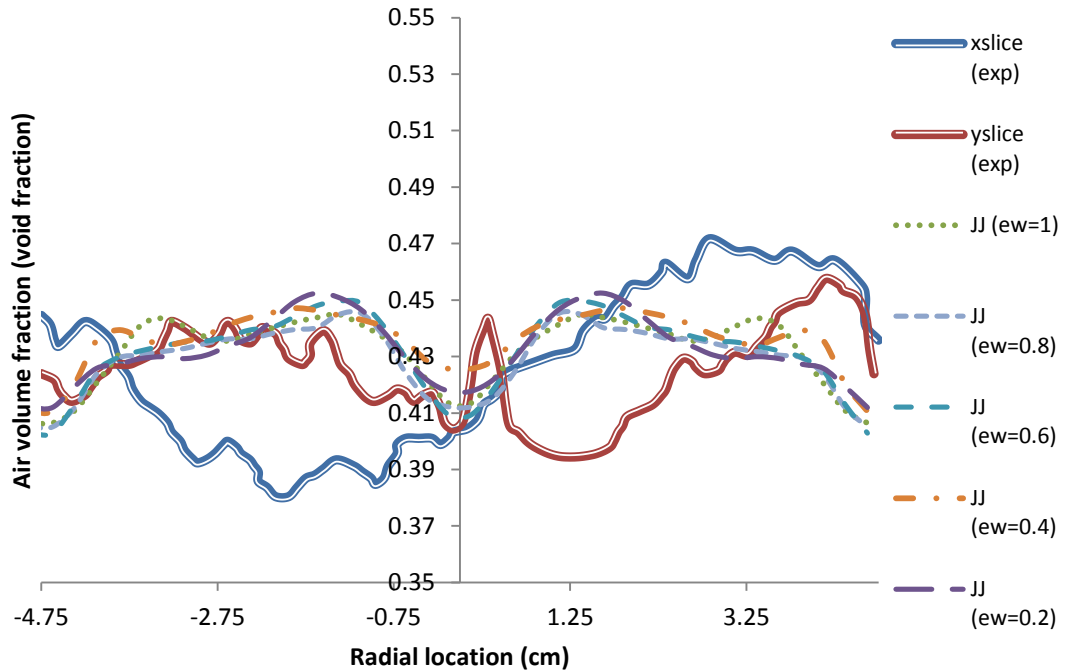


Figure 22 Radial distribution of time-averaged void fraction at 8cm height using Johnson&Jackson partial slip wall boundary conditions with different particle-wall restitution coefficients

Although, no significant difference was observed between different cases in Figure 22, particle-wall restitution coefficient may affect the void fraction near the wall and should be adjusted according to better fit with the experimental results. Reducing e_w might cause a small shift-up of void fraction near the wall and in the middle as it can be noticed for cases of $e_w = 0.4$ and $e_w = 1$ in Figure 22.

4.2.5. Turbulence models

Effect of turbulence can be very important especially when gas phase velocities are high. It is also reported that for large particles ($>100 \mu\text{m}$) turbulence may affect the flow [44]. Since our particles are relatively large Geldart B particles and gas

velocities are expected to increase in riser section, turbulence is supposed to be significant and should be modeled. For gas phase, $k - \epsilon$ model was used. A modified version of $k - \epsilon$ model was used in which effect of solid phase to gas phase turbulence is also considered. In this modified version, constitutive relations for solid phase parameters were derived by Cao and Ahmadi [57]. Details of $k - \epsilon$ model and Ahmadi model is given in Chapter 3.

Another wall boundary condition depending on turbulence model was also examined. This wall boundary condition model was based on an analytical description of particle-wall frictional behavior derived by Jenkins [67]. Two extreme cases were considered in Jenkins's model which are "small friction/all sliding" and "large/friction no sliding" limit. In no sliding limits, friction is assumed to be very large so that particles are sticking to the wall. Jenkins model is based on a proper interpolation of these two cases. Jenkins boundary condition implemented in MFIX is defined as in Equations (61) and (62) which represent force balance and granular energy balances respectively [56].

$$\mu_s \left. \frac{\partial u_2}{\partial x} \right|_w = P_s \tan(\phi_w) \frac{u_s}{|u_s|} \quad (61)$$

$$\kappa_s \left. \frac{\partial \Theta_s}{\partial x} \right|_w = P_s \sqrt{3\Theta_s} \frac{3}{8} \left[\frac{7}{2} (1 - e_w) \tan^2(\phi_w) - (1 - e_w) \right] \quad (62)$$

Angle of internal friction Φ_w was to be determined which relates tangential and normal components of the impulse. That value was taken as 11.31deg, which is a suggested value in MFIX software [46].

Considering the similar experimental data discussed in previous sections, $k - \epsilon$ turbulence model, Ahmadi model and Ahmadi model with Jenkins boundary conditions were compared in Figure 23.

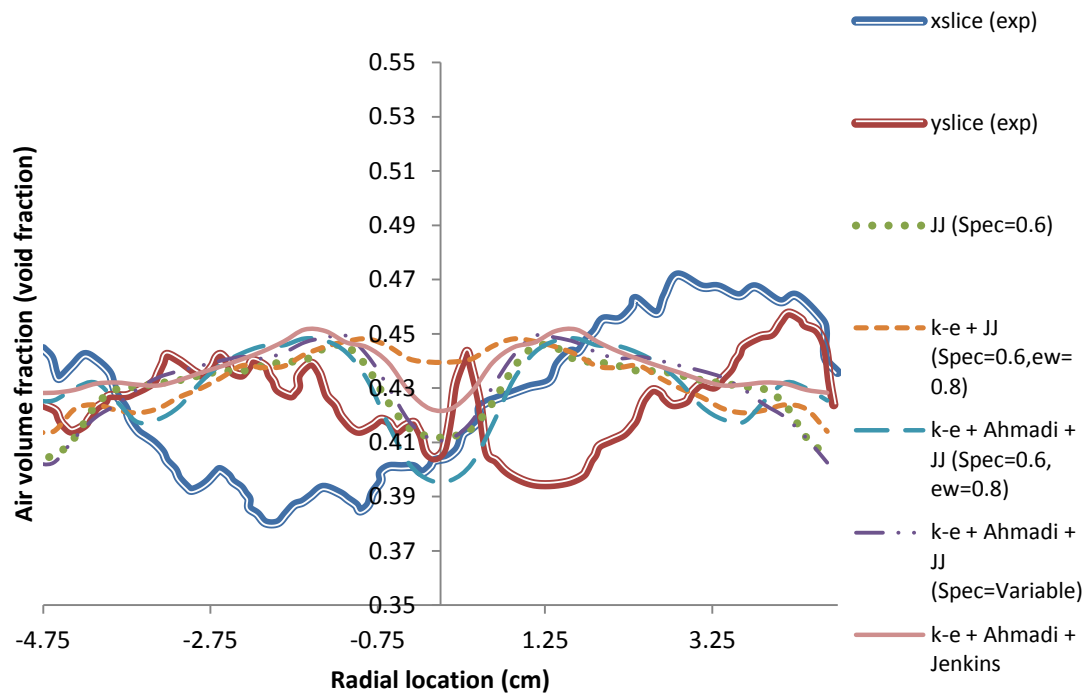


Figure 23 Radial distribution of time-averaged void fraction at 8cm height for investigation of k-e turbulence model and Ahmadi model and Jenkins wall boundary condition

When $k - \epsilon$ turbulence model was used, void fraction at the middle was increased and better prediction of void fraction at the wall was obtained. Better agreement with experimental data was noticeable when $k - \epsilon$ turbulence model was used with Ahmadi model. Both Ahmadi-JJ and Ahmadi-Jenkins combinations could predict the void fraction at the wall accurately. On the other hand, no peak of void fraction near the wall could be seen with Jenkins model. From Figure 23, Ahmadi model and JJ wall boundary condition with $\phi = 0.6$ was selected to be the best. For this best case, various particle-wall restitution coefficients were examined for optimization in Figure 24.

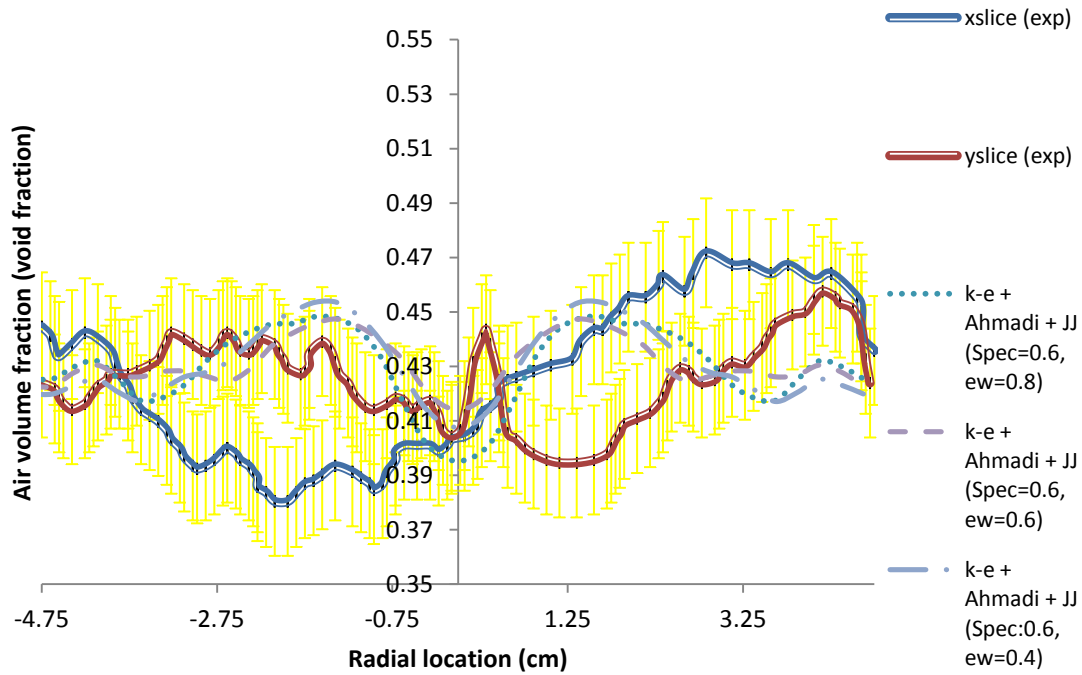


Figure 24 Radial distribution of time-averaged void fraction at 8cm height for investigation of wall-restitution coefficients for the best model selected. Experimental data are given with the associated error bars.

Experimental void fraction error is determined in Deza's study as ± 0.02 . This fixed error amount is applied to both x-slice and y-slice data and shown as error bars in Figure 23. It is clearly be seen that all of the results drops within the error bars in most of the locations. This claims that the results can estimate the magnitude of the void fractions well in most of the radial locations, although the radial distribution profiles are not in a good match. Among the cases shown in Figure 24, e_w of 0.6 was selected. For the selected case, time averaged and radially averaged void fraction across the bed height were compared with the experimental data and a good agreement was observed in Figure 25.

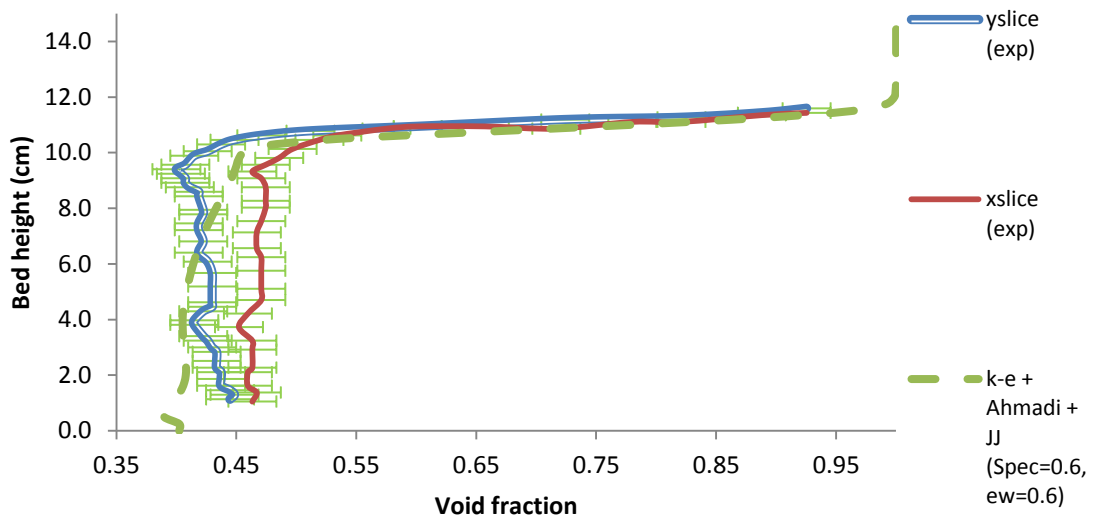


Figure 25 Time averaged void fraction along bed height for data spatially averaged across the radial location of the bed for comparison of the best model with the experimental data. Experimental data are given with the associated error bars.

4.3. Circulating Fluidized Bed Riser Model

Flow regimes in circulating fluidized bed risers differ from bubbling fluidized beds. Gas velocities must be higher than terminal velocity to carry the particles upwards in the riser. Therefore, usually velocities are high, which causes dilute regimes especially for Geldart B particles. Depending on flow conditions, generally core-annulus regime with cluster formation occurs at the wall. At low superficial gas velocities, even downward annulus flow exists. However, when the velocities are high, particles move upwards as well [44]. This condition is shown in Figure 26. For both conditions, solid volume fraction is larger in the annulus region, but mass flux is greater in the core region.

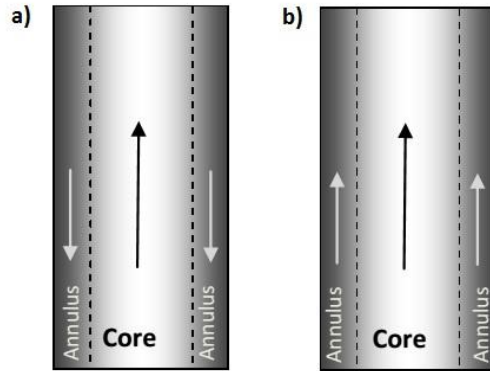


Figure 26 Core annulus flow regime in circulating fluidized bed risers a) For low superficial gas velocities, b) For high superficial gas velocities

In light of the information presented above, a model validation is required for CFB riser section as well. Validation was done by applying the model to an experimental CFB study and adjusting wall boundary conditions to obtain closest results to the experimental results in the following sub-sections.

4.3.1. Modeling of an Experimental CFB Study

Experimental study selected for model validation was done by Mastellone [68]. This study was selected because riser geometry was appropriate to be able to solve with CFD in reasonable times and particles used in this study was similar to the ones used in the main riser receiver model of this thesis. Mastellone [68] used FCC, Ballotini and silica sand particles. Data for silica sand particles having diameter of $310\mu m$ and density of $\rho_s = 2600kg/m^3$ was used from this study.

Schematic of the system used by Mastellone is shown in Figure 27.

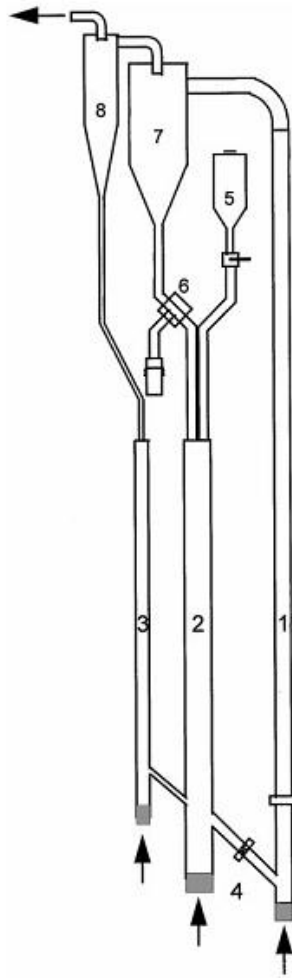


Figure 27 Schematic of CFB system used in Mastellone's study. (1) riser; (2) and (3) recirculation standpipes; (4) solids control butterfly valve; (5) feed hopper; (6) three ways valve; (7) and (8) cyclones (Adapted from [68])

The riser had internal diameter of 0.12m and height of 5.75m. 2D axisymmetric model was constructed in MFIX. Model parameters were selected in light of the bubbling bed study explained in Section 4.2. except specularly and particle-wall restitution coefficients. These coefficients were adjusted to obtain a better fit with the experimental data.

The riser was initially filled with particles up to 0.3m height with particles having volume fraction of 0.6. Solid particles with flux of $55\text{kg}/\text{sm}^2$ were fed at 0.3m

height via 0.1m gap. Air was supplied from bottom of the riser with vertical velocity of 6m/s.

The simulation was performed for 10 seconds and data was taken for every 0.05 seconds. Time averaged results were taken for time range of 5-10 seconds. For some cases, analysis had been performed for 20 seconds and no big difference was distinguished between time averaged data for 5-10 seconds time range and 10-20 seconds time range. Therefore, steady operation was assumed to be achieved in the first 5 seconds.

Simulation parameters are summarized in Table 4.

Table 4 Simulation parameters used for modeling Mastellone's case

Simulation Parameter	Value
Grid size	2.5x2.5 (mmxmm)
Time step	5×10^{-5} (Adjustable)
U_g	6 (m/s)
Solid circulation rate	55 (kg/sm ²)
Drag model	Gidaspow
Turbulence model	$\kappa - \epsilon$
Wall Boundary Condition	JJ
Particle-particle restitution	0.95
Solid Phase Stress Model	Ahmadi
Numerical Method	Higher order van Leer
Total maximum residuals at convergence	10^{-3}

For validation and optimization of wall boundary condition parameters, radial distribution of mass flux and spatially averaged void fraction data were used.

4.3.2. Optimization of Wall Boundary Condition Parameters

Due to frictional and collisional interactions between particles and wall, kinetic energy and velocity direction of particles change at the wall. In most of the studies, void fraction and solid vertical velocity decrease at the wall region. Therefore, modeling of particle-wall interaction is important and parameters like specular coefficient (ϕ) and particle-wall restitution coefficient (e_w) should be adjusted to fit well with the experimental CFB study. For specular coefficient, while a moderate value like 0.5 is suggested for bubbling bed cases, very small values in the order of magnitude of 10^{-4} are suggested for CFB risers [34][61]-[62][65].

Firstly, effect of specular coefficient was examined and a proper specular coefficient was selected. For $e_w = 0.8$, different specular coefficients were considered. Radial distribution of mass flux at 4.23m height was given in Figure 28

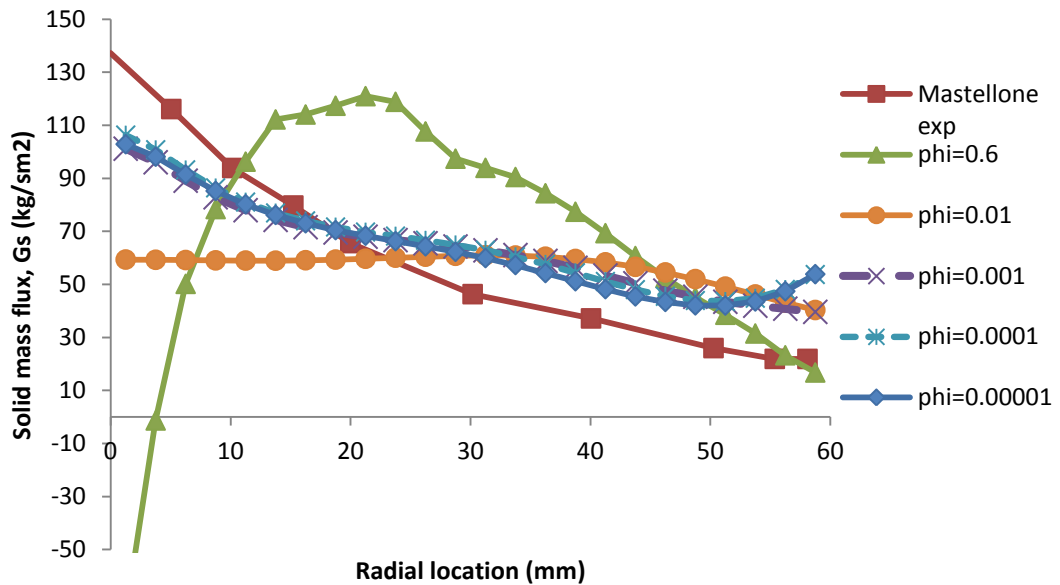


Figure 28 Radial distribution of solid mass flux at 4.23m height of Mastellone's case for various specular coefficients

As it can be seen in Figure 28, high specular coefficients like $\phi = 0.6$ and $\phi = 0.01$ gave abrupt results for riser case. Although the profiles were closer for

small specularly values, mass flux near the wall was overestimated for cases of $\phi = 0.0001$ and $\phi = 0.00001$. Therefore, it seems that $\phi = 0.001$ gave the closest profile compared to experimental data.

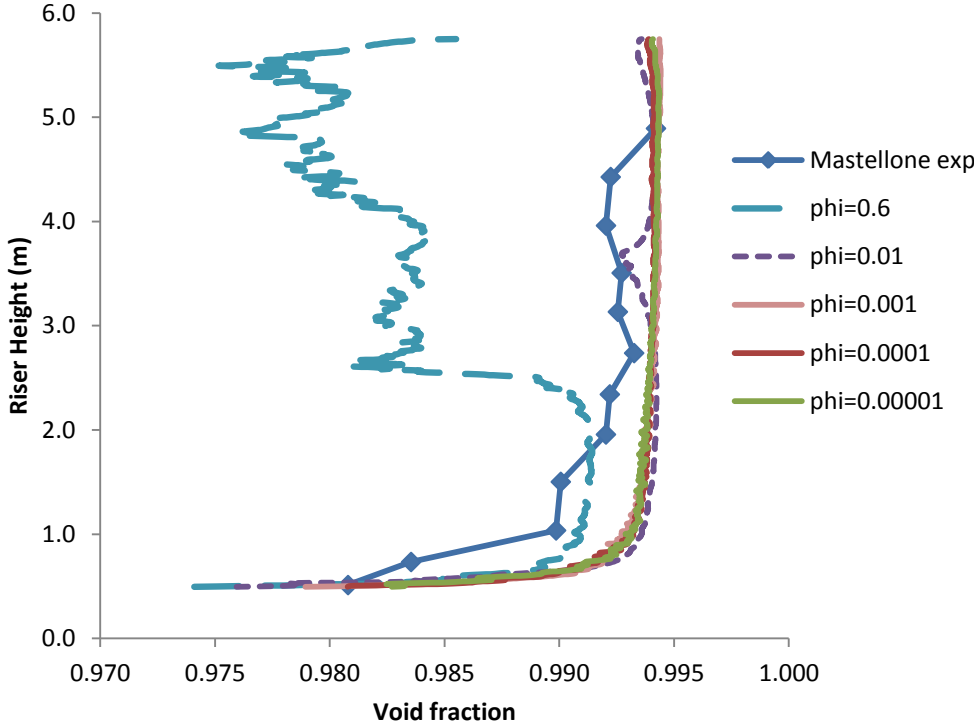


Figure 29 Time averaged and radially averaged void fraction along the riser for various specularly coefficients

Significant differences between $\phi = 0.6$ and other cases are also distinguishable in Figure 29. Reasonable results were obtained for specularly values less than 0.01. Beyond that value, results did not differ so much in terms of radially averaged void fractions.

For specularly coefficient of $\phi = 0.001$ and $\phi = 0.005$, effect of particle-wall restitution coefficient was examined. Results are presented in Figure 30 and Figure 31.

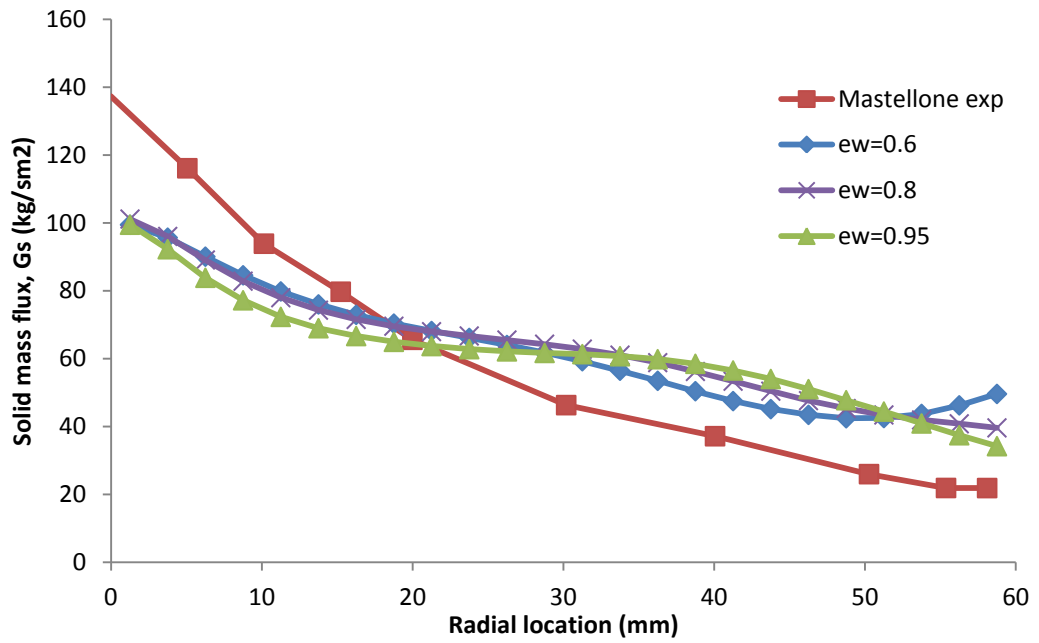


Figure 30 Radial distribution of solid mass flux at 4.23m height of Mastellone's case for various particle-wall restitution coefficients when $\phi = 0.001$.

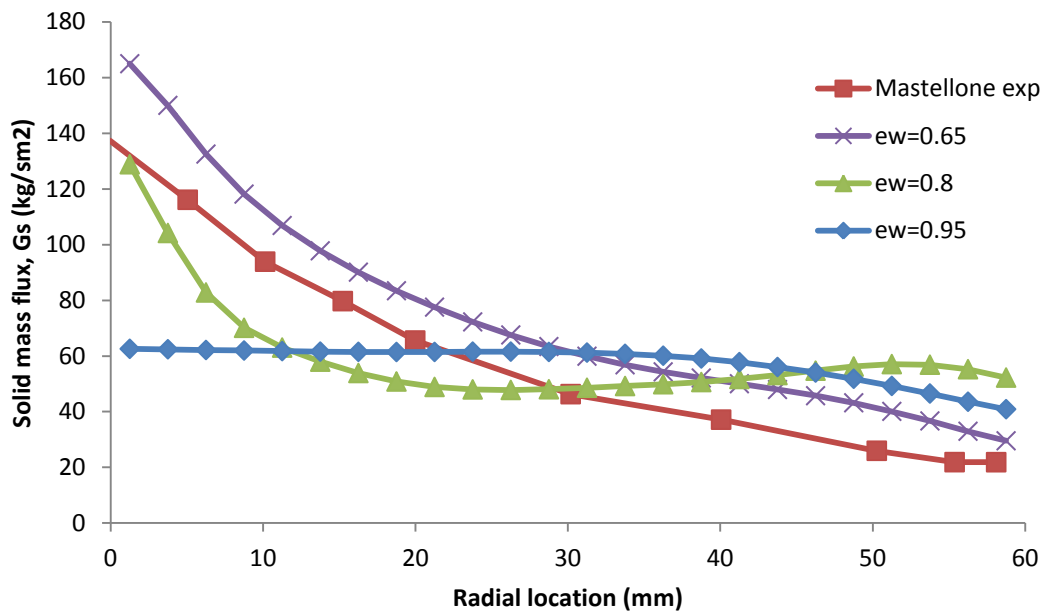


Figure 31 Radial distribution of solid mass flux at 4.23m height of Mastellone's case for various particle-wall restitution coefficients when $\phi = 0.005$

Mass flux at the wall was increased when e_w was decreased in Figure 30. However, effect of particle-wall restitution coefficient was very obscure for $\phi = 0.001$ case. Results varied much when the specularity coefficient was increased. It is interesting in Figure 31 that, for $\phi = 0.005$, mass flux did not increased when e_w was changed from 0.8 to 0.65. Indeed, the case of $\phi = 0.005$ and $e_w = 0.65$, result was very close to the experimental data. The profile was absolutely parallel to experimental profile, the only difference was a shift up which could be occurred due to overestimation of the drag force. This case was selected to be the best case and spatially averaged void fraction along the riser was also compared with the experimental data in Figure 32 in which good agreement was achieved.

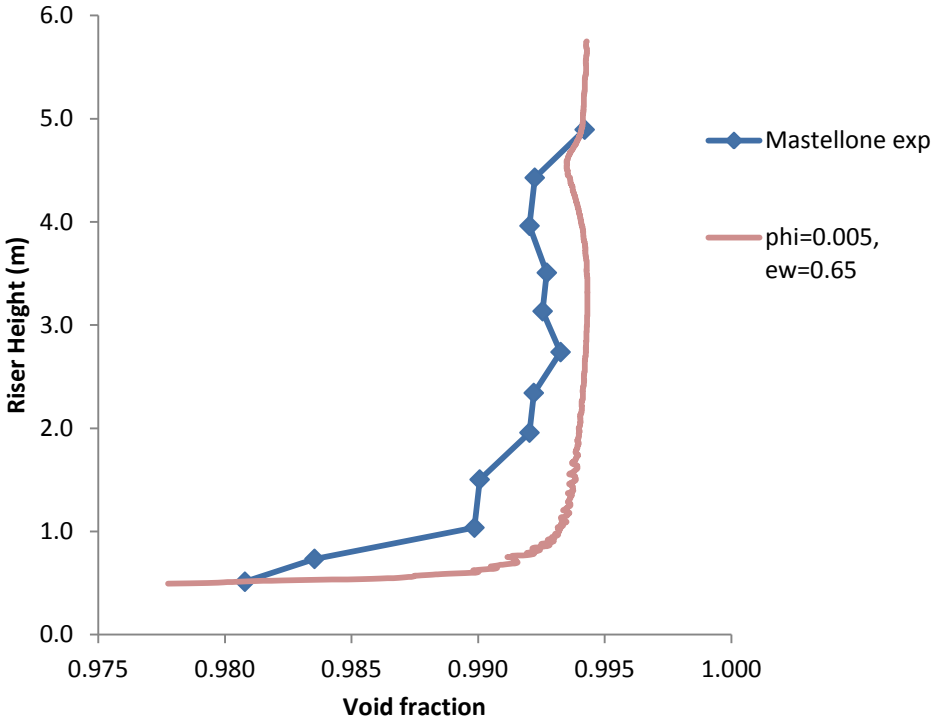


Figure 32 Time averaged and radially averaged void fraction along the riser for the best case.

4.3.3. Final Model Applied to CFB Riser Solar Receiver

Solar receiver used in this thesis is similar to receiver design of Flamant [6] and Boissiere [70]. The receiver consists of a riser and a fluidized bed. A riser pipe of 4cm diameter and 1 m length penetrates in a fluidized bed having diameter of 14cm and height of 40cm. The fluidized bed was initially filled with particles, but particles were disappeared due to upward move into the riser due to fluidization. Desired solid mass flux was provided via solid mass inlet. At steady operation, solid mass flux at solid mass inlet and outlet are expected to match. Solar radiation was planned to be introduced to a 50cm section of the riser. Schematic of riser receiver was given in Figure 33.

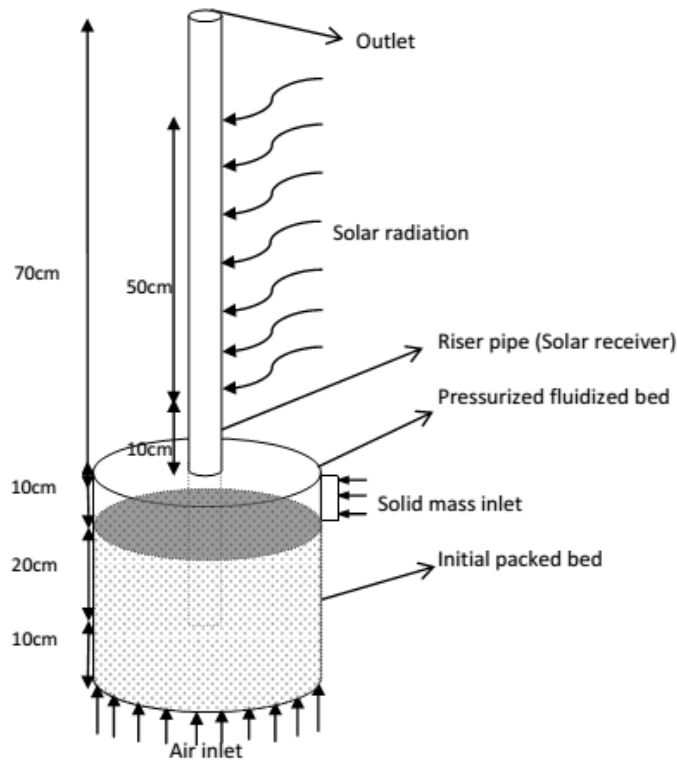


Figure 33 Schematic of circulating fluidized riser solar receiver

According to the riser geometry described in Section 4.1, a 2D axisymmetric riser model was developed in light of the model optimization study done with glass beads. Grid size is selected as the same with glass beads study which is 2.5mmx2.5mm.

This grid size refers to 28 cells in radial direction of the fluidized bed region, 8 cells in radial direction of the riser region and 440 cells in axial direction. The bed is initially filled with sand up to 30cm and solid mass inlet is located at 30-40cm from the bottom of the bed. The initial model can be seen in Figure 34 in which air is shown in red and the sand bed is presented in blue. Please note that EP_g in all contour plots refer to void fraction, ϵ_g .

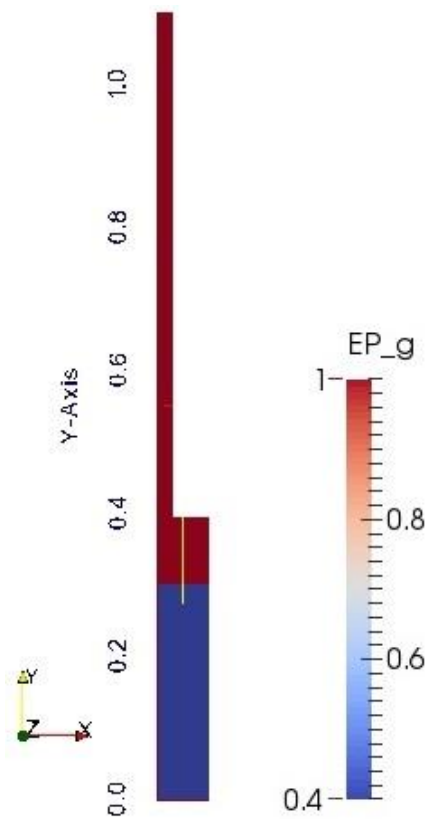


Figure 34 Initial condition of 2D axisymmetric riser model

The sand particle diameter was selected to be equal to the glass bead diameter used in the preliminary analyses, which is 550 μ m. Particles were considered as round sand for which sphericity value of $\Phi_s = 0.86$ was suggested by Knuii&Levenspiel [40] which was used to determine packed-bed void fraction. Packed-bed void fraction was determined as 0.4 from Figure 7 [40].

Minimum fluidization velocity was calculated by Wen-Yu equation (Equations (2),(3) and (4)) Using the solid and air properties at 293K, U_{mf} was determined as 0.23 m/s. The solid properties were tabulated in Table 5. The particle density and packed bed void fraction of sand was taken from textbook of Knuii&Levenspiel [40] and the air properties were taken from textbook of Bergman et al. [61].

Table 5 Physical properties of sand

d_p (μm)	Φ_s	$\rho_s(\text{kg/m}^3)$	ϵ_{pb}	$U_{mf}(\text{m/s})$
550	1	2600	0.4	0.23

In order to be consistent with preliminary analysis, superficial air velocity of $1.3U_{mf} = 0.3\text{m/s}$ was supplied to the bottom of the bed. Inlet and outlet static pressures are determined as 101.3 kPa. Solid circulation rate of 0.5kg/s with 0.5 void fraction was given to the mass inlet. This also provides extra air input from solid mass inlet. Amount of air supplied to the solid mass inlet is calculated to be the same as solid volumetric flow rate which is calculated as $2.39 \times 10^{-4} \text{ m}^3/\text{s}$. Simulation parameters were tabulated in Table 6.

Table 6 Riser simulation parameters

Simulation Parameter	Value
Grid size	2.5x2.5 (mmxmm)
Time step	5×10^{-5} (Adjustable)
U_g	0.3 (m/s)
Solid circulation rate	0.5 (kg/s)
Drag model	Gidaspow
Turbulence model	$\kappa - \epsilon$
Wall Boundary Condition	JJ
Φ	0.005
e_w	0.65
Particle-particle restitution	0.95
Solid Phase Stress Model	Ahmadi
Numerical Method	Higher order van Leer
Total maximum residuals at convergence	10^{-3}

CHAPTER 5

RESULTS

5.1. Mass Flow Rate

Although a solid mass flow rate was specified and constantly fed through the mass inlet, the same amount of mass flow rate could not be obtained every section of the riser. It was hard to achieve steady operating conditions, but comparison of radially averaged mass flow rates at different sections, especially at the outlet of the riser could give an idea about it. Using the output data, solid mass flux for a cell can be obtained from

$$G_s = \rho_s(1 - \epsilon_g)V_s \quad (63)$$

Average solid mass flow rate passing through a horizontal section can be calculated from

$$\overline{m}_s = \overline{G}_s A_{riser} \quad (64)$$

where \overline{G}_s is radially averaged solid mass flux and A_{riser} is cross-sectional area of the riser.

Radially averaged solid mass flow rates were calculated for heights of $y=0.2\text{m}$, 0.5m , 1m and 1.1m . Time averaged data was taken for every 10 seconds and plotted in Figure 35 to show the time dependent fluctuations of the flow at different sections. Time averaged data was represented as the data of the ending time. For instance, data for 10s showed the data for time range of 0-10 seconds.

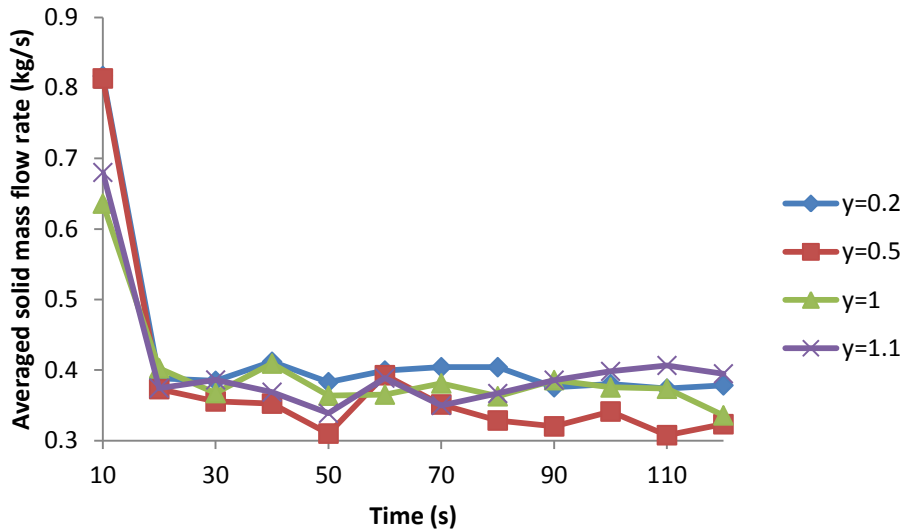


Figure 35 Time variation of radially averaged solid mass flow rates at different heights of the riser

High mass flux at the beginning stands for the discharge of initial packing. It can be seen in Figure 35 that mass flux was set around 0.3-0.4 kg/s range for all sections. Fluctuations were more uncertain in the bubbling bed ($y=0.2\text{m}$) than in the riser. For the riser sections, it was hard to notice steady flow during operation. Solid mass flow rate did not exceed 0.4 kg/s. Since mass flow rate at the inlet was 0.5 kg/s, it means 20% of the mass inlet was accumulating inside the bed.

In order to observe solid mass flow rate fluctuations, data can be presented in shorter time ranges without time averaging. First, time range of 0-1 seconds are presented in Figure 36.

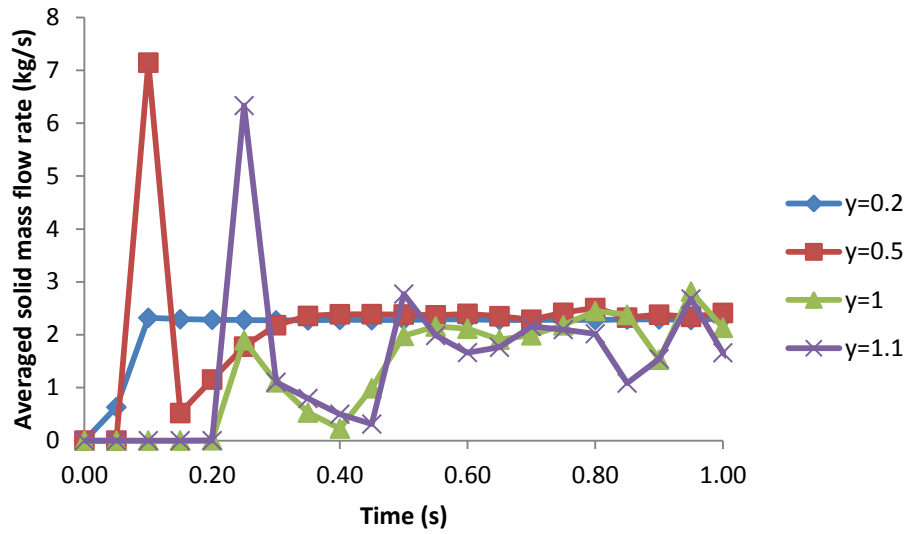


Figure 36 Averaged solid mass flow rates in 0-1 seconds time range

It can be seen in Figure 36 that, first solid particles reach to $y=1\text{m}$ and $y=1.1\text{m}$ sections at 0.2 seconds. While solid mass flow rate is set to 2 kg/s for $y=0.2\text{m}$ and $y=0.5\text{m}$ cases, fluctuations are more observable for other cases. Solid mass flow rate data in 1-5 seconds is given in Figure 37 and Figure 38.

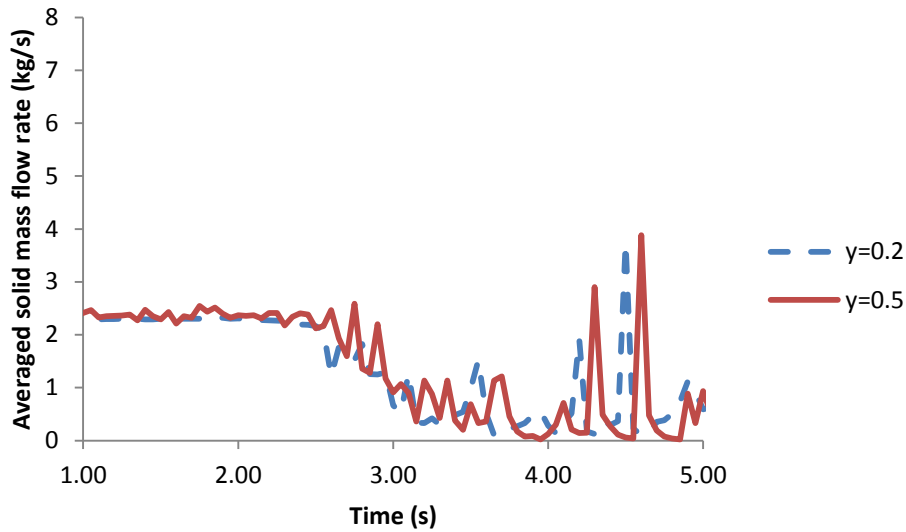


Figure 37 Averaged solid mass flow rate for $y=0.2\text{m}$ and $y=0.5\text{m}$ cases in 1-5 seconds

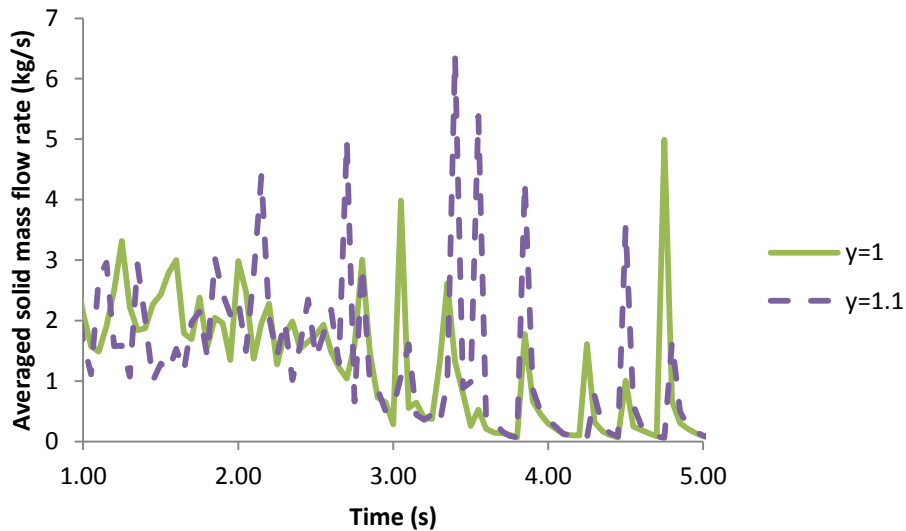


Figure 38 Averaged solid mass flow rate for $y=1\text{m}$ and $y=1.1$ cases in 1-5 seconds

Initial high mass flow rates due to discharging of initial packing can also be seen in Figure 37 and Figure 38. In Figure 36, while solid mass flow rates are stable in first 2.5seconds for $y=0.2\text{m}$ and $y=0.5\text{m}$, they decrease and start fluctuating after that point. In Figure 38, it can be observed that the mass flow rate is not stable for any

time range. $y=1\text{m}$ and $y=1.1\text{m}$ sections refer to riser regions at which solid particles are passing through as clusters periodically. This periodic behavior is more distinguishable after 4 seconds which can be seen in Figure 38.

It is expected that as the time passes, flow becomes more steady and this periodic solid mass flow behavior becomes more clear. Similar to the representation of data for 1-5 seconds time range, data is presented for 115-120 seconds in Figure 39 and Figure 40.

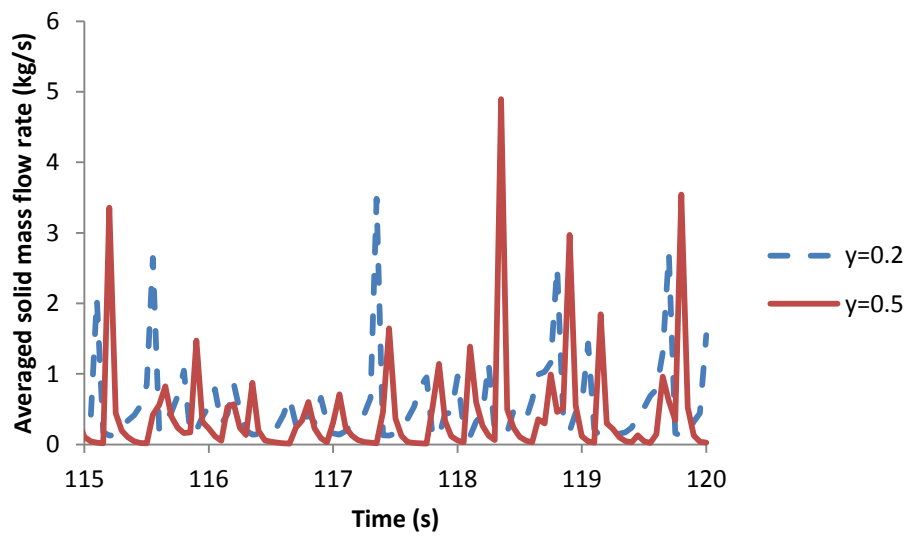


Figure 39 Averaged solid mass flow rate for $y=0.2\text{m}$ and $y=0.5\text{m}$ sections in 115-120 seconds

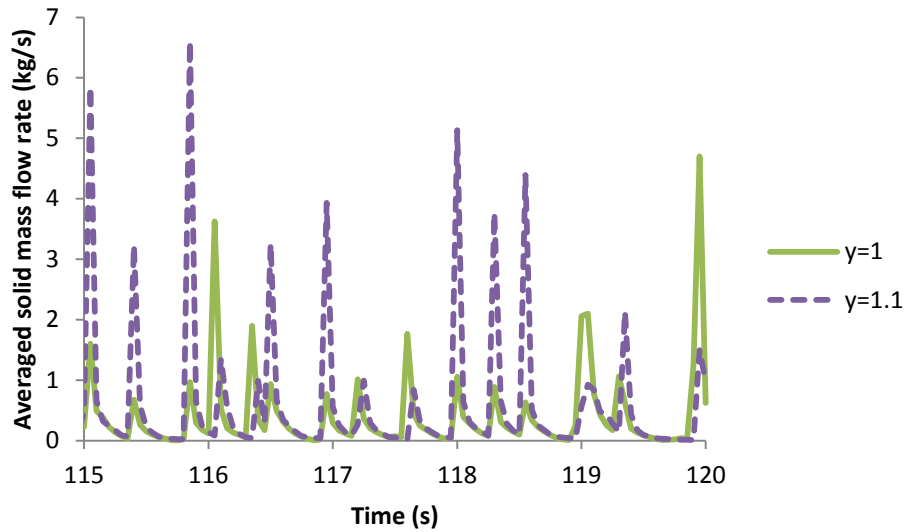


Figure 40 Averaged solid mass flow rate for $y=1\text{m}$ and $y=1.1\text{m}$ sections in 115-120 seconds

In Figure 39, fluctuations are not still very periodical. Especially for $y=0.2\text{m}$ case, which also refer to bubbling region, solid mass flow rate never drops to zero. For $y=0.5\text{m}$ case, which will also be defined as transition region, dense cluster movements are observable but the flow is not periodical. On the other hand, this periodic cluster flow is clearly distinguishable in riser regions which can be seen in Figure 40. It can be said that solid clusters are passing approximately in 0.4 seconds. Mass flow rates are greater at $y=1.1\text{m}$ section than $y=1\text{m}$ section, which will also be seen in following discussions about radial distribution of mass fluxes.

Radial distribution of mass fluxes at heights of $y=0.5\text{m}$ and $y=1\text{m}$ of the riser were presented in Figure 41. Please note that radial location of zero represents the central axis, which is also called symmetry axis in our axisymmetric simulation case. Time averaged data was taken for time range of 110-120 seconds.

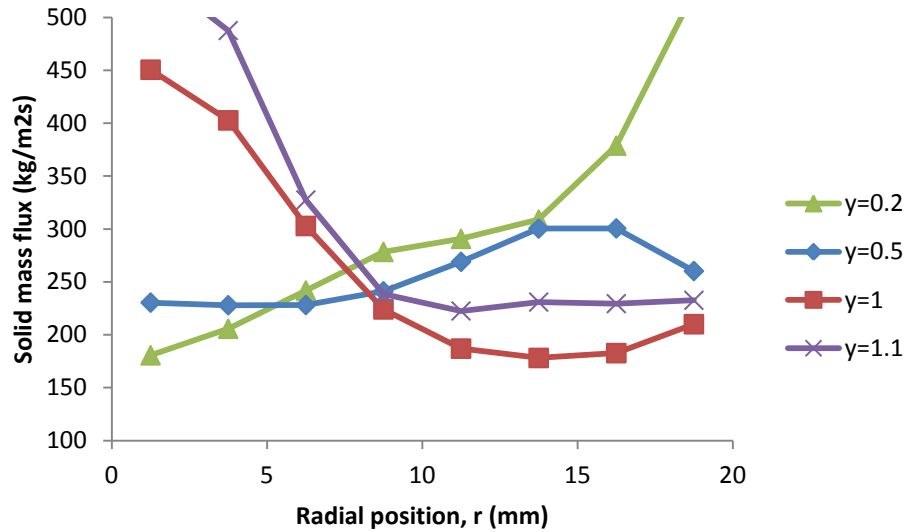


Figure 41 Radial distribution of mass fluxes at heights of $y=0.5\text{m}$ and $y=1\text{m}$ of the riser

Flow regime differences could clearly be distinguished in Figure 41. Solid phase was flowing near the riser wall for the bubbling bed region ($y=0.2\text{m}$). For $y=1\text{m}$ and $y=1.1\text{m}$ cases, the flow behavior was similar to core-annulus regimes of CFB risers. This similarity could be seen if the results were compared with the experimental data presented in Figure 31. Particles were mostly flowing in the core region of the riser. In $y=0.5\text{m}$ region, the flow showed transition behavior from bubbling bed to riser because the values were likely to be the arithmetic average of $y=0.2\text{m}$ and $y=1\text{m}$ cases.

In order to show time variation of radial mass flux distribution in heat transfer region ($y=0.5\text{m}$ and $y=1\text{m}$ cases), data taken in 50-60s time range and 110-120s time range for starting and ending point of that region are compared in Figure 42.

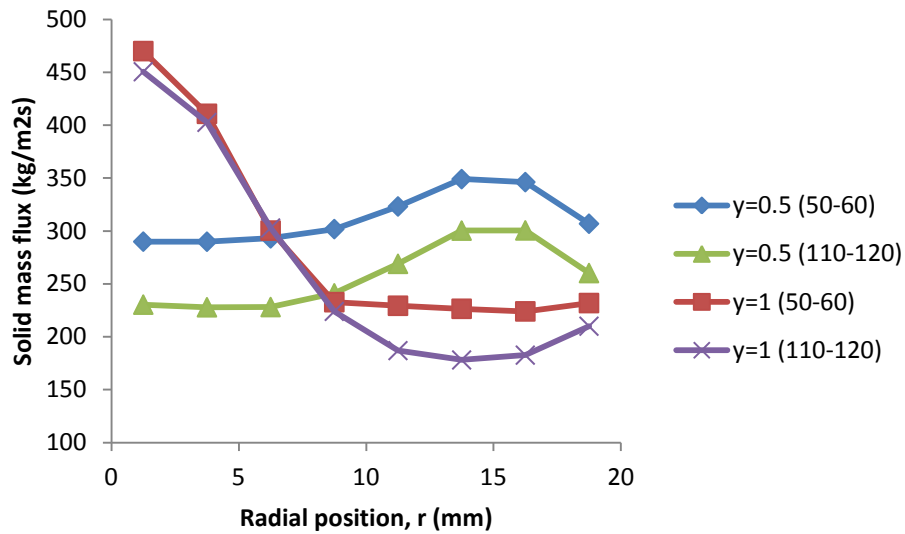


Figure 42 Radial distribution of mass fluxes in different time ranges for beginning and ending lines of heat transfer region

It can be clearly seen in Figure 42 that mass flux is decreased as time passes which can also be noticed in Figure 35. This may be caused by effect of initial charging which is discharging at earlier times of simulation. Mass flux profile does not change for $y=0.5m$, while mass flux decrease exists near wall region for $y=1m$.

5.2. Void Fraction

Void fraction is an important parameter in showing regimes of the flow. Radial distribution of void fractions were presented for similar riser cross sections used for average mass flow rate results which were $y=0.2m$, $0.5m$, $1m$ and $1.1m$.

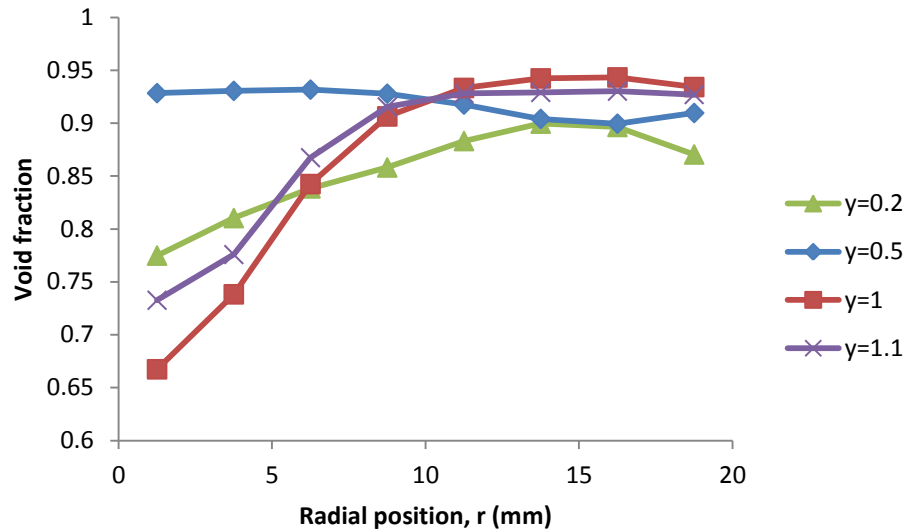


Figure 43 Radial distribution of void fraction at heights $y=0.2\text{m}$, 0.5m , 1m and 1.1m of the riser

As it can be seen in Figure 43 void fraction was very high near the wall. In other words, solid phase was accumulated at the core region especially near the exit of the riser. Due to frictional behavior of the wall, a little decrease in void fraction was noticeable for $y=0.2\text{m}$ and $y=1.1\text{m}$ cases. Usually solid accumulation exists near the wall which was not clearly seen in our results. This discrepancy might have been occurred due to special receiver design in which relatively big particles were loaded in thin pipe or gas penetration to the riser was near the wall region which caused an additional increase in the void fraction.

Similar to the comparison in Figure 42, time variation of radial void fraction distribution is shown in Figure 44. No big difference is observed for void fractions.

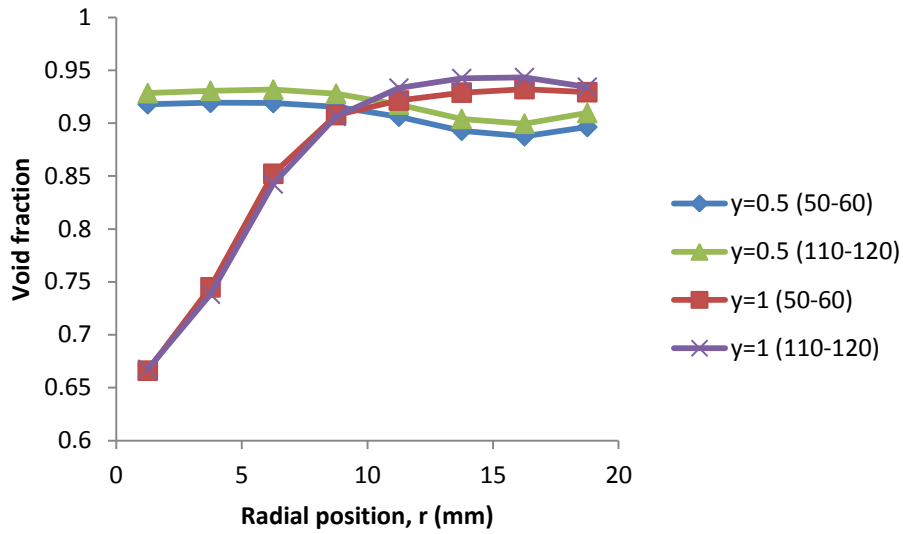


Figure 44 Radial distribution of void fractions in different time ranges for beginning and ending lines of heat transfer region

Void fraction contour plots of riser upwards of $y=0.4\text{m}$ are given in Figure 45. Instantaneous void fraction contour plots are taken for $t=30\text{s}$, 60s , 90s and 120s . Time averaged void fraction contour plot data of whole simulation is also shown in Figure 45. Instantaneous contour plots show us that mass is carried in the riser discretely. In other words, particle clusters are moving upwards in the riser and big voidage values exist except these. This particle carrying mechanism cannot be observed by time averaged results. For that reason, instantaneous void fraction contour plots for more focused bubbling, transition and riser sections in shorter time ranges are given in Appendix. In all times and upwards of $y=0.8\text{m}$ of the riser, particles are collected in core region.

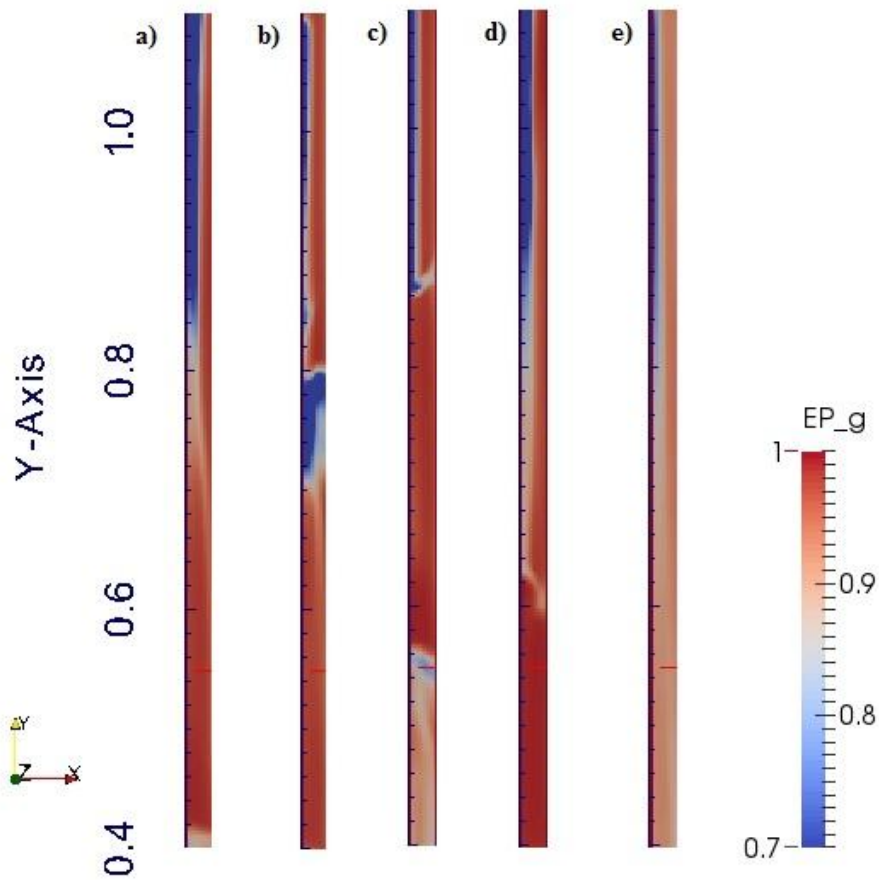


Figure 45 Instantaneous and time averaged void fraction contour plots for riser region upwards of 0.4m. a) $t=30s$; b) $t=60s$; c) $t=90s$; d) $t=120s$; e) Time averaged in the range of 0-120s

Axial distribution of void fraction is also an important parameter. Since solar radiation would irradiate the wall, it was important to have information about the near wall void fractions. At $r=18.8mm$ void fractions were plotted with the radially averaged data along the riser in Figure 46. Data shown in Figure 46 is time averaged in the range of 110-120s. Detailed void fraction contour plots can be seen in Appendix.

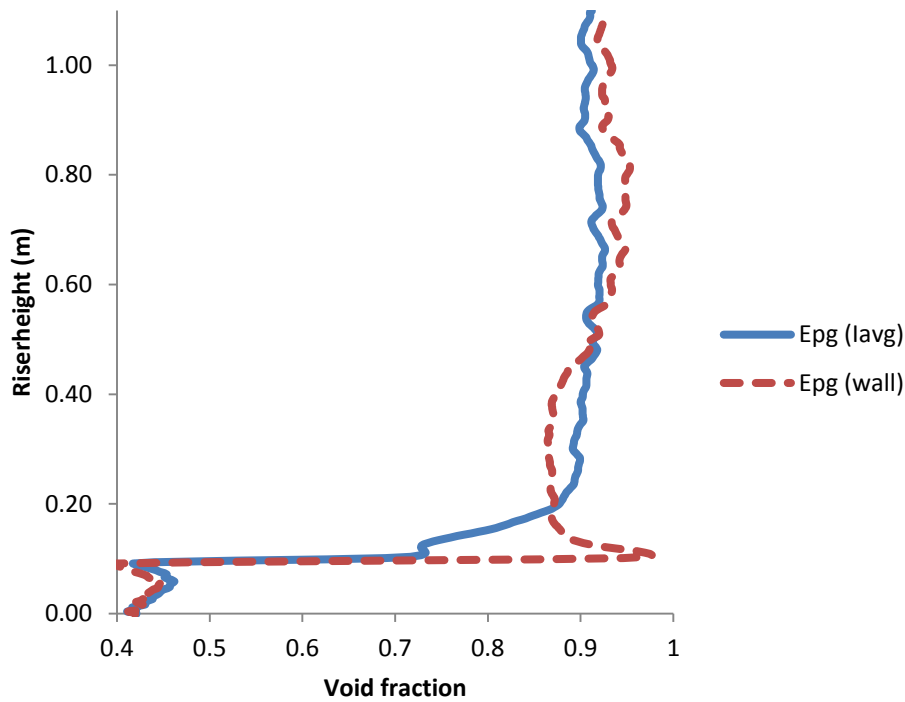


Figure 46 Radially averaged and near wall void fractions along the riser

In Figure 46, starting point of the riser pipe could be clearly seen where the height was 0.1m. At this starting point, there were almost no particles at the wall where the gas was penetrating. Up to 0.5m height, void fraction was less than the average which could be explained by the effect of bubbling bed at the lower part. However, beyond that region, where solar irradiation was supposed to expose, void fraction was greater than 0.9. This dilute behavior might give clues about heat transfer modes. It can be clearly stated that conduction would not be the dominant mode of heat transfer since the gas conductivity would be very low compared to the solid conductivity. Modeling radiative transfer from wall to particles becomes prominent for heat transfer investigations.

5.3. Solid and Gas Velocities

Radial distribution of solid vertical velocities for heights of $y=0.2\text{m}$, 0.5m , 1m and 1.1m were given in Figure 47. All the time averaged data shown in this section is also averaged in time range of 110-120s.

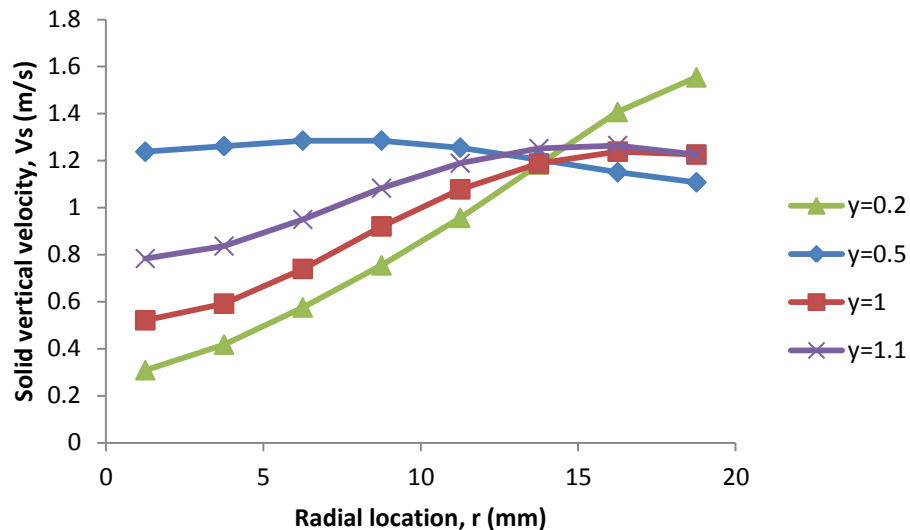


Figure 47 Radial distribution of solid vertical velocities at various heights of the riser

Solid velocity profiles were similar except $y=0.5\text{m}$ case in Figure 47 in which solid vertical velocity was smaller in wall region than the velocity in core region. Very low solid velocity was obtained in the middle of the bubbling bed region. For all cases except $y=0.2\text{m}$ case, a little slow down of solid velocity could be seen at the wall region. For the heat transfer region, solid velocity was around 1.2m/s at the wall. If Figure 47 was collated with Figure 43, it could be concluded that solid vertical velocity was smaller in dense regions and bigger in dilute regions where gas vertical velocity was expected to be bigger as well which would refer to a column of gas flow.

Similar to the solid vertical velocities, gas vertical velocities were presented in Figure 48

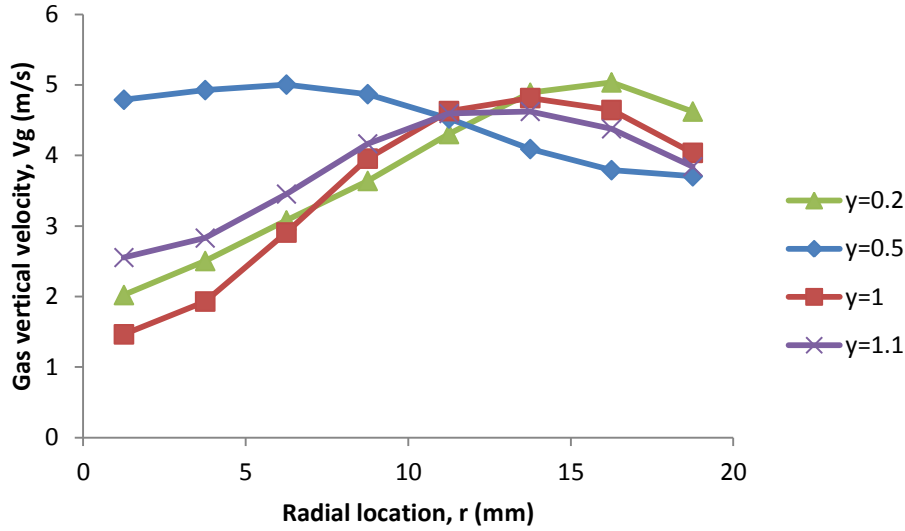


Figure 48 Radial distribution of gas vertical velocities at various heights of the riser

Gas vertical velocity profiles showed similarities with solid vertical velocity profiles except the fact that the gas velocity profiles were sharper. Wall gas velocity was around 4.5m/s at heat transfer region. If terminal velocity of particles were calculated using Equations (6),(7) and (8), $u_t = 3.48m/s$ was found. It can be seen that gas vertical velocity was greater than that value in most of the areas, but for low gas velocity regions this does not mean that particles will move downwards. For internal flows, critical Reynolds number for transition to turbulence regime is defined as 2300 [61]. Critical gas velocity in the riser can be calculated from following formula

$$V_{crit} = \frac{Re_{crit}\mu_g}{d_{riser}\rho_s} \quad (65)$$

Using $Re_{crit} = 2300$, critical gas velocity was calculated as $V_{crit} = 0.95m/s$. Since gas velocities in Figure 48 are greater than V_{crit} , turbulence flow was predicted for gas flow, which can be considered as an evidence for using $\kappa - \epsilon$ turbulence model for our case.

5.4. Pressure Drop

Gas pressure drop along the riser gives an idea about the mass amount in the riser and required operation power of the system. Pressure drop was defined as pressure difference between the corresponding region and inlet of the riser. Therefore, pressure drop at the exit showed the total pressure drop of the riser. Formula of the pressure drop is given with

$$\Delta P = P_{inlet} - P \quad (66)$$

Time averaged pressure drop in range of 110-120s is shown in Figure 49.

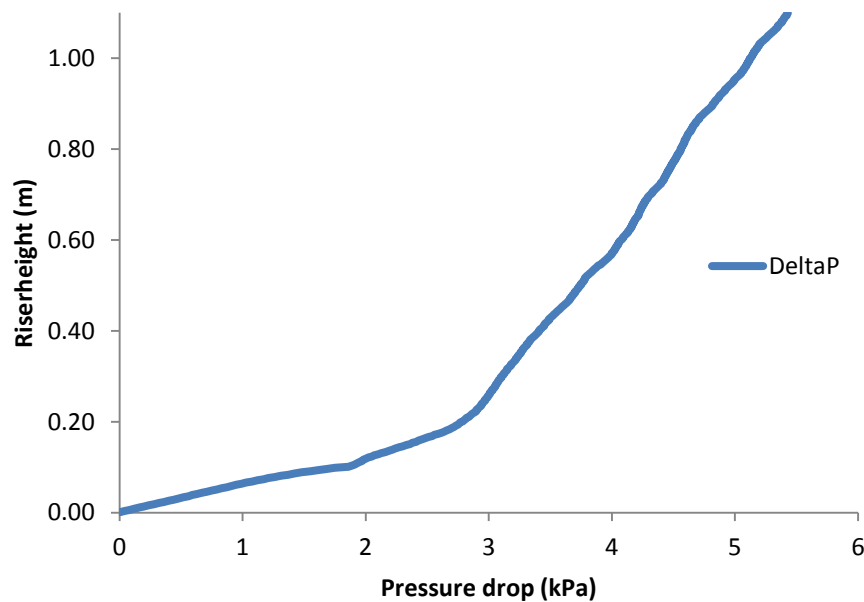


Figure 49 Pressure drop along the riser

Total pressure drop in the riser was found as $\Delta P = 5.43kPa$. There were three different pressure decrease areas in Figure 49 which were at heights of 0-0.1m, 0.1m-0.2m and 0.2m-1.1m. Pressure drop per unit length was maximum in bubbling bed region and decreased in upward regions. Pressure drop per unit length were calculated for three regions and tabulated in Table 7.

Table 7 Pressure drop per unit length for different regions of the receiver.

Height range (m)	Pressure drop per unit length (kPa/m)
0-0.1	18.6
0.1-0.2	9.5
0.2-1.1	2.82

These three different regions could be distinguished in axial distribution of void fractions in Figure 46. Please note that there was a relation between void fraction and pressure drop. The higher the void fraction, the lower the pressure drop. Actually relation between pressure drop and void fraction was given in drag coefficient formulas in Chapter 3.3. Drag coefficients were derived from pressure drop formulations, so that referring the void fraction-pressure drop relation to this equations is logical. Having dense flow regimes might increase the power requirement to compensate higher pressure drops.

CHAPTER 6

CONCLUSION

6.1. Summary

In this thesis, hydrodynamics of CFB is examined with Eulerian-Eulerian CFD method for concentrating solar thermal receiver applications. This study is aimed to establish a strong basis for further heat transfer investigations.

First chapter is related to thesis plan supported by literature review and motivation. A brief overview about CSP systems, HTF alternatives in receivers and thermal storage capabilities are discussed. Motivation of the thesis is supported by several advantages of using solid particles as HTF and storage medium. Previous studies about solid particle solar receivers are mentioned to give an idea about concept and state-of-art. Because Eulerian-Eulerian CFD method is used in the thesis, it is important to review studies covering CFD simulations of CFB risers loaded with sand like Geldart B type particles. Since model options vary due to particle classification, it is important to select proper studies and eliminate the studies in which common Geldart A particles are used such as FCC or silicon carbide particles.

In Chapter 2, some fundamental definitions are made about hydrodynamics of fluidization. Starting from different numerical methods for investigation of fluidized beds, theoretical bases of Two-Fluid CFD model are provided in Chapter 3. As mentioned in that chapter, Two-Fluid Method is based on the assumption of taking solid phase as fluid phase. Since granular flow behavior is adapted by constitutive relations, interphase forces and frictional/collisional mechanisms are complex. Chapter 3 covers only fundamental relations and very important constitutive

equations. Please note that one should go to references given for that theory for detailed information about the method and kinetic theory of granular flow.

Most important effort is put in model development which is discussed in Chapter 4. For examination of model options and parameters, a small bubbling fluidized bed model is built for which an experimental data is available. Experimental case is properly selected in which glass beads particles are used. Glass beads have almost the same properties with sand particles except sphericity. For all of the cases in this thesis, 2D axisymmetric model is constructed since it is expected to solve cylindrical geometries realistically in short simulation times. Grid independence study is performed and a proper grid size is selected for final model. Different drag models, wall boundary conditions and effect of turbulence are examined. Importance of modeling frictional/collisional behavior between particles and wall is highlighted and effect of modeling parameters in Johnson&Jackson's [62] model is examined. Turbulence is decided to be modeled with solid phase stress modifications of Ahmadi [57]. These examinations are previously published and presented in a conference [59]. Because our final model would be a CFB model, experimental validation study is performed by modeling the study of Mastellone [68]. The reason of selecting this study is the usage of sand particles and relatively small-scale riser which would reduce the computational cost. It is found in experimental validation study that wall boundary condition parameters which are specular coefficient and particle-wall restitution coefficients should be adjusted to fix radial distribution of mass fluxes and axial distribution of void fractions. Especially specular coefficient should be adjusted carefully, very low values should be selected to accurately model dilute CFB riser flows. After good match in mass flux and void fractions are obtained between experimental and numerical model, parameters used in numerical model is selected to be applied for final CFB riser solar receiver model.

Results are presented for CFB riser solar receiver in Chapter 5. Analysis are performed for 120 seconds only due to computational limitations. For four different heights, cross sectional data is taken to present radial distributions of flow

parameters. $y=0.2\text{m}$ is selected for exemplifying bubbling bed region; $y=0.5\text{m}$ and $y=1\text{m}$ are starting and ending points of heat transfer region where solar radiation would expose; and $y=1.1\text{m}$ case is the exit of the riser. Radial distribution of mass fluxes, void fractions and solid/gas velocities are presented. Axial distributions are plotted for a location near wall and compared with radially averaged results. Pressure drop is plotted across the height of riser/bed assembly which gives an idea about power requirement of the system.

6.2. Concluding Remarks

Hydrodynamics of fluidized beds are complex and should be modeled properly. Complexity comes from transient and fluctuating behavior of particulate flow. Usually industrial scale riser receiver designs are expected to be in meters which might correspond to transient flow solution in millions of cells. Such big risers may include billions of particles where particle tracking would be impossible. On the other hand, Eulerian methods like Two-Fluid Method require significant effort on modeling. Convergence may be an important issue since constitutive models are complex and non-linear. Small scale risers can be simulated in 2D models only with personal computers. Solution of millions of cells will certainly require parallelization in many cores around 100 which requires usage of a supercomputer or a cluster. Please keep in mind that parallelization may cause additional convergence issues to be handled.

2D axisymmetric model could show significantly good qualitative results and reasonably accurate quantitative results about hydrodynamics of the riser system. However, accurate results could be obtained by 3D models only. Modeling mesoscale structures are important for accuracy. Constructing 3D models for industrial scale risers can be possible by using coarse grids. In order to be able to catch mesoscale structures with coarse grids, subgrid models should be used. For example EMMS drag model can be used to predict flow heterogeneities with coarse grids. However, EMMS drag model requires case dependent pre-calculation effort to

determine location dependent drag coefficient reduction. Otherwise, conventional drag models like Syamlal or Gidaspow shows no big difference. Syamlal drag model requires experimental minimum fluidization velocity, so that it should be preferred only if experimental data is available.

Frictional and collisional mechanisms between particle and wall have great importance in modeling. Johnson&Jackson model gives the best result which considers no slip condition for gas phase and describes partial slip of solid phase with specularity coefficient and particle-wall restitution coefficient. These two parameters should be adjusted to fit with experimental results. For bubbling bed cases a moderate value of specularity coefficient around 0.5 is suggested, while very low specularity coefficient in order of magnitude of 10^{-4} is suggested for dilute CFB riser cases. Particle-wall restitution coefficient should be around 0.6 or 0.8. The lower the particle-wall restitution coefficient the more particle accumulation at the wall and the less kinetic energy of particles near the wall.

It is important to mention that particles in different classifications requires different models. Because Geldart A particles are smaller and more aeratable, usually gas and solid velocities are expected to be lower than Geldart B particles. However, sand like Geldart B particles have large minimum fluidization and terminal velocities, which requires high gas velocities in riser. High gas velocities refer high Re numbers, so that turbulence effects may not be neglected. For such high Re number cases, such as the case in this thesis, solid phase stress modifications based on turbulence models might be useful for better estimation of void fractions at the wall. Moreover, smaller particles require smaller grids, so that subgrid models would be required for big scale riser receiver models. It is hard to obtain grid independence. As a rule of thumb, ten times particle diameter is suggested, but even 4 times finer mesh than 10 particle diameter is necessary for the model built in this thesis.

Steady state operating condition is hard to achieve. While solid particles are injected with solid mass flow rate of 0.5kg/s, mass flow rate at the outlet is obtained around 0.4kg/s which means that steady state operation could not be reached in simulation

time or all of the particles could not be carried through the riser which cause particle agglomeration in the bed. In terms of radial distribution of mass fluxes, bubbling bed and riser regions show opposite profiles. Mass flux is greater in core region of riser while it is smaller in core region of bubbling bed.

Void fraction is increased near wall in riser region. Very little decrease is obtained at wall due to friction and particle agglomeration. It is expected to be greater. However, the only outlet is end of the riser, so that all of the gas is penetrating into riser pipe near wall due to special riser/bed assembly. This might have caused an extra increase in void fraction near wall region. Normally there is another pressure regulation valve in bed region from which some amount of gas is extracted. Due to different flow characteristics in bubbling bed and riser regions, a transition region is observed. Transition region is obtained in 0.5m height case. Velocity profiles of transition region are distinguishable compared to other regions. Average and near wall void fractions are greater than 0.9 in heat transfer region which gave a clue about possible models about heat transfer. It can be concluded that conduction would not be dominant heat transfer mode since gas thermal conductivity is low. If heat transfer would be solved with conduction, it is more logical to calculate conductivities from kinetic theory, rather than packed-bed conductivity models. Since the flow is dilute near wall, wall-to-particle radiative transfer would be dominant. Gas phase would be heated by convection and particles would gain heat from gas phase via convection again.

For pressure drop, three different regions are noticed. Pressure drop per unit length is very large upon riser pipe inlet and this pressure drop rate decreases for upper riser regions. Direct relation between pressure drop and void fraction is obtained. The higher the void fraction, the less the pressure drop. Total pressure drop along the riser is determined as 5.43kPa.

6.3. Future Work

There are further research opportunities available following this thesis.

First of all, since the aim of the thesis was providing a strong basis for heat transfer investigations, a heat transfer model can be constructed starting with this hydrodynamics model. Please note that including conduction and convection, interphase heat transfer and radiative transfer between wall and participating media will be under consideration.

Secondly, limitations of this hydrodynamics study can be solved. It is expected that 3D model would give more accurate results. Subgrid models can be used, so that solution with coarser mesh will be possible. Case dependent drag models can be constructed and applied to the model. Gas leakage from pressure regulation valve in original model of Flamant [6] can be modeled.

Using the same model, different operating conditions can be examined. This will allow obtaining different flow behaviors. Solid mass flow rate or superficial gas velocity can be varied or secondary gas inlet can be added to the system to control the flow. Riser geometry can be changed which give opportunity to create novel designs. Changing the operating conditions or particle size, slowly moving dense suspension regimes can be obtained which may be preferable for heat transfer and thermal storage purposes.

Different particles can be tried such as silicon carbide or PCM capsules. Please note that different particle types may require a completely different grid size and model parameters. Since PCM capsules are generally bigger than 1mm diameter, it may be possible to use Lagrangian methods. Silicon Carbide particles are finer than sand, so that especially drag coefficient should be modeled properly.

Using the information obtained from the receiver results, other components of the CSP system can be modeled like the cyclone, the heat exchanger or the storage tank.

If heat transfer investigations are also completed, advantages and disadvantages of the concept for CSP systems and storage capabilities can be examined.

REFERENCES

- [1] S. Kuravi, J. Trahan, D. Y. Goswami, M. M. Rahman, and E. K. Stefanakos, “Thermal energy storage technologies and systems for concentrating solar power plants,” *Prog. Energy Combust. Sci.*, vol. 39, no. 4, pp. 285–319, 2013.
- [2] H. Price, E. Lüpfert, D. Kearney, E. Zarza, G. Cohen, R. Gee, and R. Mahoney, “Advances in Parabolic Trough Solar Power Technology,” *J. Sol. Energy Eng.*, vol. 124, no. 2, p. 109, 2002.
- [3] C. Uçkun and D. K. Baker, *Modeling and simulations of direct steam generation in concentrating solar power plants using parabolic trough collectors. [Electronic resource]*. Ankara : METU ; 2013.
- [4] Estela, “Strategic Research Agenda 2020-2025,” no. december, 2012.
- [5] C. K. Ho and B. D. Iverson, “Review of high-temperature central receiver designs for concentrating solar power,” *Renew. Sustain. Energy Rev.*, vol. 29, pp. 835–846, Jan. 2014.
- [6] G. Flamant, D. Gauthier, H. Benoit, J.-L. Sans, R. Garcia, B. Boissière, R. Ansart, and M. Hemati, “Dense suspension of solid particles as a new heat transfer fluid for concentrated solar thermal plants: On-sun proof of concept,” *Chem. Eng. Sci.*, vol. 102, pp. 567–576, Oct. 2013.
- [7] J. A. Duffie and W. A. Beckman, *Solar engineering of thermal processes*, vol. 3. Wiley New York etc., 1980.
- [8] S. A. Kalogirou, *Solar energy engineering: processes and systems*. Academic Press, 2013.
- [9] H. L. Zhang, J. Baeyens, J. Degève, and G. Cacères, “Concentrated solar power plants: Review and design methodology,” *Renew. Sustain. Energy Rev.*, vol. 22, pp. 466–481, 2013.
- [10] J. Mcfarlane, “Heat Transfer Fluids for Concentrating Solar Power,” *Solar Energy and Energy Storage Workshop*. 2010.
- [11] T. Tan and Y. Chen, “Review of study on solid particle solar receivers,” *Renew. Sustain. Energy Rev.*, vol. 14, no. 1, pp. 265–276, Jan. 2010.

- [12] U. Herrmann and D. W. Kearney, "Survey of thermal energy storage for parabolic trough power plants," *J. Sol. Energy Eng.*, vol. 124, no. 2, pp. 145–152, 2002.
- [13] Y. Tian and C. Y. Zhao, "A review of solar collectors and thermal energy storage in solar thermal applications," *Appl. Energy*, vol. 104, pp. 538–553, 2013.
- [14] J. Hruby, R. Steeper, G. Evans, and C. Crowe, "An experimental and numerical study of flow and convective heat transfer in a freely falling curtain of particles," *J. Fluids Eng.*, vol. 110, no. 2, pp. 172–181, 1988.
- [15] M. J. Rightley, L. K. Matthews, and G. P. Mulholland, "Experimental characterization of the heat transfer in a free-falling-particle receiver," *Solar Energy*, vol. 48, no. 6, pp. 363–374, 1992.
- [16] H. Chen, Y. Chen, H.-T. Hsieh, and N. Siegel, "Computational Fluid Dynamics Modeling of Gas-Particle Flow Within a Solid-Particle Solar Receiver," *J. Sol. Energy Eng.*, vol. 129, no. 2, p. 160, 2007.
- [17] K. Kim, S. F. Moujaes, and G. J. Kolb, "Experimental and simulation study on wind affecting particle flow in a solar receiver," *Sol. Energy*, vol. 84, no. 2, pp. 263–270, 2010.
- [18] N. P. Siegel, C. K. Ho, S. S. Khalsa, and G. J. Kolb, "Development and Evaluation of a Prototype Solid Particle Receiver: On-Sun Testing and Model Validation," *J. Sol. Energy Eng.*, vol. 132, no. 2, p. 021008, 2010.
- [19] SunShot U.S. Department of Energy, "High Temperature Falling-Particle Receiver."
- [20] G. Flamant, "Theoretical and experimental study of radiant heat transfer in a solar fluidized-bed receiver," *AIChE J.*, vol. 28, no. 4, pp. 529–535, Jul. 1982.
- [21] Z. Ma, G. C. Glatzmaier, and M. Mehos, "Development of solid particle thermal energy storage for concentrating solar power plants that use fluidized bed technology," vol. 49, pp. 898–907, 2014.
- [22] Z. Ma, M. Mehos, G. Glatzmaier, and B. B. Sakadjian, "Development of a concentrating solar power system using fluidized- bed technology for thermal energy conversion and solid particles for thermal energy storage," vol. 69, pp. 1349–1359, 2015.
- [23] F. Pitié, C. Y. Zhao, J. Baeyens, J. Degève, and H. L. Zhang, "Circulating fluidized bed heat recovery/storage and its potential to use coated phase-

- change-material (PCM) particles,” *Appl. Energy*, vol. 109, pp. 505–513, Sep. 2013.
- [24] a. Brems, G. Cáceres, R. Dewil, J. Baeyens, and F. Pitié, “Heat transfer to the riser-wall of a circulating fluidised bed (CFB),” *Energy*, vol. 50, pp. 493–500, Feb. 2013.
- [25] “Concentrated Solar Power in Particles European Project.” [Online]. Available: <http://www.csp2-project.eu/>. [Accessed: 01-Jan-2015].
- [26] D. Geldart, “Types of gas fluidization,” *Powder Technol.*, vol. 7, no. 5, pp. 285–292, 1973.
- [27] H. Enwald, E. Peirano, and a E. Almstedt, “Eulerian two-phase flow theory applied to fluidization,” *Int. J. Multiph. Flow*, vol. 22, no. 1975, pp. 21–66, 1996.
- [28] Y. P. Tsuo and D. Gidaspow, “Computation of flow patterns in circulating fluidized beds,” *AIChE J.*, vol. 36, no. 6, pp. 885–896, 1990.
- [29] V. Mathiesen, T. Solberg, and B. H. Hjertager, “An experimental and computational study of multiphase flow behavior in a circulating fluidized bed,” *Int. J. Multiph. Flow*, vol. 26, no. 3, pp. 387–419, 2000.
- [30] D. . Zhang and W. . VanderHeyden, “High-resolution three-dimensional numerical simulation of a circulating fluidized bed,” *Powder Technol.*, vol. 116, no. 2–3, pp. 133–141, May 2001.
- [31] D. Z. Zhang and W. B. VanderHeyden, “The effects of mesoscale structures on the macroscopic momentum equations for two-phase flows,” *Int. J. Multiph. Flow*, vol. 28, no. 5, pp. 805–822, 2002.
- [32] E.-U. Hartge, L. Ratschow, R. Wischnewski, and J. Werther, “CFD-simulation of a circulating fluidized bed riser,” *Particuology*, vol. 7, no. 4, pp. 283–296, Aug. 2009.
- [33] N. Zhang, B. Lu, W. Wang, and J. Li, “3D CFD simulation of hydrodynamics of a 150MW e circulating fluidized bed boiler,” *Chem. Eng. J.*, vol. 162, no. 2, pp. 821–828, 2010.
- [34] T. D. B. Nguyen, M. W. Seo, Y.-I. Lim, B.-H. Song, and S.-D. Kim, “CFD simulation with experiments in a dual circulating fluidized bed gasifier,” *Comput. Chem. Eng.*, vol. 36, pp. 48–56, Jan. 2012.

- [35] Ö. Baysal, “Akışkan Yatak İçerisindeki Gaz-Katı İki Fazlı Akışın Hidrodinamiğinin Sayısal Olarak İncelenmesi,” Gazi University, 2007.
- [36] Ö. Baysal, K. M. Fevzi, H. Topal, and Ş. Başkaya, “Sirkülasyonlu Akışkan Yatakta Gaz-Katı Akış Hidrodinamiğinin Sayısal Olarak İncelenmesi,” *Isı Bilim. ve Tek. Derg.*, vol. 27, no. 2, pp. 21–32, 2007.
- [37] T. Li, A. Gel, S. Pannala, M. Shahnam, and M. Syamlal, “Reprint of ‘CFD simulations of circulating fluidized bed risers, part I: Grid study,’” *Powder Technol.*, vol. 265, pp. 2–12, 2014.
- [38] T. Li, S. Pannala, and M. Shahnam, “CFD simulations of circulating fluidized bed risers, part II, evaluation of differences between 2D and 3D simulations,” *Powder Technol.*, vol. 254, pp. 115–124, 2014.
- [39] W.-C. Yang, *Handbook of Fluidization and Fluid-Particle Systems*. Pittsburgh, Pennsylvania, 2003.
- [40] D. Knutti and O. Levenspiel, *Fluidization Engineering*, Second Edi. Butterworth-Heinemann, 1991.
- [41] Neutrium, “Terminal Velocity of Particles for Gravity Separation.” [Online]. Available: <https://neutrium.net/unit-operations/terminal-velocity-of-particles-for-gravity-separation/>. [Accessed: 10-Sep-2015].
- [42] S. Choi, Y. S. Kim, D. S. Park, S. J. Kim, J. M. Kim, H. C. Kim, S. H. Oh, T.-J. Kim, and D. H. Choo, “Catalytic cracking process using fast fluidization for the production of light olefins from hydrocarbon feedstock.” Google Patents, 2012.
- [43] B. G. M. Van Wachem, J. C. Schouten, C. M. Van den Bleek, R. Krishna, and J. L. Sinclair, “Comparative analysis of CFD models of dense gas-solid systems,” *AIChE J.*, vol. 47, no. 5, pp. 1035–1051, 2001.
- [44] S. Pannala, M. Syamlal, and T. J. O’Brien, *Computational Gas-Solids Flows and Reacting Systems: Theory, Methods and Practice*. Hershey, New York: IGI Global, 2010.
- [45] V. V. Ranade, *Computational flow modeling for chemical reactor engineering*, vol. 5. Academic press, 2001.
- [46] M. Syamlal, W. Rogers, and T. J. O’Brien, “MFIX Documentation: Volume 1, Theory Guide,” vol. 1004, no. December, 1993.

- [47] S. Benyahia, M. Syamlal, and T. J. O'Brien, "Summary of MFIX Equations 2012-1," *From URL <https://mfix.netl.doe.gov/> ...*, vol. 1, no. January, 2012.
- [48] C. Wen and Y. H. Yu, "Mechanics of fluidization," in *Chem. Eng. Prog. Symp. Ser.*, 2014, vol. 62, no. 62, p. 100.
- [49] D. Gidaspow, *Multiphase flow and fluidization: continuum and kinetic theory descriptions*. Academic press, 1994.
- [50] S. Ergun, "Fluid flow through packed columns," *Chem. Eng. Prog.*, vol. 48, 1952.
- [51] P. N. Rowe and G. A. Henwood, *Drag forces in a hydraulic model of a fluidised bed*. UKAEA, 1960.
- [52] J. M. DallaValle, "Micromeritics.," *Soil Sci.*, vol. 56, no. 2, p. 151, 1943.
- [53] J. Garside and M. R. Al-Dibouni, "Velocity-voidage relationships for fluidization and sedimentation in solid-liquid systems," *Ind. Eng. Chem. Process Des. Dev.*, vol. 16, no. 2, pp. 206–214, 1977.
- [54] D. G. Schaeffer, "Instability in the evolution equations describing incompressible granular flow," *J. Differ. Equ.*, vol. 66, no. 1, pp. 19–50, 1987.
- [55] S. Benyahia, M. Syamlal, and T. J. O'Brien, "Evaluation of boundary conditions used to model dilute, turbulent gas/solids flows in a pipe," *Powder Technol.*, vol. 156, no. 2–3, pp. 62–72, 2005.
- [56] S. Benyahia, "Gas/Solids Turbulence models implemented in MFIX," 2005.
- [57] J. Cao and G. Ahmadi, "Gas-particle two-phase turbulent flow in a vertical duct," *Int. J. Multiph. Flow*, vol. 21, no. 6, pp. 1203–1228, 1995.
- [58] NETL, "Multiphase Flow with Interphase eXchanges (MFIX)." [Online]. Available: <https://mfix.netl.doe.gov/>. [Accessed: 01-Jan-2015].
- [59] S. Bilyaz and İ. Tari, "Investigation of Various Options for Numerical Modeling of Fluidized Beds for a Solar Thermal Application," in *ICHMT International Symposium on Advances in Computational Heat Transfer*, 2015.
- [60] M. Deza, N. P. Franka, T. J. Heindel, and F. Battaglia, "CFD Modeling and X-Ray Imaging of Biomass in a Fluidized Bed," *J. Fluids Eng.*, vol. 131, no. 11, p. 111303, 2009.

- [61] T. L. Bergman, F. P. Incropera, and A. S. Lavine, *Fundamentals of heat and mass transfer*. John Wiley & Sons, 2011.
- [62] P. C. Johnson and R. Jackson, “Frictional--collisional constitutive relations for granular materials, with application to plane shearing,” *J. Fluid Mech.*, vol. 176, pp. 67–93, 1987.
- [63] T. Li and S. Benyahia, “Revisiting Johnson and Jackson boundary conditions for granular flows,” *AIChE J.*, vol. 58, no. 7, pp. 2058–2068, 2012.
- [64] T. Li and S. Benyahia, “Evaluation of wall boundary condition parameters for gas--solids fluidized bed simulations,” *AIChE J.*, vol. 59, no. 10, pp. 3624–3632, 2013.
- [65] L. Kong, C. Zhang, and J. Zhu, “Evaluation of the effect of wall boundary conditions on numerical simulations of circulating fluidized beds,” *Particuology*, vol. 13, pp. 114–123, 2014.
- [66] X. Zhou, J. Gao, C. Xu, and X. Lan, “Effect of wall boundary condition on CFD simulation of CFB risers,” *Particuology*, vol. 11, no. 5, pp. 556–565, 2013.
- [67] J. T. Jenkins and M. Y. Louge, “On the flux of fluctuation energy in a collisional grain flow at a flat, frictional wall,” *Phys. Fluids*, vol. 9, no. 10, pp. 2835–2840, 1997.
- [68] M. L. Mastellone and U. Arena, “The effect of particle size and density on solids distribution along the riser of a circulating fluidized bed,” *Chem. Eng. Sci.*, vol. 54, no. 22, pp. 5383–5391, 1999.
- [69] T. Li, R. Garg, J. Galvin, and S. Pannala, “Open-source MFIX-DEM software for gas-solids flows: Part II — Validation studies,” *Powder Technol.*, vol. 220, pp. 138–150, Apr. 2012.
- [70] B. Boissiere, H. Benoit, R. Ansart, H. Neau, D. Gauthier, G. Flamant, and M. Hemati, “Hydrodynamics of Dense Fluidized Beds for Application in Concentrated Solar Energy Conversion,” 2013.

**APPENDIX: INSTANTANEOUS VOID FRACTION CONTOUR PLOTS
OF DIFERENT REGIONS FOR 118-119 SECONDS TIME RANGE**

